



HAL
open science

Emulating IPCC AR4 atmosphere-ocean and carbon cycle models for projecting global-mean, hemispheric and land/ocean temperatures: MAGICC 6.0

M. Meinshausen, S. C. B. Raper, T. M. L. Wigley

► **To cite this version:**

M. Meinshausen, S. C. B. Raper, T. M. L. Wigley. Emulating IPCC AR4 atmosphere-ocean and carbon cycle models for projecting global-mean, hemispheric and land/ocean temperatures: MAGICC 6.0. Atmospheric Chemistry and Physics Discussions, 2008, 8 (2), pp.6153-6272. hal-00304059

HAL Id: hal-00304059

<https://hal.science/hal-00304059>

Submitted on 18 Jun 2008

HAL is a multi-disciplinary open access archive for the deposit and dissemination of scientific research documents, whether they are published or not. The documents may come from teaching and research institutions in France or abroad, or from public or private research centers.

L'archive ouverte pluridisciplinaire **HAL**, est destinée au dépôt et à la diffusion de documents scientifiques de niveau recherche, publiés ou non, émanant des établissements d'enseignement et de recherche français ou étrangers, des laboratoires publics ou privés.

MAGICC 6.0

M. Meinshausen et al.

Emulating IPCC AR4 atmosphere-ocean and carbon cycle models for projecting global-mean, hemispheric and land/ocean temperatures: MAGICC 6.0

M. Meinshausen¹, S. C. B. Raper², and T. M. L. Wigley³

¹Potsdam Institute for Climate Impact Research (PIK), Potsdam, Germany

²Manchester Metropolitan University (MMU), Manchester, UK

³National Center for Atmospheric Research (NCAR), Boulder, CO, USA

Received: 20 December 2007 – Accepted: 6 January 2008 – Published: 27 March 2008

Correspondence to: M. Meinshausen (malte.meinshausen@pik-potsdam.de)

Published by Copernicus Publications on behalf of the European Geosciences Union.

Title Page

Abstract

Introduction

Conclusions

References

Tables

Figures

◀

▶

◀

▶

Back

Close

Full Screen / Esc

Printer-friendly Version

Interactive Discussion



Abstract

Current scientific knowledge on the future response of the climate system to human-induced perturbations is comprehensively captured by various model intercomparison efforts. In the preparation of the Fourth Assessment Report (AR4) of the Intergovernmental Panel on Climate Change (IPCC), intercomparisons were organized for atmosphere-ocean general circulation models (AOGCMs) and carbon cycle models, named “CMIP3” and “C4MIP”, respectively. Despite their tremendous value for the scientific community and policy makers alike, there are some difficulties in interpreting the results. For example, key radiative forcings have not been considered or standardized in the majority of AOGCMs integrations and carbon cycle runs. Furthermore, the AOGCM analysis of plausible emission pathways was restricted to only three SRES scenarios. This study attempts to address these issues. We present an updated version of MAGICC, the simple carbon cycle-climate model used in past IPCC Assessment Reports with enhanced representation of time-varying climate sensitivities, carbon cycle feedbacks, aerosol forcings and ocean heat uptake characteristics. This new version of MAGICC (6.0) is successfully calibrated against the higher complexity AOGCM and carbon cycle models. Parameterizations of MAGICC 6.0 are provided. Previous MAGICC versions and emulations shown in IPCC AR4 (WG1, Fig. 10.26, page 803) yielded, in average, a 10% larger global-mean temperature increase over the 21st century compared to the AOGCMs. The reasons for this difference are discussed. The emulations presented here using MAGICC 6.0 match the mean AOGCM responses to within 2.2% for the SRES scenarios. This enhanced emulation skill is due to: the comparison on a “like-with-like” basis using AOGCM-specific subsets of forcings, a new calibration procedure, as well as the fact that the updated simple climate model can now successfully emulate some of the climate-state dependent effective climate sensitivities of AOGCMs. The mean diagnosed effective climate sensitivities of the AOGCMs is 2.88°C, about 0.33°C cooler than the reported slab ocean climate sensitivities. Finally, we examine the combined climate system and carbon cycle em-

ACPD

8, 6153–6272, 2008

MAGICC 6.0

M. Meinshausen et al.

Title Page

Abstract

Introduction

Conclusions

References

Tables

Figures

◀

▶

◀

▶

Back

Close

Full Screen / Esc

Printer-friendly Version

Interactive Discussion



ulations for the complete range of IPCC SRES emission scenarios and some lower mitigation pathways.

1 Introduction: the value of simple climate models

Since the introduction of three-dimensional coupled atmosphere-ocean general circulation models (AOGCMs) (e.g. [Manabe and Bryan, 1969](#); [Manabe et al., 1975](#); [Bryan et al., 1975](#)), one goal of Earth system science for understanding the past and projecting the future is to build highly resolved, comprehensive and coupled models of the physical atmosphere and ocean dynamics, including models of the Earth's cryosphere, terrestrial and marine biota. Depending on the research question, though, intermediate complexity or simpler models will remain more suitable research tools, due to their focus on individual processes, their ability to encompass part of the structural uncertainties of complex models, and/or their computational efficiency. After the introduction of the one-dimensional upwelling-diffusive ocean model by [Hoffert et al. \(1980\)](#), early applications of simple models were able to give insights into climate system behaviour as their relative simplicity allowed isolation and investigation of individual feedback processes, multi-thousand year simulations, and various parameterizations ([Harvey and Schneider, 1985b,a](#); [Hoffert et al., 1980](#); [Schneider and Thompson, 1981](#)). Recently, this role has also been filled by intermediate complexity models. Shifting from their role as models in their own right, simple models started to serve four distinct purposes as exemplified in this study:

I) Emulations. Simple models are used to emulate global or large-scale averaged quantities of AOGCMs (see e.g. [Schlesinger and Jiang, 1990, 1991](#)). In most cases, AOGCMs are still computationally too expensive for large ensembles for different emission scenarios and/or perturbed physics experiments except in special circumstances ([Allen, 1999](#); [Stainforth et al., 2005](#)). A precondition for the quantitative reliability of AOGCM emulations is that the emulation of the variables of interest is suitably accurate over a wide range of scenarios actually performed with AOGCMs. Various authors

Title Page

Abstract

Introduction

Conclusions

References

Tables

Figures

◀

▶

◀

▶

Back

Close

Full Screen / Esc

Printer-friendly Version

Interactive Discussion



(e.g. Raper and Cubasch, 1996; Kattenberg et al., 1996; Raper et al., 2001; Cubasch et al., 2001; Osborn et al., 2006) have shown for example that the upwelling-diffusion model MAGICC, the primary simple climate model used in past IPCC Assessment Reports, can closely match key large-scale AOGCMs results.

In the preparation of the Intergovernmental Panel on Climate Change Fourth Assessment Report (IPCC AR4), fourteen modeling groups submitted data for 23 AOGCMs, building the World Climate Research Programme's (WCRP's) Coupled Model Inter-comparison Project phase 3 (CMIP3) multi-model dataset. Each of these AOGCMs is structurally different (although the degree to which they differ is variable), leading to variations in their climate response characteristics. In the present study we show emulations of oceanic heat uptake and surface air temperatures over land and ocean in both hemispheres for 19 of these AOGCMs (i.e., those for which suitable data were available). In addition to the no-climate-policy SRES scenarios analyzed in IPCC AR4, we also present joint AOGCM and carbon cycle model projections for a set of multi-gas mitigation scenarios and pathways.

II) Spanning structural uncertainties. The advantage of simple models is that structural uncertainties across a large set of complex models can be captured. Structural uncertainties are reflected by the different choices made by modeling groups, e.g. what key processes should be included and how they should be modeled. Parametric uncertainty, in contrast, is the uncertainty arising from choices in the parameter values for a model with given structure. In practice, a strict separation between these two types of uncertainties is not possible. In fact, we take advantage of this overlap in the present study by "parameterizing" the structural uncertainty range of more complex models (cf. O'Neill and Melnikov, 2008). This approach is distinct from perturbed physics studies with intermediate complexity models or AOGCMs, which often concentrate on assessing parametric uncertainties. Sufficiently flexible simple models, once calibrated to sophisticated models help to indicate structural uncertainties, for a limited set of key quantities, like hemispheric mean temperatures and only to the extent that variations in the AOGCM responses are due to structurally different model com-

[Title Page](#)[Abstract](#)[Introduction](#)[Conclusions](#)[References](#)[Tables](#)[Figures](#)[◀](#)[▶](#)[◀](#)[▶](#)[Back](#)[Close](#)[Full Screen / Esc](#)[Printer-friendly Version](#)[Interactive Discussion](#)

ponents. As shown in this study, calibrating a simple model to the CMIP3 AOGCMs provides some measure of structural uncertainty, e.g. in regard to the models' feedback processes summarized by the calibrated climate sensitivity parameter. This structural uncertainty can then be translated to scenarios, which were not run by all AOGCMs.

5 **III) Factor separation analysis.** Simple models can assist in factor separation analysis, i.e., separating climate or carbon cycle responses from forcing uncertainties or investigating the effects due to different initialization choices. Thus, simple models can assist in harmonizing AOGCM and other higher complexity model responses, e.g. by estimating their responses for unified forcing assumptions. A major difficulty in interpreting the multi-model AOGCM projections presented in IPCC AR4 arises from the different sets of radiative forcings agents considered by the various modeling groups (see Table 10.1 in [Meehl et al., 2007](#)). Even for the common forcings, the magnitude and time-evolution differs from model to model for the same scenario. For example, some models applied only very weak volcanic forcing in the 20th century runs, while some ignored volcanic forcing completely; some models varied tropospheric ozone, while others kept the forcing by tropospheric ozone constant for the 21st century.

Further complications arise due to the fact that for most AOGCMs, the forcing time-series are not diagnosed or documented from the model runs – with some exceptions like [Takemura et al. \(2006\)](#) and [Hansen et al. \(2005\)](#). Different reporting standards for radiative forcing, like reporting adjusted forcing after thermal stratospheric adjustment at the model's tropopause or at 200 hPa level, further hinder comparability, even if some diagnostic data are provided as for the doubled CO₂ concentration experiments (see e.g. Table 2 in [Forster and Taylor, 2006](#)). In addition, studies comparing the radiative transfer schemes in AOGCMs found surprisingly large differences from the line-by-line code, even for well known forcing agents like CO₂ ([Collins et al., 2006](#)). In summary, imperfect knowledge with regard to the forcings in CMIP3 AOGCMs leads to ambiguities as to whether differences in their climate responses are due to different climate responses or partly an expression of different (sometimes limited or erroneous) radiative forcing implementations.

Title Page

Abstract

Introduction

Conclusions

References

Tables

Figures

◀

▶

◀

▶

Back

Close

Full Screen / Esc

Printer-friendly Version

Interactive Discussion



MAGICC 6.0

M. Meinshausen et al.

[Title Page](#)[Abstract](#)[Introduction](#)[Conclusions](#)[References](#)[Tables](#)[Figures](#)[I◀](#)[▶I](#)[◀](#)[▶](#)[Back](#)[Close](#)[Full Screen / Esc](#)[Printer-friendly Version](#)[Interactive Discussion](#)

Faced with these challenges, this study attempts to separate radiative forcing and climate response uncertainties in AOGCMs. Thus, using “like-with-like” forcing time series to match the AOGCM specific sets of considered forcing agents, the parameterizations in the simple climate model are calibrated to match the AOGCMs’ climate responses. Subsequent emulations take into account the complete set of key forcing agents – thereby providing an estimate of the AOGCMs’ response had all major forcings been considered.

IV) Joint response and feedback analysis. Simple, but sufficiently comprehensive, models allow estimating the coupled responses of multiple models of higher complexity. One example are the uncertainties in radiative forcing of well-mixed greenhouse gases, which are to some degree independent from the climate response to the forcing. A simple model could combine forcing and climate response uncertainties by emulating all permutations of AOGCM climate response characteristics and respective radiative transfer scheme results.

Another example relates to the fact that many of the AOGCMs used in the IPCC AR4 were not yet coupled to an interactive carbon cycle and so had to be driven with externally calculated CO₂ concentrations. Thus, in most cases the same CO₂ concentrations were prescribed for a “warmer” and a “colder” AOGCM, despite the fact that the warmer AOGCM is likely to see higher concentrations under the same emission scenario. MAGICC is a coupled gas-cycle/climate model and, as such, includes feedbacks between the carbon cycle and the climate. Hence, for any set of model parameters, MAGICC is internally consistent in that the climate feedbacks on the CO₂ projections will be driven by the climate model output.

This study combines a full range of AOGCM emulations with emulations of the most complete set of carbon cycle models to date (C4MIP, Friedlingstein et al., 2006). Ten of the eleven C4MIP carbon cycle models and their terrestrial and oceanic carbon pools and fluxes are emulated. For the first time, a large set of both carbon cycle and climate models has been emulated individually. This allows a sizeable combined ensemble for each emission scenario with 190 combinations of nineteen emulated AOGCM climate

and ten C4MIP carbon cycle responses, providing a better estimate of uncertainties in the climate projections than would otherwise be possible.

This study presents the most comprehensive AOGCM and carbon cycle model emulation exercise to date. We use an updated version of MAGICC, which was originally developed by Wigley and Raper (1987, 1992) and amended continuously since then (see e.g. Raper et al., 1996; Wigley and Raper, 2001). Several amendments to MAGICC have been spurred by new results presented in IPCC AR4 as well as the increasing availability of comprehensive AOGCM and C4MIP datasets. For example, land/ocean hemispheric temperature evolutions of both hemispheres were calculated for each AOGCM allowing for a more in-depth analysis of optimal heat exchange parameterizations in MAGICC. Of course, emulations with a simple model like MAGICC 6.0 can by no means replace research into more sophisticated carbon cycle and general circulation models. Rather, what MAGICC 6.0 offers is primarily a method to extend the knowledge created with AOGCMs and carbon cycle model runs in order to provide estimates of their joint responses and to extrapolate their key characteristics to a range of other scenarios. This study is partially motivated by the MAGICC 4.2 emulation results presented in IPCC AR4, which showed in average an about 10% warmer response over the period from 1990 to the end of the 21st century for the SRES scenarios, despite closely matching the idealized CO₂-only scenarios.

This paper is structured as follows: Sect. 2 provides a brief overview of the main amendments in the climate model MAGICC 6.0 as used here – compared to the version used in IPCC AR4. The calibration procedures and forcing harmonization for emulating CMIP3 AOGCMs and C4MIP carbon cycle models are described in Sect. 3. The emulation results as well as the effects of the forcing adjustments are provided in Sect. 4. Section 5 discusses the present calibration results, particularly in regard to diagnosed climate sensitivities. In addition, Sect. 5 provides an analysis of calibrations to AOGCM with a previous version of MAGICC, as presented in IPCC AR4. Climate responses to a large set of non-mitigation and mitigation scenarios are provided in Sect. 6. Section 7 summarizes limitations of the present approach, while conclusions

MAGICC 6.0

M. Meinshausen et al.

Title Page

Abstract

Introduction

Conclusions

References

Tables

Figures

◀

▶

◀

▶

Back

Close

Full Screen / Esc

Printer-friendly Version

Interactive Discussion



are given in Sect. 8. A complete description of the MAGICC 6.0 model can be found in Appendix A.

2 Model description

MAGICC has a hemispherically averaged upwelling-diffusion ocean coupled to an atmosphere layer and a globally averaged carbon cycle model. As with most other simple models, MAGICC evolved from a simple global average energy-balance equation. This energy balance equation of the perturbed climate system can be written as:

$$Q_G = \lambda_G \Delta T_G + \frac{dH}{dt} \quad (1)$$

where Q_G is the global-mean radiative forcing at the top of the troposphere. This extra energy influx is partitioned into increased outgoing energy flux and heat content changes in the ocean $\frac{dH}{dt}$. The outgoing energy flux is dependent on the global-mean feedback factor, λ_G , and the surface temperature perturbation ΔT_G .

While MAGICC is designed to provide maximum flexibility in order to match different types of responses seen in more sophisticated models, the approach in MAGICC's model development has always been to derive the simple equations as much as possible from key physical and biological processes. In other words, as simple as possible, as mechanistic as necessary. This process-based approach might be an advantage in comparison to simple statistical fits that are more likely to quickly degrade in their skill when emulating scenarios outside the original calibration space of sophisticated models.

The main improvements in MAGICC 6.0 compared to the version used in the IPCC AR4 are briefly highlighted in this section. The options introduced to account for variable climate sensitivities are described (Sect. 2.1). With the exception of the updated carbon cycle routines (Sect. 2.2), the new parameterizations encompass the IPCC AR4 MAGICC parameterizations as a special case, i.e., the IPCC AR4 version can be retained by appropriate parameter settings.

MAGICC 6.0

M. Meinshausen et al.

Title Page

Abstract

Introduction

Conclusions

References

Tables

Figures

◀

▶

◀

▶

Back

Close

Full Screen / Esc

Printer-friendly Version

Interactive Discussion



2.1 Introduction of variable climate sensitivities

Climate sensitivity (ΔT_{2x}) is a useful metric to compare models and is usually defined as the global-mean equilibrium warming after a doubling of CO₂ concentrations (from pre-industrial levels). Climate sensitivity is inversely related to the feedback factor λ :

$$\Delta T_{2x} = \frac{\Delta Q_{2x}}{\lambda} \quad (2)$$

where ΔT_{2x} is the climate sensitivity, and ΔQ_{2x} the radiative forcing after a doubling of CO₂ concentrations (see energy balance Eq. A46).

The (time- or state-dependent) effective climate sensitivity (S^t) (Murphy and Mitchell, 1995) is defined using the transient energy balance Eq. (1) and can be diagnosed from model output for any part of a model run where radiative forcing and ocean heat uptake are both known and their sum is different from zero, so that:

$$S^t = \frac{\Delta Q_{2x}}{\lambda^t} = \frac{\Delta Q_{2x} \times \Delta T_{GL}^t}{Q^t - \left. \frac{dH}{dt} \right|_t} \quad (3)$$

where ΔQ_{2x} is the model-specific forcing for doubled CO₂ concentration, λ_t is the time-variable feedback factor, Q^t the radiative forcing, ΔT_{GL}^t the global-mean temperature perturbation and $\left. \frac{dH}{dt} \right|_t$ the climate system's heat uptake at time t . By definition, the traditional (equilibrium) climate sensitivity (ΔT_{2x}) is equal to the effective climate sensitivity S^t at equilibrium ($\left. \frac{dH}{dt} \right|_t = 0$) after doubled (pre-industrial) CO₂ concentration.

If there were only one globally homogenous, fast and constant feedback process, the diagnosed effective climate sensitivity would always equal the equilibrium climate sensitivity ΔT_{2x} . However, many CMIP3 AOGCMs exhibit variable effective climate sensitivities, often increasing over time (e.g. models CCSM3, CNRM-CM3, GFDL-CM2.0, GFDL-CM2.1, GISS-EH – see Figs. 16, 17, and 18). This is consistent with earlier results of increasing effective sensitivities found by Senior and Mitchell (2000); Raper et al. (2001) for the HadCM2 model. In addition, some models present significantly

Title Page

Abstract

Introduction

Conclusions

References

Tables

Figures

◀

▶

◀

▶

Back

Close

Full Screen / Esc

Printer-friendly Version

Interactive Discussion



higher sensitivities for higher forcing scenarios (1pctto4x) than for lower forcing scenarios (1pctto2x) (e.g. ECHAM5/MPI-OM and GISS-ER, see Fig. 1).

In order to better emulate these time-variable effective climate sensitivities, this version of MAGICC incorporates two modifications: Firstly, an amended land-ocean heat exchange formulation allows effective climate sensitivities to increase on the path to equilibrium. In this formulation, changes in effective climate sensitivity arise from a geometrical effect: spatially non-homogenous feedbacks can lead to a time-variable effective global-mean climate sensitivity, if the spatial warming distributions change over time. Hence, by modifying land-ocean heat exchange in MAGICC, the spatial evolution of warming is altered, leading to changes in effective climate sensitivities given that MAGICC has different equilibrium sensitivities over land and ocean (Raper, 2004). Secondly, the climate sensitivity, and hence the feedback parameters, can be made explicitly dependent on the current forcing at time t . Both amendments are detailed in the Appendix A (see Sects. A4.2 and A4.3). Although these two amendments both modify the same diagnostic, i.e., the time-variable effective sensitivities in MAGICC, they are distinct: the land-ocean heat exchange modification changes the shape of the effective climate sensitivity's time evolution to equilibrium, but keeps the equilibrium sensitivity unaffected. In contrast, making the sensitivity explicitly dependent on the forcing primarily affects the equilibrium sensitivity value.

Note that time-varying effective sensitivities are not only empirically observed in AOGCMs, but they are necessary here in order for MAGICC to accurately emulate AOGCM results. Even with a constant (best-fit) sensitivity, however, MAGICC is able to provide good (but less than optimal) fits to these more sophisticated models.

Alternative parameterizations to emulate time-variable climate sensitivities are possible, e.g. assuming a dependence on temperatures instead of forcing. However, this study chose to limit the degrees of freedom in respect to time-variable climate sensitivities given that a clear separation into three (or more) different parameterizations seemed speculative based on the AOGCM data analyzed here. Further studies like the recent ones by Andrews and Forster (2008) or Gregory and Webb (2008) on semi-

MAGICC 6.0

M. Meinshausen et al.

Title Page

Abstract

Introduction

Conclusions

References

Tables

Figures



Back

Close

Full Screen / Esc

Printer-friendly Version

Interactive Discussion



direct forcings or instantaneous, fast and longer term adjustment effects to various forcings will help to refine the optimal parameterizations to emulate AOGCMs in the future.

2.2 Updated carbon cycle

5 MAGICC's terrestrial carbon cycle model is a globally integrated box model, similar to that in [Harvey \(1989\)](#) and [Wigley \(1993\)](#). The MAGICC 6.0 carbon cycle can emulate temperature-feedback effects on the heterotrophic respiration carbon fluxes. One improvement in MAGICC 6.0 allows increased flexibility when accounting for CO₂ fertilization. This increase in flexibility allows a better fit to some of the more complex
10 carbon cycle models reviewed in C4MIP ([Friedlingstein et al., 2006](#)) (see Sect. 3.3).

Another update in MAGICC 6.0 relates to the relaxation in carbon pools after a deforestation event. The gross CO₂ emissions related to deforestation and other land use activities are subtracted from the plant, detritus and soil carbon pools (see Fig. 13). While in previous versions only the regrowth in the plant carbon pool was taken into
15 account to calculate the net deforestation, MAGICC 6.0 includes now an effective relaxation/regrowth term for all three terrestrial carbon pools (see Appendix A1.1).

The original ocean carbon cycle model used a convolution representation [Wigley \(1991b\)](#) to quantify the ocean-atmosphere CO₂ flux. A similar representation is used here, but modified to account for nonlinearities. Specifically, the impulse response
20 representation of the Princeton 3-D GFDL model ([Sarmiento et al., 1992](#)) is used to approximate the inorganic carbon perturbation in the mixed layer (see for the impulse response representation [Joos et al., 1996](#)). The temperature sensitivity of the sea surface partial pressure is implemented based on [Takahashi et al. \(1993\)](#) as given in [Joos et al. \(2001\)](#). For details on the updated carbon cycle routines, see Appendix A1.2.

Title Page

Abstract

Introduction

Conclusions

References

Tables

Figures

◀

▶

◀

▶

Back

Close

Full Screen / Esc

Printer-friendly Version

Interactive Discussion



2.3 Other improvements compared to IPCC AR4 version

Five additional amendments to the climate model have been implemented in MAGICC 6.0.

2.3.1 Aerosol indirect effects

5 Relating to tropospheric aerosols, in particular their (rather uncertain) indirect effects, it is now possible to account directly for contributions from black carbon, organic carbon and nitrate aerosols due to indirect (cloud albedo) effects (Twomey, 1977). The so-called second indirect effect, affecting cloud cover or cloud lifetime, can be modeled separately. However, following the convention in IPCC AR4 (Forster et al., 2007), the
10 second indirect effect is by default modeled as a change in efficacy of the first indirect effect. See Sect. A3.6 in the Appendix for details.

2.3.2 Depth-variable ocean with entrainment

Building on the work by Raper et al. (2001), MAGICC 6.0 includes the option of a depth-dependent ocean area profile with entrainment at each of the ocean levels (default, 50
15 levels) from the polar sinking water column. The default ocean area profile decreases from unity at the surface to, for example, 30%, 13% and 0% at depths of 4000, 4500 and 5000 m. Although comprehensive data on depth-dependent heat uptake profiles of the CMIP3 AOGCMs has not been available for this study, this entrainment update provides more flexibility and allows to a better simulation of the characteristic depth-
20 dependent heat uptake as observed in one analyzed AOGCM, namely HadCM2 (Raper et al., 2001).

2.3.3 Vertical mixing depending on warming gradient

Simple models, including earlier versions of MAGICC, sometimes overestimated the ocean heat uptake for higher warming scenarios when applying parameter sets chosen

Title Page

Abstract

Introduction

Conclusions

References

Tables

Figures

◀

▶

◀

▶

Back

Close

Full Screen / Esc

Printer-friendly Version

Interactive Discussion



to match heat uptake for lower warming scenarios, see e.g. Fig. 17b in [Harvey et al. \(1997\)](#). A strengthened thermal stratification and hence reduced vertical mixing might contribute to the lower heat uptake (compared to a case with fixed mixing) for higher warming levels. To compensate for this, a warming-dependent vertical gradient of the thermal diffusivity is implemented here. (Appendix [A4.7](#)).

2.3.4 Forcing efficacies

Since the IPCC TAR, a number of studies have focussed on forcing efficacies, i.e., on the differences in surface temperature response due to a unit forcing by different radiative forcing agents with different geographical and vertical distributions (see e.g. [Joshi et al., 2003](#); [Hansen et al., 2005](#)). This version of MAGICC includes the option to apply different efficacy terms for the different forcings agents (see Appendix [A4.4](#) for details and <http://www.atmos-chem-phys-discuss.net/8/6153/2008/acpd-8-6153-2008-supplement.pdf> for default values).

2.3.5 Radiative forcing patterns

Earlier versions of MAGICC used time-independent (but user-specifiable) ratios to distribute the global-mean forcing of tropospheric ozone and aerosols to the four atmospheric boxes, i.e., land and ocean in both hemispheres. This model structure and the simple 4-box forcing patterns are retained as it can capture a large fraction of the forcing agent characteristics of interest here. However, we now use patterns for each forcing individually, and allow for these patterns to vary over time. For example, the historical forcing pattern evolutions for tropospheric aerosols are based on results from [Hansen et al. \(2005\)](#), which are interpolated to annual values and extrapolated into the future using hemispheric emissions. Additionally, MAGICC 6.0 incorporates now forcing patterns for the long-lived greenhouse gases as well, although these patterns are assumed to be constant in time and scaled with global-mean radiative forcing (<http://www.atmos-chem-phys-discuss.net/8/6153/2008/>

Title Page

Abstract

Introduction

Conclusions

References

Tables

Figures

◀

▶

◀

▶

Back

Close

Full Screen / Esc

Printer-friendly Version

Interactive Discussion



3 Calibration and emulation procedures

In this section, the method used to calibrate MAGICC against CMIP3 AOGCMs and C4MIP carbon cycle models is explained, and forcings employed for “complete-forcing” simulations are described.

3.1 Calibration against CMIP3 AOGCMs

Nineteen of the CMIP3 AOGCMs provided sufficient data on their heat uptake and surface air temperature responses such that MAGICC could be calibrated to their responses. Three distinct calibration exercises are undertaken, optimizing a smaller (I,II) or larger (III) set of MAGICC parameters using idealized scenarios only (I), or optimizing against multi-forcing scenarios as well (II,III). The “calibration I” approach mimics the procedure employed for IPCC AR4. Three key parameters were calibrated to reproduce the idealized 1%/yr increasing CO₂-only scenarios optimally. Secondly, an additional five parameters were optimized (“calibration II”) to match the idealized CO₂-only scenarios better. Thirdly, the most comprehensive calibration exercise (“calibration III”) employs, in addition, the AOGCM results for multi-gas scenarios, viz. the year-2000 constant concentration (commit) experiments, and the SRES B1 and A1B scenarios, if available. The scenario SRES A2 is not used for calibrating MAGICC parameters, but was instead used for verification. See Table 1 for an overview of the three calibration exercises. Going beyond the match of global-mean temperatures and heat uptake, all calibration exercises also took into account hemispheric land and ocean temperatures, diagnosed from one of the ensemble members of each CMIP3 AOGCM (run 1) provided at the PCMDI database (http://www.pcmdi.llnl.gov/ipcc/about_ipcc.php). To take account of model-drift, the corresponding low pass-filtered (1/20 yr⁻¹ cutoff frequency)

Title Page

Abstract

Introduction

Conclusions

References

Tables

Figures

◀

▶

◀

▶

Back

Close

Full Screen / Esc

Printer-friendly Version

Interactive Discussion



control-run segments were subtracted (see Appendix B).

3.1.1 Calibrated parameters

In the first calibration exercise (“calibration I”), only three key parameters were optimized, namely the climate sensitivity ΔT_{2x} , the equilibrium land-ocean warming ratio RLO and the vertical thermal diffusivity Kz in the ocean. Kz has a large influence on the ocean heat uptake efficiency. In the second and third calibration exercises, five additional parameters in MAGICC were optimized to match the AOGCM temperature and heat-uptake results. As in any calibration exercise with multiple parameters, there is the danger of overfitting. Therefore, only a limited set with clearly distinct effects representing different physical mechanisms were chosen out of the large number of MAGICC parameters. Two of the additional five parameters are required to emulate time-varying effective climate sensitivities: namely μ , the ocean to land heat-exchange amplification, which allows the emulation of increasing, but forcing-independent, effective sensitivities (Appendix A4.2); and ξ , the forcing-dependency of feedbacks (see Appendix A4.3). Another parameter, the gradient $\frac{dK_{ztop}}{dT}$, modulates the heat uptake efficiency under higher warming scenarios, by making the vertical diffusivity dependent on the ocean warming (see Appendix A4.7). Furthermore, the two symmetric heat-exchange parameters between land and ocean (k_{LO}) and between the hemispheres (k_{NS}) are calibrated, with the latter having no influence on the global-mean warming, but on the hemispheric warming pattern.

The parameter space in MAGICC is first sampled randomly with 2000 parameter sets. For each parameter set, up to five parallel runs were done, one for each of the fitted scenarios. Subsequently, the best (in a least-squared sense) parameter set is used to initialize an optimization routine with approximately 1000 iterations to find the parameter combination that minimizes the squared differences between lowpass-filtered AOGCM and MAGICC time series of heat uptake, global, northern land, northern ocean, southern land and southern ocean surface air (2 m) tempera-

Title Page

Abstract

Introduction

Conclusions

References

Tables

Figures

◀

▶

◀

▶

Back

Close

Full Screen / Esc

Printer-friendly Version

Interactive Discussion



tures. See Appendix B for details.

3.1.2 Calibration against idealized CO₂ scenarios

In order to successfully emulate the climate response of an AOGCM, its driving forces should be known. This is why idealized experiments, where the forcing is known, are preferred for calibration. For example, MAGICC calibrations for IPCC TAR, as well as feedback parameter calculations by Forster and Taylor (2006), used the first 70 years of the idealized 1% runs. MAGICC 4.2 calibrations for IPCC AR4 used the full-length 1% runs (1pctto2x and 1pctto4x). All 19 CMIP3 AOGCMs considered here provided at least some output for such idealized forcing experiments, assuming annual 1% increases of CO₂ up to doubled and quadrupled concentrations (1pctto2x and 1pctto4x, respectively). Most AOGCMs started these experiment from pre-industrial control runs (picntrl), although four (CCSM3, MRI-CGCM2.3.2, ECHO-G, NCAR PCM) used present-day control runs (pdcntrl). Control-run drift was removed using the respective low pass-filtered (1/20 yr⁻¹ cutoff frequency) control run segments. Assuming that the CO₂ concentration to forcing relationship is logarithmic (IPCC, 1990; Myhre et al., 1998), the forcing is a ramp-function over 70 (140) years up to its forcing level ΔQ_{2x} at doubled (or quadrupled) CO₂ concentrations. ΔQ_{2x} is estimated to be 3.71 Wm⁻² (Myhre et al., 1998), although AOGCMs show a relatively large variation (see Table 10.2 in Meehl et al., 2007). Where available, model-specific ΔQ_{2x} values were used during the calibration exercise (see Tables B1 and B2).

3.1.3 The difficulty posed by unknown radiative forcing

The inherent difficulty with calibrating MAGICC parameters to the multi-forcing output data, and the reason why this approach has not been used previously, is the large uncertainties in the actual forcings. Modeling groups took into account different sets of radiative forcing agents when computing the multi-forcing-agent scenarios. Even

Title Page

Abstract

Introduction

Conclusions

References

Tables

Figures

◀

▶

◀

▶

Back

Close

Full Screen / Esc

Printer-friendly Version

Interactive Discussion



MAGICC 6.0

M. Meinshausen et al.

Title Page

Abstract

Introduction

Conclusions

References

Tables

Figures

◀

▶

◀

▶

Back

Close

Full Screen / Esc

Printer-friendly Version

Interactive Discussion



for the forcings in common, the quantitative information of the actual effective forcings within AOGCMs is rather limited, mostly restricted to CO₂ forcings at doubled CO₂ concentrations. The first study addressing this shortcoming in a comprehensive manner is the one by Forster and Taylor (2006), who diagnosed the effective forcings. Neither forcings nor efficacies can be diagnosed from the currently available AOGCM data without making additional assumptions, though; for example, with regard to the models' effective climate sensitivities (Forster and Taylor, 2006).

In the present study, given these limitations, we use informed guesses for the individual model forcings. Only the matching set of radiative forcing agents (see Table 2) was applied for each AOGCM using default efficacies (see <http://www.atmos-chem-phys-discuss.net/8/6153/2008/acpd-8-6153-2008-supplement.pdf>).

These reconstructed forcing time-series are hence not identical to the diagnosed forcings given by Forster and Taylor (2006). In case of the GISS models, the modeling group provided an independent estimate of the radiative forcing (Hansen, 2005, personal communication as reported in Forster and Taylor, 2006), which agrees well with the net effective forcing series used for calibration here (see Fig. 2b).

A further step in this study provides insights into how the AOGCM responses might have changed if all AOGCMs had used all forcing agents in their integrations. Unifying the starting years of the emulations to 1750, completing the set of forcings, adjusting historical volcanic forcing to a historical zero mean, and coupling an interactive carbon cycle are several steps taken here in the attempt to produce projections. The full-forcing time series applied here in MAGICC differ from the full-forcing time-series applied in MAGICC 4.2 for IPCC AR4 in particular towards the end of the 21st century (see Fig. 2), primarily because of our revised assumption on individual aerosol contributions to the indirect aerosol effects following Hansen et al. (2005) (see Appendix A3.6 for details).

Figure 2 highlights the different forcing series for two of the 19 emulated CMIP3 models. The forcings used in IPCC AR4 for the projections with MAGICC 4.2 (calibrated only to idealized scenarios) are in these two cases higher than the diagnosed forcings by (Forster and Taylor, 2006) (hereafter referred to as “F&T”). Across all AOGCMs, the

mean MAGICC 4.2 forcing series are, however, in close agreement to the respective multi-model means of the diagnosed F&T forcings, as shown in Fig. 9. The “like-with-like” forcings used for calibrations in this study tend to be lower as are the full forcing series used for projections. A more detailed discussion of the MAGICC 4.2 forcing assumptions and emulations can be found in Sect. 5.1 and Fig. 9. Forcing assumptions for MAGICC 6.0 made in this study are presented below. The forcing resulting from these assumptions are compared to the diagnosed F&T forcings in Fig. 7 together with the respective MAGICC 6.0 temperature responses (see Sect. 4.4).

3.1.4 Special cases for multi-forcing calibration

Within the forcing agent sets, MAGICC applies forcing histories whose magnitude from 1750 to 2005 is consistent with the central estimate provided by IPCC AR4 (see <http://www.atmos-chem-phys-discuss.net/8/6153/2008/acpd-8-6153-2008-supplement.pdf> or Table 2.12 in Forster et al., 2007). The four exceptions are:

Firstly, for volcanic forcing, the amplitude was adjusted for each AOGCM that included volcanic forcing, so that the amplitude in net effective (shortwave and longwave) volcanic forcing is approximately matched as detected by Forster and Taylor (2006). A too strong negative amplitude would result in a too high sensitivity ΔT_{2x} , and hence too warm future MAGICC response, because the chosen goodness of fit statistic, the squared differences, give substantial weight to the larger deviations during strong volcanic forcing events. To minimize the effect of mismatching volcanic forcing series a low pass filter was applied within the optimization routine. The scaling factor for volcanic forcing was determined to be lower than unity for all models (ranging from 0.2 for INM-CM3.0 and MRI-CGCM2.3.2 to 0.7 for most models). See Table 2.

Secondly, CO₂ related forcing is modeled slightly differently compared to other forcing agents: as for the idealized scenarios, the parameter that scales CO₂ forcing ΔQ_{2x} is set to its AOGCM-specific value during the calibration exercise (see Eq. A36 and A37). Furthermore, under the assumption that most CMIP3 AOGCMs prescribed CO₂

Title Page

Abstract

Introduction

Conclusions

References

Tables

Figures

◀

▶

◀

▶

Back

Close

Full Screen / Esc

Printer-friendly Version

Interactive Discussion



concentrations according to the Bern reference cases provided in the IPCC TAR, these CO₂ concentration scenarios are prescribed in MAGICC when trying to match the AOGCM output for the SRES scenarios B1 and A1B. Prescribing CO₂ concentrations instead of emissions has the additional benefit of keeping the calibration of the carbon cycle (see following Sect. 3.3) strictly separate from the calibration of the climate response.

Thirdly, a special case is the second indirect aerosol effect, characterized by default in IPCC AR4 (Forster et al., 2007) as an efficacy enhancement to the first indirect aerosol effect. For AOGCMs that only included the first indirect effect (ECHAM5/MPI-OM, ECHO-G, IPSL-CM4, UKMO-HadCM3), the second effect is ignored during the calibration exercise. For the GISS-EH and GISS-ER models, which only included the second indirect effect (see Table 10.1 in Meehl et al., 2007), a forcing was assumed of the same magnitude as IPCC AR4's best estimate of the first indirect aerosol effect (-0.7 Wm^{-2} with efficacy 0.9). For the three models MIROC3.2 (hires), MIROC3.2 (medres) and HadGEM1 that are reported to have included both indirect aerosol effects, the efficacy of the first indirect effect has been assumed as 1.5 (default 0.9; i.e., the second indirect effect is assumed to enhance the first indirect effect by 67%) during the calibration exercise following the (very uncertain) efficacy estimates discussed in IPCC AR4 (see Sect. 2.8.5.5 in Meehl et al., 2007 as well as <http://www.atmos-chem-phys-discuss.net/8/6153/2008/acpd-8-6153-2008-supplement.pdf>).

Fourthly, the last issue relates to the “cold start problem” (Hasselmann et al., 1993). Rather than starting in 1750, the reference year for radiative forcings, modeling groups chose years in between 1850 and 1900 as a starting point for the 20th century integrations (20c3m runs). Unfortunately, it is not documented how (or if) the AOGCM modeling groups handled any forcing differences between 1750 and the respective starting year. For example, in the default forcing series applied here (excluding volcanic forcing), a slight forcing increase of roughly $+0.2 \text{ Wm}^{-2}$ occurred between 1750 and 1860. Modeling groups could have applied a “jump start”, so that the model is subject to a step forcing increase in the starting year (see Fig. 3). Alternatively, models

Title Page

Abstract

Introduction

Conclusions

References

Tables

Figures

◀

▶

◀

▶

Back

Close

Full Screen / Esc

Printer-friendly Version

Interactive Discussion



MAGICC 6.0

M. Meinshausen et al.

Title Page

Abstract

Introduction

Conclusions

References

Tables

Figures

◀

▶

◀

▶

Back

Close

Full Screen / Esc

Printer-friendly Version

Interactive Discussion



could be driven by radiative forcing changes since their starting year only, neglecting any forcing changes between 1750 and their starting year. Judging from their temperature evolutions, it is assumed here that AOGCMs were initialized with zero forcing in their 20c3m starting year, not in regard to 1750, given that no significant temperature increases are apparent in the early 20c3m runs (cf. case “Starting 1860” in Fig. 3). The effect of these different initializations is small in light of the overall projection uncertainties, though still important in order to derive optimal calibrations for individual model response characteristics. For both the climate and carbon cycle models, the only exception is the Hadley C4MIP carbon cycle model, whose temperature evolution suggests that it has been subject to a “jump start” in forcing. Such “jump start” initializations have been used earlier as well—as documented in Johns et al. (1997) (see Fig. 30a therein).

3.2 Harmonizing the forcings

There are substantial uncertainties in the forcing magnitudes and their evolution over time. Here, we ensured that the forcing evolutions for each gas, aerosol or albedo effect, are consistent with the point forcing estimates in year 2005 provided in the IPCC AR4 see <http://www.atmos-chem-phys-discuss.net/8/6153/2008/acpd-8-6153-2008-supplement.pdf> and Table 2.12 in Forster et al. (2007). We also began each emulation case using MAGICC in 1750 (see Fig. 3). An additional change was to adjust the forcing for CO₂. As discussed by Collins et al. (2006), radiative forcing parameterizations in GCMs can result in substantial deviations from the line-by-line radiative transfer schemes. These deviations are, for example, apparent in the ΔQ_{2x} values, with values ranging from 3.09 to 4.06 Wm⁻² across the AR4 AOGCMs (see first column of Table B3). To remove these differences we used a central estimate of 3.71 Wm⁻² (Myhre et al., 1998) consistent with line-by-line models (Collins et al., 2006), although it is recognized that there is some uncertainty in the “true” CO₂ forcing. Finally, instead of using the prescribed CO₂ concentrations, we generated these internally from emissions using each of the ten carbon cycle model calibrations (see

following Sect. 3.3) – thereby replacing the prescribed CO₂ concentrations.

The following paragraph highlights one of the many forcing adjustments, namely the volcanic forcing. Judging from their temperature evolutions, CMIP3 AOGCMs that included a non-zero volcanic forcing (see Table 2), applied volcanic forcing as negative forcing only, which leads to an initial cooling of the global-mean temperatures after the runs branched off from the pre-industrial control simulations. This is an initialization problem, which leads to an artificial cooling of the 20th century simulations (see Fig. 4). Furthermore, rather than prescribing a future cooling according to the historical mean, future volcanic forcing is typically assumed zero in the AOGCMs. This leads to a rebound effect with a slight additional warming for 21st century temperatures relative to the base period 1980–1999. Thus, the AOGCMs which did include volcanic forcing are representing a temperature projection for a volcanic-free future, in which a rebound effect is appropriate, although the cooling after initialization is still problematic. Note that the HadCM3 model data stored at PCMDI seems not to have included volcanic forcings in their IPCC AR4 runs (in contrast to the information provided in Table 10.1 of Meehl et al., 2007). The approach taken here in the emulations after the forcing adjustments, is attempting to provide best-guess future warming projections including natural forcing, i.e., a mean volcanic cooling and a mean solar forcing according to the recent 100-year and 11-year history, respectively. The benefit of adjusting the historical volcanic forcing series to a mean zero is that the initialization problem is addressed. Keeping a future volcanic mean zero has in turn the benefit that the dependence of future projections on past volcanic forcing assumptions is minimized, i.e., there is no rebound effect. Some AOGCMs, e.g. some HadCM3 runs (J. Lowe, personal communication, 2007; see as well Fig. 1 in Stott et al., 2000), do in fact apply volcanic forcing with a historical zero mean and zero future (see Fig. 4).

3.3 Calibrating the carbon cycle

The following section details the procedures for calibrating the MAGICC carbon cycle to ten of the eleven carbon cycle models that took part in the C4MIP intercomparison

Title Page

Abstract

Introduction

Conclusions

References

Tables

Figures

◀

▶

◀

▶

Back

Close

Full Screen / Esc

Printer-friendly Version

Interactive Discussion



project (Friedlingstein et al., 2006).

MAGICC's carbon cycle model (see Fig. 13) was calibrated in two consecutive steps. In a first step, the climate sensitivity (ΔT_{2x}) was derived by prescribing the C4MIP models' CO₂ concentrations (for runs that included temperature feedbacks on the carbon cycle) and calibrating MAGICC's climate sensitivity for default climate module settings to obtain optimal (least squares) agreement with the C4MIP temperature projection (see Table B4). Subsequently, MAGICC's main carbon cycle parameters were adjusted in order to optimally match the C4MIP model-specific carbon fluxes and pool sizes for both the feedback and non-feedback cases (total of 14 time-series).

The initial MAGICC carbon fluxes were obtained from the available C4MIP datasets, specifically the net primary productivity (NPP_{ini}) and total heterotrophic respiration ($\sum R_{ini}$ comprising R , Q_a and U). A constant partitioning (45:55) is assumed for the initial carbon pool sizes of the detritus (D_{ini}), and soil box (S_{ini}), as only the aggregated dead carbon pool is provided for the C4MIP models. C4MIPs initial living carbon pool is equated to MAGICC's plant (P_{ini}) carbon pool. The start year for fertilization and temperature effects has been assumed to be the first year of the available C4MIP dataserie (first model years ranging from 1765 to 1901; see Table B4.)

Using these initial conditions for carbon fluxes and pools, thirteen MAGICC carbon cycle parameters were calibrated. The semi-automatic procedure involves 2000 randomly drawn parameter sets, each run once for the coupled (i.e., including temperature feedbacks) and once for the uncoupled (excluding temperature feedbacks) scenarios. The "best match" parameter set was then chosen as initialization to an automated optimization procedure that fulfils a pre-selected error tolerance criterion after approximately another 1000 iterations. By adjusting the thirteen MAGICC parameters, the procedure minimizes the weighted least-squares differences between MAGICC and 14 available time series; namely, the air-to-land, air-to-ocean, Net Primary Production (NPP), and heterotrophic respiration (R , Q_a and U) fluxes, as well as the living and dead carbon pools and CO₂ concentrations for both the with-feedback and no-feedback runs. See Appendix B for details.

MAGICC 6.0

M. Meinshausen et al.

Title Page

Abstract

Introduction

Conclusions

References

Tables

Figures

◀

▶

◀

▶

Back

Close

Full Screen / Esc

Printer-friendly Version

Interactive Discussion



[Title Page](#)
[Abstract](#)
[Introduction](#)
[Conclusions](#)
[References](#)
[Tables](#)
[Figures](#)
[◀](#)
[▶](#)
[◀](#)
[▶](#)
[Back](#)
[Close](#)
[Full Screen / Esc](#)
[Printer-friendly Version](#)
[Interactive Discussion](#)


The three ocean carbon cycle parameters involved in the calibration are: a) the CO_2 gas exchange rate k (yr^{-1}) between the atmosphere and the upper mixed ocean layer (Eq. A22); b) the temperature sensitivity α_T of the sea surface partial pressure (see Eq. A28); c) a scaling factor γ to scale the impulse response function r'_t for the inorganic carbon perturbation in the mixed layer (so that $r_t = \gamma r'_t / (\gamma r'_t + (1 - r'_t))$) for times lower than one year and a constant scaling factor $\gamma' = (r_{t=1} / r'_{t=1})$ for longer response times, i.e., $r_t = \gamma' r'_t$ for $t > 1$. The transition year for the scaling factor is chosen to match the transition time between the initial polynomial and subsequent exponential expression in the impulse response function representing the 3-D-GFDL model. This particular two-part scaling of the impulse response function has been chosen to allow a linear scaling over medium and long timescales (cf. Fig. 7b in Joos et al., 1996), while ensuring a continuous impulse response function from year zero onwards.

The calibrated terrestrial carbon cycle model parameters determine the flux partition inside MAGICC; namely, the fraction of the plant box flux L going to the detritus box (ϕ_H), the fraction of the detritus box outbound flux Q going to the soil box (q_S). The no-feedback runs were used as well to estimate the fertilization parameters β_m and β_s , where β_m refers to whether a standard lognormal formulation for fertilization is used ($\beta_m = 1.0$), or the rectangular hyperbolic formulation ($\beta_m = 2.0$), or any linear combination of these two formulations ($1.0 < \beta_m < 2.0$). β_s denotes the fertilization factor itself (see Sect. A1.1 and Eq. A20). The temperature feedback parameters σ_i of the carbon fluxes NPP , Q and U (cf. Fig. 13) were estimated by matching the difference between the with-feedback and no-feedback runs.

4 AOGCM calibration results

This section gives the results of the three calibration exercises employed here to replicate the climate response characteristics of the AOGCMs (Sects. 4.1, 4.2, and 4.3). The forcing and temperature effects of the AOGCM-specific forcing adjustments are given in Sect. 4.4. Section 4.5 provides the results of the carbon cycle calibrations.

4.1 Calibration Method I – as in the AR4

Here we fit the idealized CO₂-only scenarios 1pctto2x and 1pctto4x, using only the three most important MAGICC parameters; the equilibrium climate sensitivity (ΔT_{2x}), the equilibrium land-ocean warming ratio (RLO), and the vertical diffusivity in the ocean (Kz) (see Table B1).

This simple calibration approach enables the emulation of the evolution of global-mean temperatures for the idealized scenarios relatively well for most AOGCMs. The root mean square errors (RMSE) between emulations and the AOGCMs are well below 0.2°C for the 1pctto2x and 1pctto4x scenarios for all but four models (UKMO HadGEM1, CCCma CGCM3.1(T47), GFDL CM2.0 and MPI ECHAM5), as shown in Fig. 5a. As can be expected, the SRES and “commit” multi-forcing scenarios are less well emulated for almost all models, as their information was not used to derive the optimal parameter settings for ΔT_{2x} , RLO and Kz . This discrepancy between emulations and AOGCM multi-forcing runs is substantial for three out of the 19 emulations showing RMSE values higher than 0.35°C. On average across all models and scenarios, the RMSE is 0.21°C (see Fig. 5a).

In order to put this RMSE value of 0.21°C in perspective, it is here compared to the equivalent goodness of fit statistic, if a single AOGCM's projections were simply approximated by the global-mean temperature time-series of another randomly drawn AOGCM for the same scenario. This comparison is motivated by the common practice in many studies to make inferences from single AOGCMs, often implying that a single AOGCM is representative for a wider range of other AOGCMs. Thus, for this comparative measure of inter-model uncertainty, we computed the average RMSE between global-mean temperature series for all permutations of CMIP3 AOGCMs applying the same lowpass filter as used for the calibrations (1/20 yr⁻¹ cutoff frequency), taking into account the full overlapping time-periods between any pair of AOGCMs. The resulting RMSE is 0.46°C across the multi-forcing and idealized scenarios, more than twice as high compared to the RMSE of emulations following the “calibration I” procedure.

Title Page

Abstract

Introduction

Conclusions

References

Tables

Figures

◀

▶

◀

▶

Back

Close

Full Screen / Esc

Printer-friendly Version

Interactive Discussion



MAGICC 6.0

M. Meinshausen et al.

[Title Page](#)[Abstract](#)[Introduction](#)[Conclusions](#)[References](#)[Tables](#)[Figures](#)[I◀](#)[▶I](#)[◀](#)[▶](#)[Back](#)[Close](#)[Full Screen / Esc](#)[Printer-friendly Version](#)[Interactive Discussion](#)

It is noticeable that some AOGCMs show features in their idealized scenario runs (1pctto2x and 1pctto4x), that cannot possibly be emulated satisfactorily by only optimizing the three parameters ΔT_{2x} , RLO and Kz . For example, a larger best-fit effective climate sensitivity for the higher forcing 1pctto4x run than for the 1pctto2x run is apparent in the MPI ECHAM5 simulation, after these runs diverge in year 70 of the model integration (see Fig. 1, and discussion in Sect. 5.2). A constant climate sensitivity ΔT_{2x} is thus not able to match both scenarios satisfactorily. The best-fit constant climate sensitivity will be in-between the effective sensitivities for the 1pctto2x and 1pctto4x runs. Indeed, the “calibration I” procedure gives a climate sensitivity of 3.95°C (see Table B1), which is in between the effective sensitivities of 3.5 and 4.2°C towards the end of the 1pctto2x and 1pctto4x scenarios, respectively (see Fig. 1).

4.2 Calibration Method II – using additional parameters

For some AOGCMs, the use of additional parameters in the fitting exercise did not improve the goodness of fit (MIROC3.2(hires), GISS-EH and FGOALS-g1.0). For other, the fit was improved markedly. For example, the RMSE is halved for NCAR CCSM3 and GISS-ER (see 1pctto2x and 1pctto4x scenarios in Fig. 5a and c). The enhanced ability to match the idealized scenarios of the MPI ECHAM5 model is most noticeable: under “Method I”, the RMSE values were 0.30°C and 0.43°C . The idealized scenarios are now emulated with an RMSE of 0.15°C and 0.11°C – primarily due to the ability of MAGICC under “Method II” to simulate time-varying effective sensitivities for the 1pctto2x and 1pctto4x scenarios (see Fig. 1). The idealized scenarios as well as the multi-forcing scenarios are more accurately emulated, so that the goodness of fit ranking for MPI ECHAM5 improved (see Fig. 5).

In summary, the match to the idealized scenarios improved for all those models that provided 1pctto2x and 1pctto4x data. The models where there was no improvement, see above, were those that provided only 1pctto2x data. The emulation skill for the multi-forcing scenarios, which were – as in “calibration I” – not used for “calibration II”, was only slightly enhanced in most cases. The average RMSE across all scenarios

and models is 0.188°C (see Fig. 5a and c), slightly improved from the 0.206°C that resulted from the “calibration I” procedure.

4.3 Calibration Method III – from CO₂-only to multi-forcing

While the inclusion of additional parameters under the “calibration II” procedure markedly improved the fit to the idealized experiments, the performance of the emulations for the multi-forcing runs is still imperfect. Obviously, the emulation quality for SRES scenarios enhances, if a goodness of fit statistic for these SRES scenarios is included in the optimization routine. Analyzing the global-mean as well as the hemispheric land and ocean average temperatures relative to the control run simulations reveals a remarkable consistency between the mean of the emulations and the mean of the AOGCM runs under the “calibration III” strategy (see Fig. 6 and Table 3).

For individual AOGCMs, the deviations over the full scenario duration are small, mostly <0.2°C (see Fig. 5f). The largest deviation in global means of up to 0.5°C is for the model, for which the calibrated MAGICC was least capable of simulating their temperature under the multi-forcing scenarios, namely CNRM CM3. The emulations of CNRM CM3 show most clearly what is apparent as well for eight other AOGCMs (GISS-ER, MIROC3.2 (medres), NCAR PCM1, MPI ECHAM5, MRI CGCM2.3.2A, IPSL-CM4, INM-CM3.0 and HadGEM1), namely that the idealized scenarios are emulated too warm and the multi-forcing runs too cold or vice versa (see Fig. 5f). In the case of CNRM CM3, this likely points to an underestimation of the net forcing in the multi-forcing runs or overestimation of the CO₂ forcing in the idealized scenarios. The average RMSE across all scenarios and models further decreased to 0.172 K, so that the intermodel uncertainty RMSE of 0.46°C is more than 2.5 times higher compared to the uncertainty introduced by the emulations of an individual AOGCM. The mean across all AOGCM emulations compared to the mean of the original AOGCM’s global temperature evolutions has an RMSE of 0.053°C (averaged across all multi-forcing runs 2000–2100). This highlights that the emulations of the multi-model ensemble mean is substantially more robust than emulating a single AOGCM and associated with very

Title Page

Abstract

Introduction

Conclusions

References

Tables

Figures

◀

▶

◀

▶

Back

Close

Full Screen / Esc

Printer-friendly Version

Interactive Discussion



minor biases, if any (see Fig. 6).

As the SRES A2 scenario has not been used for calibration, but left as an independent test case for the validity of the emulations, the emulation skill in comparison to the other multi-forcing runs is of interest. The performance of the emulations for the high SRES A2 scenario is similar to the other two SRES scenarios B1 and A1B that were taken into account for the calibration (average RMSE A2: 0.175°C; A1B: 0.190°C, B1: 0.168°C; see Fig. 5e). This is encouraging as it supports the assumption that emulations for other emissions scenarios approximately reflect what AOGCMs would project.

Again, it is valuable putting these errors introduced by the emulations in perspective. The inter-model uncertainties between AOGCMs in regard to global-mean temperatures towards the end of the 21st century (2090–2099) to SRES scenarios are roughly 40%, when expressed as double standard deviation divided by the multi-model ensemble mean (B1:49%, A1B:41%, A2:26%) (cf. Knutti et al., 2008). In comparison, the mean relative errors introduced by the emulations are substantially smaller, i.e., less than 2.2% for the ensemble means (B1:2.2%, A1B:–1.0%, A2:–0.8%) and, on average, 7% for individual AOGCM emulations over 2090–2099 relative to 1980–1999 (B1:9%, A1B:6%, A2:6%). Comparing these 2090–2099 warmings between emulations and AOGCMs relative to AOGCM starting years reduces differences further, as well because the uncertainties introduced by the strong Pinatubo volcanic forcing in the 1980–1999 base period are circumvented: Individual AOGCMs in the last decade of the 21st century are now matched in average with a mean relative error of only 6% (B1:5%, A1B:5%, A2:7%). The better half of emulation and AOGCM pairs show deviations of only 3% on average (B1:3%, A1B:2%, A2:5%).

4.4 Harmonized forcing results

In this section we consider the effects on temperature that arise because different AOGCMs used different forcings (both historically and in the future), as well as different starting dates. Even if all AOGCMs had the same physics (i.e., the same climate

Title Page

Abstract

Introduction

Conclusions

References

Tables

Figures

◀

▶

◀

▶

Back

Close

Full Screen / Esc

Printer-friendly Version

Interactive Discussion



sensitivity, ocean mixing, etc.), these differences would cause the projected climate changes to diverge. We analyze this effect by applying a common set of forcings to the different MAGICC emulations, model by model, and compare the resulting projections with those that arise when only model-specific forcings are used (see Fig. 2). As a representative example, we consider results for the A1B scenario.

The starting point of the analysis is the set of AOGCM specific “like-with-like” forcings applied for calibrating MAGICC parameters (see Table 2). Comparing the mean of these efficacy-adjusted forcing series used for calibration with the mean of the diagnosed F&T forcings reveals a close match up to the middle of the 21st century (see first sub-panel indicated with black circled “1” in Fig. 7a). Thereafter, the “like-with-like” forcings assumed here turn lower than the diagnosed F&T forcings. This difference might at least partially be due to an overestimation of the effective F&T forcings towards the second half of the 21st century. The reason for the potential overestimation of diagnosed forcings could be that Forster and Taylor (2006) assumed constant climate sensitivities, estimated from the first 70 years of the idealized forcing scenarios. If in fact effective climate sensitivities are increasing in some models over time, this method would lead to an underestimation of the effective climate sensitivity at the end of the 21st century and hence an overestimation of the forcings. There are two factors supporting this hypothesis. Firstly, in the idealized scenarios, for which the forcing is better known, the diagnosis of effective climate sensitivities (see equation 3) reveals increasing climate sensitivities for higher forcing levels for a number of models - as shown in Fig. 1 for CCSM3 and ECHAM5/MPI-OM. Secondly, continuing the analysis by Forster and Taylor (2006) beyond 2100 suggests increasing diagnosed forcings for some models, inconsistent with the fact that forcings should be constant after 2100 by definition of the scenarios (Meehl et al., 2005a).

The close match between the A1B forcings assumed here and the diagnosed F&T forcings up to the middle of the 21st century is reflected in a close match of the global-mean temperatures. Also, the emulated mean temperature perturbations in MAGICC 6.0 using the “like-with-like” forcings are within 0.1°C of the AOGCM mean throughout

[Title Page](#)[Abstract](#)[Introduction](#)[Conclusions](#)[References](#)[Tables](#)[Figures](#)[I◀](#)[▶I](#)[◀](#)[▶](#)[Back](#)[Close](#)[Full Screen / Esc](#)[Printer-friendly Version](#)[Interactive Discussion](#)

the whole emulation period, which tends to support our forcing assumptions compared to the diagnosed F&T forcings (see black circled “1” in Fig. 7b). Relative to the base period 1980–1999, the difference in projected warming for 2090–2099 between the MAGICC emulations and the AOGCMs is 0.02°C or less than 1% (cf. column AOGCM and IIIa for “Period 2” in Table 3).

One of the difficulties interpreting the AOGCM results for the past is that modelling groups assumed different starting years, in which the 20th century simulations (20c3m) diverge from the pre-industrial control runs. Unifying these starting years to 1750 shifts the forcing to higher values. This is because the forcing increments of CO₂ and other considered forcing agents between 1750 and the starting years, e.g. 1850 or 1900, are now taken into account (see Fig. 3 and “2” in Fig. 7a). Had all AOGCMs started their simulations in 1750, their temperature projections for the 21st century could be expected to be approximately 0.1°C warmer relative to 1750 (see “2” in Fig. 7b), although this effect almost vanishes when taking differences to the 1980–1999 base period (see “2” in Fig. 7c).

In the next step, all AOGCM emulations were now run with complete and unified forcings. Specifically, if an AOGCM had left out a specific forcing agent (e.g. indirect aerosol effects or tropospheric ozone), the climate module has been calibrated by taking account of this omission. Completing and unifying the missing sets of radiative forcing agents in each AOGCM simulation (see Table 2), unifying the CO₂ forcing ($\Delta Q_{2x}=3.71 \text{ Wm}^{-2}$) and adjusting the historical volcanic forcing to a zero mean has a significant effect on the applied forcing (see “3” in Fig. 7a).

These numerous forcing adjustments have obviously a pronounced effect on the emulated temperatures. Relative to the starting years of the emulations, the temperatures drop by around 0.4°C for much of the 21st century (see “3” in Fig. 7b). However, when taking differences to the base period 1980–1999, the 21st century temperatures only cool by 0.1°C in average (see “3” in Fig. 7c). Hence, the partial omission of aerosol effects and volcanic forcings did not result in a significant projection error for 21st AOGCM temperature projections under the SRES A1B scenario in IPCC AR4,

[Title Page](#)[Abstract](#)[Introduction](#)[Conclusions](#)[References](#)[Tables](#)[Figures](#)[◀](#)[▶](#)[◀](#)[▶](#)[Back](#)[Close](#)[Full Screen / Esc](#)[Printer-friendly Version](#)[Interactive Discussion](#)

where a base period of 1980–1999 has been applied.

Running the AOGCM emulations coupled with the carbon cycle calibrations for the future overcomes the inconsistency that warmer AOGCMs were using the same prescribed CO₂ concentrations as colder AOGCMs. By combining each CMIP3 AOGCM with each of the C4MIP emulations, the coupled AOGCM carbon cycle emulations yield in average a 0.2 Wm⁻² additional forcing (see “4” in Fig. 7a), resulting in an additional warming of roughly 0.1°C by the end of the 21st century (see “4” in Fig. 7 b and c).

The sum of all forcing adjustments (see “5” in Fig. 7a) is characterized by additional forcings of around 0.25 Wm⁻² until 1970 interspersed by negative spikes reflecting the unaccounted part of volcanic coolings in the past. After 1970, the forcing adjustments approximately offset each other and start turning negative, dominated by the volcanic forcings spikes. After year 2000, when the zero-mean “spiky” volcanic forcing time series changes into a smooth zero-mean future time series, the net negative cooling effect of 0.2–0.3 Wm⁻² becomes apparent, mainly due to the adjustments for partially omitted aerosol effects, moderated by the positive forcing shift due to the unification of the starting years. Up to 2000, the positive volcanic forcing largely masked this effect. For global-mean temperatures, the net effect of the forcing adjustments is a cooling after around 1970 and throughout the 21st century (see “5” in Fig. 7b). Relative to the base period 1980–1999, the net temperature effect is positive up to 1963, the volcanic eruption of Mt Agung. Furthermore, the warming in the early 20st century after the eruption of Krakatoa in year 1883, is increased by around 0.2°C (see “5” in Fig. 7c).

Emulating the other SRES scenarios beyond A1B confirms that the “like-with-like” forcing emulations (Illa) are resulting in a very close match of the original AOGCM data, with deviations of maximally 2.2% for SRES B1 by the end of the 21st century (cf. the columns “AOGCM” and “Illa” for “Period 2” in Table 3). Note though, that difference to the ‘year 2000 concentration stabilization’ (commit) scenarios are larger (mean –0.1°C). The “commit” scenarios are challenging to emulate, as different AOGCMs show a wide range of 20th century temperature evolutions with, for some models, relatively strong short-term variability. In combinations with very different concentration

Title Page

Abstract

Introduction

Conclusions

References

Tables

Figures

◀

▶

◀

▶

Back

Close

Full Screen / Esc

Printer-friendly Version

Interactive Discussion



levels held constant after year 2000, the inter-model differences in unrealized warming at the end of the 20th century manifests itself in a rather wide spread of temperatures under the “commit” scenario (0.17°C to 1.0°C by 2090–2099 relative to 1980–1999).

In case of the SRES A2 scenario, not all models provided integrations, in particular not the MIROC 3.2 (hires) AOGCM, the “warmest” among all CMIP3 AOGCMs. Thus, adjusting the SRES A2 mean by accounting for all models results in a slight shift of the mean 21st warming upward by 0.09°C. Additionally, a general feature of the forcing harmonization is that the emulated warming up to the end of the 20st century is generally reduced, while the 21st warming is rather unaffected. Not surprisingly, the largest radiative forcing adjustment effects are related to those AOGCMs that left out significant forcing agents, such as indirect aerosol forcing effects (e.g. CCSM3, CGCM3.1(T47), CSIRO-MK3.0, FGOALS-g1.0, GFDL-CM2.0 etc. – see Table 2) and the high aerosol scenario SRES A2 (see Table 3). In case of SRES A2, the 0.09°C additional warming noted above due to the inclusion of all AOGCMs, is overcompensated by additional cooling due to aerosols, resulting in a net downward adjustment of 0.1°C for the 21st century (see Table 3). Furthermore, an effect of similar magnitude compared to the forcing adjustments is due to the choice of the reporting period. While in IPCC TAR, results were stated for 2100, IPCC AR4 choose the 2090–2099 period, which results in a lowering of the stated temperatures by up to 0.25°C under the SRES A2 scenario (see “Period 3” in Table 3).

4.5 Carbon cycle calibration results

MAGICC has been successfully calibrated against ten of the C4MIP carbon cycle models. C4MIP used CO₂ emissions in line with the SRES A2 scenario. We have used 14 time series with and without temperature feedbacks for calibration. Results are given in Fig. 8, Fig. 19 in Appendix B and Table B4. The overall range across C4MIP models of 2100 CO₂ concentrations (732 to 1025 ppm) is well matched by the emulations (732 ppm to 1012 ppm). For the no-feedback case, errors in 2100 concentration range between –15 and +15 ppm (RMSE=9ppm, not shown in Table B4). For the with-

Title Page

Abstract

Introduction

Conclusions

References

Tables

Figures

◀

▶

◀

▶

Back

Close

Full Screen / Esc

Printer-friendly Version

Interactive Discussion



feedback case, errors in 2100 range between -23 and $+2$ ppm (RMSE=10 ppm). The match with the IPSL CM2C model in the with-feedback case is the least optimal: a maximal deviation of 2.9% or 23 ppm for 2100 CO₂ concentrations (see Table B4). Over 2000 to 2100, the RMSE, averaged across the models, is 3.5 ppm when emulating atmospheric CO₂ concentrations.

The additional uncertainty introduced by the emulations is more than a magnitude smaller than the C4MIP intermodel spread: the mean over the squared difference between all with-feedback C4MIP pairs of 21st century and 2100 CO₂ concentrations is 38.4 ppm and 128 ppm, respectively, which would be the average error (RMSE) introduced if one models' CO₂ concentration were simply approximated by another carbon cycle model's projection, not the emulation. While the optimization procedure placed the largest weights on fitting atmospheric CO₂ concentrations, the six other available C4MIP time series were also well matched for each model, namely the terrestrial C-uptake, oceanic C-uptake, Net Primary Production (NPP), terrestrial living C-pool, terrestrial dead C-pool and the total respiration (see Fig. 8 and Fig. 19 in Appendix B).

5 Discussion of emulation results including those in IPCC AR4

This section discusses two issues: For comparison and historical context, the MAGICC 4.2 emulations presented in IPCC AR4 are briefly discussed (Sect. 5.1), including the reasons why the mean emulations were approximately 10% warmer over the 21st century compared to the CMIP3 AOGCM data. Furthermore, Sect. 5.2 compares the effective climate sensitivities of the CMIP3 AOGCMs derived in this study with other estimates and slab ocean equilibrium climate sensitivities.

5.1 Why were MAGICC IPCC AR4 results 10% warmer than CMIP3 AOGCMs?

The MAGICC 6.0 “calibration I” procedure follows the approach taken during the preparation of IPCC AR4 using MAGICC 4.2 (see Table 1). Both calibration methods yield

Title Page

Abstract

Introduction

Conclusions

References

Tables

Figures

◀

▶

◀

▶

Back

Close

Full Screen / Esc

Printer-friendly Version

Interactive Discussion



MAGICC 6.0

M. Meinshausen et al.

[Title Page](#)[Abstract](#)[Introduction](#)[Conclusions](#)[References](#)[Tables](#)[Figures](#)[◀](#)[▶](#)[◀](#)[▶](#)[Back](#)[Close](#)[Full Screen / Esc](#)[Printer-friendly Version](#)[Interactive Discussion](#)

very similar climate sensitivity estimates for all AOGCMs (see Table 4, columns 4 and 5). One exception is the HadGEM1 model, where the present study benefited from additional data for the 1pctto4x run, not available at the time of calibrating MAGICC 4.2. This leads to a 0.5°C larger climate sensitivity estimate in the MAGICC 6.0 calibration. In addition to the improved model structure, MAGICC 6.0 calibrations benefited from complete hemispheric land/ocean AOGCM data sets allowing a more accurate determination of the land/ocean warming characteristics for all models.

In an Appendix on sea level rise in IPCC AR4, Sect. 10.A.1 (p. 844), it is said that the “average of the tuned versions of MAGICC gives about 10% greater temperature rise [...] than the corresponding AOGCMs”. In assessing these differences, IPCC goes on to say that, because the MAGICC forcings are similar to F&T (assumed to be an accurate representation of the AOGCM forcings), these differences “suggest(s) there may be structural limitations on the accurate emulation of AOGCMs” by MAGICC. An actual analysis of why MAGICC 4.2 emulations were warmer for SRES scenarios (despite matching the idealized CO₂-only scenarios optimally in a least square sense) is thus of interest. It could be the case that the climate sensitivity of MAGICC 4.2 was set higher than appropriate – maybe indeed due to “structural limitations” in MAGICC 4.2 and earlier versions. However, if the extra warming turns out to be due to forcing differences, the warmer MAGICC response might even represent a correction to the AOGCM temperature prediction as these did not account for all forcings. As discussed below, it turns out that the answer is likely to be a combination of the two effects.

5.1.1 Comparing forcings

SRES projections with the calibrated MAGICC 4.2 model were calculated by assuming a central forcing estimate of all major forcings listed in Table 2.12 of Forster et al. (2007). This central forcing estimate certainly differed from the average of the (largely unknown) forcing series actually effective in the AOGCMs. As a check on the MAGICC 4.2 forcings, we compare them to the forcings diagnosed by Forster and Taylor (2006) (F&T), noting that these forcings might be underestimated because of the constant

sensitivity assumption employed by these authors.

The most obvious difference is a higher forcing in MAGICC 4.2 from 1850 to 1970, starting to diminish thereafter (see black circled “1” in subpanel of Fig. 9a). There are two reasons for this: Firstly, MAGICC 4.2 applied forcings from 1750 for all models, while many AOGCMs branched off the pre-industrial control runs later. Secondly, MAGICC 4.2 applied volcanic forcings differently: an historical volcanic forcing (Ammann et al., 2007) with relatively high amplitudes was used and the forcing series was adjusted to have a zero mean (shift by around $+0.2 \text{ Wm}^{-2}$). As aforementioned, the CMIP3 AOGCMs seem to have applied volcanic forcing only as a strictly negative forcing, if at all, leading to a slight initial cooling (cf. Fig. 4).

A more detailed explanation for the forcing differences between MAGICC 4.2 and the diagnosed F&T forcings follows: Forcing differences start to diminish after around 1970 and are small by the beginning of the 21st century (“2” in Fig. 9a). The likely cause is a more pronounced negative forcing of aerosols in MAGICC 4.2 compared to the average of the AOGCMs, of which only 9 models included indirect aerosol effects. Furthermore, in year 2000, the MAGICC 4.2 forcing has a step in order to account for zero-mean future volcanic warming matching the zero-mean historical volcanic forcing (see Fig. 4 and discussion in Sect. 3.2). Towards the end of the 21st century, applied forcings in MAGICC 4.2 increase again above the diagnosed F&T AOGCM forcings, partially due to adjustments of the CO_2 forcing strength (“4”) to a central 3.71 Wm^{-2} estimate for doubled CO_2 forcing, and partially due to the application of the low and high carbon cycle feedback estimates, which cause on average an increase of applied forcings (“5”).

Both the forcings in MAGICC 4.2 and the diagnosed F&T forcings are likely to be higher than the actually effective forcings in the AOGCMs towards the end of the 21st century (see “3” in Fig. 9a). We expect the MAGICC forcing to show a larger increase between 1980–1999 to the end of the 21st century due to the rebound effect of decreasing aerosol concentrations not included in many AOGCM forcings. In MAGICC 4.2, the fact that the indirect aerosol effect was modeled solely as a function of SO_x aerosols

MAGICC 6.0

M. Meinshausen et al.

Title Page

Abstract

Introduction

Conclusions

References

Tables

Figures

◀

▶

◀

▶

Back

Close

Full Screen / Esc

Printer-friendly Version

Interactive Discussion



contributed to this rebound, as SRES SO_x emissions are assumed to decline faster than nitrate or other aerosol emissions. For the diagnosed F&T forcings, there might be an overestimation due to increasing effective climate sensitivity in some AOGCMs, as detailed above (see Sect. 4.4). F&T assumed constant climate sensitivities.

5.1.2 Comparing temperatures

While MAGICC 4.2 shows – in line with the forcing differences – a higher warming initially in the 20th century, the warming rate is lower than in the AOGCMs after approximately 1970 until the beginning of the 21st century (see “6” and “7” in Fig. 9). As noted above, towards the end of the 21st century, the mean warming exhibited by the calibrated MAGICC 4.2 exceeds the mean AOGCM warming (by $\approx 10\%$).

A base period between 1900–1970 would have reduced the future temperature differences by about half, although MAGICC 4.2 would have exhibited cooler temperatures around the year 2000. Thus, half of the additional warming in MAGICC 4.2 relative to the CMIP3 AOGCMs and their 1980–1999 base period could be due to the aerosol rebound effect.

The other half of the additional warming in MAGICC 4.2 could be caused by too high sensitivities in the calibrated MAGICC 4.2 for the multi-forcing agent AOGCM runs. That is because the MAGICC 4.2 calibration attempted to find a constant climate sensitivity to match as well the rather high-forcing part of the idealized scenarios 1pctto4x, where some AOGCMs exhibit increased effective climate sensitivities.

The correction of the CO₂ forcing strength, using a default ΔQ_{2x} parameter of 3.71 Wm^{-2} has a small influence on the mean temperature evolution (see Fig. 9b). A slight additional warming is noticeable, if the uncertainty in the carbon cycle feedbacks is taken into account – averaging across low, mid and high carbon cycle feedback settings, that were applied for IPCC AR4 (“10”).

In summary, a major reason for MAGICC4.2 results being warmer than the average AOGCM projection is the difference between the AOGCM-specific incomplete forcing series and the full forcing series applied in MAGICC 4.2. To some extent, this difference

Title Page

Abstract

Introduction

Conclusions

References

Tables

Figures

◀

▶

◀

▶

Back

Close

Full Screen / Esc

Printer-friendly Version

Interactive Discussion



therefore represent a correction to the AOGCM results. The accuracy of this correction is, of course, limited by the realism of the applied forcings in MAGICC 4.2, in particular for aerosol induced forcings. On top of that, the calibrated climate sensitivities in MAGICC 4.2 were probably on average higher than appropriate for the low-forcing part of the SRES scenarios. The successful emulations of AOGCMs using MAGICC 6.0 in the present study show that there are no inherent structural limitations such that simple models are not able to accurately emulate AOGCMs.

5.2 Comparison of climate sensitivities

Equilibrium climate sensitivity is a useful aggregate model indicator and climate system characteristic. Therefore, the climate sensitivities derived here are briefly compared to other published estimates for the set of CMIP3 AOGCMs (see Table 4). Many modelling groups reported equilibrium warming results with their slab ocean model versions, stated in the first column of Table 4 taken from Meehl et al. (2007). The average climate sensitivity across all slab-ocean models is 3.21°C. For multiple reasons, the coupled model versions can exhibit different sensitivities, because the presence of a coupled ocean can alter atmospheric feedbacks (Gregory et al., 2004). Time-evolving effective climate sensitivities S^t can be diagnosed from any transient run for which the forcing and ocean heat uptake is known, as given in Eq. (3) (see Murphy and Mitchell, 1995; Raper et al., 2001; Senior and Mitchell, 2000). Gregory et al. (2004) employed a regression technique to estimate the effective climate sensitivity even if the absolute forcing is unknown. Forster and Taylor (2006) calculated climate sensitivities for the CMIP3 AOGCMs from the first 70 years of the idealized 1pctto2x scenarios. The average climate sensitivity following this procedure is nearly half a degree cooler than that estimated for the slab-ocean models (cf. first and second column in Table 4).

MAGICC4.2 climate sensitivity results presented in IPCC AR4 and those for MAGICC 6.0 using calibration Method “I” are very similar (less than 0.2°C difference), except for HadGEM1, for which additional AOGCM data were available in the MAGICC 6.0 case. For 13 out of 19 AOGCMs, these sensitivities are very similar to these in F&T, with

Title Page

Abstract

Introduction

Conclusions

References

Tables

Figures

◀

▶

◀

▶

Back

Close

Full Screen / Esc

Printer-friendly Version

Interactive Discussion



MAGICC 6.0

M. Meinshausen et al.

[Title Page](#)[Abstract](#)[Introduction](#)[Conclusions](#)[References](#)[Tables](#)[Figures](#)[◀](#)[▶](#)[◀](#)[▶](#)[Back](#)[Close](#)[Full Screen / Esc](#)[Printer-friendly Version](#)[Interactive Discussion](#)

differences less than 0.2°C . For the remaining six models analyzed by both studies, MAGICC calibrations give higher climate sensitivities, most notably for the MIROC3.2 (hires) model. The MAGICC result of around 6.0°C is 2.0°C higher than estimated by Forster and Taylor (2006). While the relatively short period (70 yrs) of available data for the 1pctto2x run limits the ability to make definite estimates of the effective climate sensitivity of MIROC3.2(hires), the exceptionally high temperature projections for the SRES A1B and B1 scenarios support the findings of a climate sensitivity around 6.0°C rather than 3.9°C , consistent with the “calibration III” results. An alternative explanation is that the SRES A1B and B1 forcing used by MIROC3.2(hires) could be exceptionally high as hypothesized by Forster and Taylor (2006). The ΔQ_{2x} forcing for this model is however reported as rather low (see Table B1).

Four additional climate sensitivities are estimated to be higher than stated by Forster and Taylor (2006), namely those for CCSM3, MPI ECHAM5, GISS-EH, GISS-ER. These models exhibit increasing effective climate sensitivities over time, so calibration of a fixed sensitivity over only the first 70 years of a 1pctto2x run will lead to an underestimate. Lastly, the ECHO-G model is estimated to have a higher climate sensitivity than suggested by Forster and Taylor (2006) possibly due to erroneous ECHO-G heat uptake data used in the present study. While the 1pctto2x scenario suggests a heat uptake efficiency or vertical ocean thermal diffusivity $K_z \geq 2 \text{ cm}^2 \text{ s}^{-1}$, the best estimate for the vertical diffusivity under the SRES runs was more than five times smaller ($K_z = 0.43 \text{ cm}^2 \text{ s}^{-1}$ – cf. Tables B3 and B1, B2). Thus, for the “calibration III” procedure, where the ECHO-G 1pctto2x heat uptake data was excluded due to this data inconsistency, the climate sensitivity suggested by Forster and Taylor (2006) is approximately confirmed (2.6°C).

Using the “calibration II” procedure, the estimated climate sensitivity ΔT_{2x} is slightly lower for eight AOGCMs compared to “calibration I”. This is largely explained by the increasing sensitivity over time in these models, a factor not accounted for in calibration method “I”. Thus, as should be expected, the differences between “calibration I” results and the sensitivities by Forster and Taylor (2006) are largely reconciled now under

method “II”, since Forster and Taylor (2006) used the relatively low-forcing scenario segments up to doubled CO₂ concentrations to regress the climate sensitivity.

The increases in effective climate sensitivities found in the present analysis confirm earlier results that the effective climate sensitivity seems often to be dependent on the climate state (see e.g. Murphy and Mitchell, 1995; Raper et al., 2001; Senior and Mitchell, 2000; Stouffer, 2004). For five AOGCMs the climate sensitivity estimate increased slightly when comparing the “calibration I” to the “calibration II” results given in Table 4. For these AOGCMs, the data suggests no forcing dependent feedback factors ($\xi=0$). However, for some of these models, the calibration suggests an increasing climate sensitivity over time, parameterized by a heat exchange enhancement factor ($\mu>1$). In this case, the transient effective sensitivity of the emulations is smaller than the equilibrium sensitivity, so that the best-fit equilibrium sensitivity is estimated to be higher. Some of these calibrations to AOGCMs suggest (as well) a decreased heat uptake efficiency for higher warmings ($\frac{dK_{ztop}}{dT} \leq 0$). Thus, the warming can now be allowed to increase further compared to “calibration I” procedure for those AOGCMs, where an overestimation of heat uptake did previously suggest a cooler warming response being optimal.

The climate sensitivity estimates under the “calibration III” procedure are not uniformly higher or lower when compared to “calibration II” estimates. The average sensitivity estimate decreases slightly, though. This could point towards a hypothesis that effective forcings or efficacies under multi-gas scenarios are slightly overestimated in average – or those in the idealized CO₂ scenarios are underestimated. However, the potential over- or underestimations of forcings vary from AOGCM to AOGCM: in five out of the nineteen AOGCMs, multi-forcing runs are emulated warmer than the idealized scenarios, in contrast to seven AOGCMs, where idealized CO₂-only emulations are warmer (see Fig. 5f).

Title Page

Abstract

Introduction

Conclusions

References

Tables

Figures

◀

▶

◀

▶

Back

Close

Full Screen / Esc

Printer-friendly Version

Interactive Discussion



6 Application: emulating temperatures for SRES and mitigation pathways

The main advantage of being able to emulate key quantities of AOGCMs on the one side and carbon cycle models on the other, is that these emulations can now be combined and performed for a series of emissions scenarios. Although climate sensitivity was calibrated for the C4MIP models, all climate response parameter values, including climate sensitivity, were superseded by the AOGCM calibrated values. Using MAGICC 6.0 and prescribing each of the ten carbon cycle parameter sets (Table B4) for each of the nineteen AOGCM parameter sets (Table B3), yields 190 emulations for any one emission scenario.

The assumption that each of the AOGCMs or each of the C4MIP models should be given equal weight, is certainly a simplification as it does not account for the different skills by these models and their structural dependence (for a discussion, see [Tebaldi and Knutti, 2007](#)). Such an “equal likelihood” assumptions affects both the uncertainty range and the ensemble means, with the latter often portrayed as “best estimates” ([Meehl et al., 2007](#)). In the absence of appropriate weights that would capture the individual models’ projection skill and interdependence, a second-best approach seems to continue the tradition of reporting unweighted ensemble means. There are two advantages in giving the multi-model average results. Apart from characterizing the overall performance of a range of models, there is strong evidence that ensemble means outperform individual models for various performance metrics (see e.g. [Tebaldi and Knutti, 2007](#), and references therein). If all models were equally likely to be “correct”, then the resulting ensemble of 190 emulations could be interpreted as a probability distribution. In fact though, the distributions spanned by the 190 emulations simply denote distributions of occurrences or ensembles of opportunity – a measure of uncertainty that arises from inter-model differences. These “ensembles of opportunity” are a collection of “best-guesses” made by each modeling group rather than an attempt to explore the extremes of the uncertainty range. Ensembles of opportunity are therefore more likely to under than overestimate the actual uncertainty.

ACPD

8, 6153–6272, 2008

MAGICC 6.0

M. Meinshausen et al.

Title Page

Abstract

Introduction

Conclusions

References

Tables

Figures

◀

▶

◀

▶

Back

Close

Full Screen / Esc

Printer-friendly Version

Interactive Discussion



MAGICC 6.0

M. Meinshausen et al.

[Title Page](#)[Abstract](#)[Introduction](#)[Conclusions](#)[References](#)[Tables](#)[Figures](#)[◀](#)[▶](#)[◀](#)[▶](#)[Back](#)[Close](#)[Full Screen / Esc](#)[Printer-friendly Version](#)[Interactive Discussion](#)

Comparing the 21st century temperature evolutions of these 190 combined emulations with the original AOGCM data yields a relatively good agreement, despite the numerous forcing adjustments for obtaining a unified and complete set of forcings in the emulations (see Fig. 10). Compared to the mean evaluated temperature evolution above 1980–1999, the 5th percentile of the emulations is 31% lower, the 95th percentile 43% higher, when averaging the results for 2050, 2075 and 2100 for the SRES scenarios (see Table 5).

The right-skewed nature of the distribution, i.e., the fact that the upper bound of the 90th percentile range is roughly 1.5 times further from the mean compared to the lower bound, compares well with the expert judgement of –40% to +60% for a likely confidence range provided in IPCC AR4 based on multiple lines of evidence (Meehl et al., 2007). Note that the IPCC AR4 ranges were denoted as “likely”, meaning 66% to 90% confidence that the real temperature evolution would fall in that range.

The 90% ranges spanned by the emulations here are, however, narrower compared to the “likely” IPCC AR4 range. This is consistent with the fact that the emulation results do not account for forcing uncertainties. Furthermore, the fact that the CMIP3 AOGCM and C4MIP carbon cycle sets do not span the complete range of plausible climate and carbon cycle responses supports the larger uncertainty ranges provided by IPCC AR4 (cf. Knutti et al., 2008). For example, independent estimates of climate sensitivity uncertainties (Meehl et al., 2007; Hegerl et al., 2007) find wider uncertainty ranges than the purely AOGCM-based range used here – as one would expect given that what we have here is a limited “ensemble of opportunity”.

Finally, it is now possible to extend the scenario space to mitigation scenarios and pathways. One of the limitations in the IPCC AR4 WG1 is that only results for non-mitigation scenarios were provided. While some idealized long-term CO₂-only stabilization profiles have been assessed by EMICS, they hardly provide useful information for the 21st century climate with mitigation action. Here, we compute temperature implications for 25 SRES scenarios, which provided complete multi-gas emission sets. In addition, a set of more recent multi-gas mitigation scenarios provided by energy-

system and economic models (van Vuuren et al., 2008¹) is analyzed. Furthermore, EQW mitigation pathways EQWS400Ce, EQWS450Ce and EQWS550Ce, as used in Meinshausen (2006) and Stern (2006) are analyzed – in addition to an EQW pathway that halves global greenhouse gas emissions by 2050 relative to 1990 as described in UNDP (2007).

Except for the “Year 2000 concentration stabilization” experiment (cf. Meehl et al., 2005b; Wigley, 2005), none of the SRES and analyzed mitigation scenarios stay below +2°C relative to pre-industrial levels in every single of these 190 AOGCM and C4MIP emulations at the global-mean. However, the lower mitigation pathways and scenarios have a median expectation below +2°C, if all 190 simulations were judged equally likely (see Fig. 11). By 2100, the median Northern Hemisphere land temperatures are roughly 40% higher than global-mean temperatures – rather independent of the chosen scenario.

7 Limitations

This section briefly summarizes some limitations that should be kept in mind when using the emulation results.

Firstly, limitations arise in the original AOGCMs and C4MIP models themselves. Even if an emulation technique were able to perfectly match the mean responses over a wide range of scenarios, emulations can not mimic the ‘real world’ any better than the original models. Clearly, for some areas, there are still significant developments to be expected in the realism of both climate and carbon cycle models. For example, the current state-of-the-art carbon cycle models themselves face substantial uncertain-

¹van Vuuren, D., Meinshausen, M., Plattner, G. K., Joos, F., Strassmann, K., Smith, S., Wigley, T. M. L., Raper, S. C. B., Riahi, K., de la Chesnaye, F., den Elzen, M., Fujino, J., Kejun, J., Nakicenovic, N., Paltsev, S., and Reilly, J.: Stabilization of 21st Century Climate, Proceedings of the National Academy of Sciences (PNAS), submitted, 2008.

Title Page

Abstract

Introduction

Conclusions

References

Tables

Figures

◀

▶

◀

▶

Back

Close

Full Screen / Esc

Printer-friendly Version

Interactive Discussion



ties, related to, for example, nitrate-fertilization, modeling of fire regimes, ocean-bottom chemistry, etc.

A second limitation arises from the incomplete knowledge on the quantitative (patterns of) forcings that each AOGCM was subject to, which limits our ability to extract the characteristic AOGCM responses to forcing correctly. A consequence of this is that calibrations will over- or under-estimate the climate feedbacks of an AOGCM. Suppose, for example, that an AOGCM includes the first indirect aerosol effect resulting in an effective radiative forcing of -0.4 Wm^{-2} by 2005 relative to 1750, and that MAGICC attempts to emulate this AOGCM using the IPCC AR4 best-estimate effective forcing of -0.7 Wm^{-2} . MAGICC will then underestimate the temperature response of that AOGCM over the historical period, if the climate sensitivity were not adjusted upwards. The calibrated MAGICC sensitivity would then be too high. Not being able to fully exclude such compensation effects due to incomplete knowledge of the forcings, this compensation is clearly suboptimal but might be the best choice at present. A potential solution to the forcing uncertainties problem might be to calibrate MAGICC using independently-derived, but model-specific forcings, such as forcings derived by Forster and Taylor (2006). Unfortunately, this would lead to a circular analysis. Forster and Taylor (2006) had to assume a climate sensitivity to back out the forcings from temperature and heat-uptake/flux imbalance time series. Hence, MAGICC would simply optimize the parameters, so that the effective climate sensitivity would closely match the constant climate sensitivity estimated by Forster and Taylor (2006).

Thirdly, there are uncertainties as to how AOGCM and carbon cycle models would behave for scenarios outside the tested range. Although the SRES A2 AOGCM response was successfully emulated without having been used for calibration, the extrapolation of the calibration results faces inherent uncertainties. For example, the C4MIP intercomparison was constrained to only CO_2 from one single emission scenario, SRES A2, for the time-horizon up to 2100. It is still an open research question, how the carbon cycle might react to, for example, peaking scenarios with increasing, then decreasing radiative forcings or how the dynamics might change in the long-term,

MAGICC 6.0

M. Meinshausen et al.

Title Page

Abstract

Introduction

Conclusions

References

Tables

Figures

◀

▶

◀

▶

Back

Close

Full Screen / Esc

Printer-friendly Version

Interactive Discussion



beyond 2100. Nevertheless, the choice of a relatively medium-high emission scenario SRES A2 was useful, as it somewhat constraints the upper bound on how large carbon cycle feedbacks could be – during the 21st century at least. Future intercomparison projects would certainly benefit using a range of low and high scenarios - allowing to better gauge the dynamical responses to a range of futures. Earlier (but similar) versions of MAGICC successfully emulated other carbon cycle models over a wide range of scenarios (Wigley et al., 2007).

Fourthly, MAGICC 6.0, by virtue of its model structure, must be limited to a subspace of the possible climate and carbon cycle responses. The model-by-model comparisons between the emulations of key variables and the original AOGCM and C4MIP data did not reveal any major structural biases or limitations in the improved MAGICC 6.0, though (see Figs. 16, 17, 18 and 19). However, those structural limitations might only become apparent if the calibrations had been done for a wider range of scenarios, particularly in the case of the carbon cycle models.

Fifthly, the calibration procedure itself is subject to limitations. For example, due to the complexity of the AOGCM data, there may be errors in the data used for calibration (see noted example related to ECHO-G data in Sect. 5.2). Furthermore, for ocean heat uptake data we used both the net integrated ocean heat uptake as well as the total radiative flux at the top of the atmosphere if the former data were not available; introducing small errors due to the effect of the land and cryosphere heat uptake. For the C4MIP carbon cycle calibration procedure, one limitation is that global-mean temperature is taken as the proxy for changes in the patterns of temperature, precipitation, cloudiness etc., which are the true driving forces in more sophisticated carbon cycle models as well as the real world.

Finally, the range of projections presented here account only for climate and carbon cycle model parameter uncertainties and do not account for radiative forcing uncertainties associated with, for example, aerosol forcing uncertainties. Future advancements in the understanding of aerosol indirect effects will hopefully allow for more extensive coverage and realism of these effects within AOGCMs

MAGICC 6.0

M. Meinshausen et al.

[Title Page](#)[Abstract](#)[Introduction](#)[Conclusions](#)[References](#)[Tables](#)[Figures](#)[◀](#)[▶](#)[◀](#)[▶](#)[Back](#)[Close](#)[Full Screen / Esc](#)[Printer-friendly Version](#)[Interactive Discussion](#)

and hence their emulations. Overall, this study presents projections based on forcing evolutions consistent with the point-estimates of forcing provided by IPCC AR4 for the year 2005 (see <http://www.atmos-chem-phys-discuss.net/8/6153/2008/acpd-8-6153-2008-supplement.pdf>). Probabilistic projections would include these forcing uncertainties (cf., for example, [Wigley and Raper, 2001](#)).

8 Conclusions

In the preparation of the IPCC AR4, various resource constraints meant that only limited inter-model comparisons and syntheses were possible, both for AOGCMs and carbon cycle models. The question arises, therefore, as to how to make best use of the existing, AR4-related climate and carbon cycle model data sets, particularly with regard to their application to a wider range of emission scenarios. A carefully calibrated model of lower complexity, which accounts realistically for key earth system components, and which is sufficiently flexible to emulate large-scale quantities for the broad range of more sophisticated models, is likely the most appropriate way. Thus, a simple coupled gas-cycle/climate model can function as an elaborated interpolation and (to a limited extent) extrapolation tool.

We have presented here an updated version of the simple gas-cycle/climate model, MAGICC, with enhanced representations of time-varying climate sensitivities, carbon cycle feedbacks, aerosol forcings and ocean heat uptake characteristics. Calibrated to emulate the responses of 19 CMIP3 AOGCMs, MAGICC 6.0 has been shown here to closely reproduce the global-mean and hemispheric land/ocean temperature changes for idealized and SRES multi-gas emissions scenarios. We have shown that, for any given SRES emission scenario, the intermodel uncertainties in regard to global-mean temperatures towards the end of the 21st century (2090–2099) are roughly $\pm 40\%$ (cf. [Knutti et al., 2008](#)). In comparison, the errors introduced by the emulations are substantially smaller, i.e., below 2.2% for the multi-model mean and, on average, 7% for the individual AOGCM models.

Title Page

Abstract

Introduction

Conclusions

References

Tables

Figures



Back

Close

Full Screen / Esc

Printer-friendly Version

Interactive Discussion



MAGICC 6.0

M. Meinshausen et al.

[Title Page](#)[Abstract](#)[Introduction](#)[Conclusions](#)[References](#)[Tables](#)[Figures](#)[◀](#)[▶](#)[◀](#)[▶](#)[Back](#)[Close](#)[Full Screen / Esc](#)[Printer-friendly Version](#)[Interactive Discussion](#)

Similarly, emulations for the C4MIP carbon cycle models were able to closely reproduce carbon pools, fluxes and atmospheric CO₂ concentrations. For example, when calibrated, and when climate feedbacks on the carbon cycle are included, MAGICC 6.0 emulates 2100 CO₂ concentrations for individual C4MIP models with a 10 ppm deviation (RMSE), which is more than a magnitude smaller than the intermodel range of variation (128 ppm RMSE). Thus, MAGICC 6.0 is well suited for emulating AOGCM and carbon cycle model responses for a variety of research purposes.

In addition, a simple model can help us to understand the behavior of and differences between AOGCMs. For example, MAGICC 6.0 has shown here, confirming earlier studies, that the effective climate sensitivity varies over time in many AOGCMs. As a specific example, we have shown that sensitivities estimates based on only the first 70 years of idealized 1% scenarios may be unrepresentative of longer time periods. We have also demonstrated that equilibrium sensitivities based on slab ocean versions of specific AOGCMs can differ noticeably from effective sensitivities derived from transient experiments (see Table 4).

In the present study we have been able to unify the results of a range of AOGCMs used in the IPCC AR4 to investigate their responses to common forcing scenarios. Direct AOGCM results are disparate because different models used different combinations and magnitudes of the suite of important forcing agents. These differences lead to ambiguities as to whether differences in climate responses are truly due to different climate responses or simply an expression of different forcing assumptions. With its new flexible structure and automated calibration procedures, MAGICC 6.0 is now well equipped to assist future AOGCM and carbon cycle model intercomparison exercises in a timely manner. However, it seems vital that the effective forcing fields in each AOGCM are extracted from the integrations and provided to the modeling community – not least to allow more transparent intercomparisons. The separation between climate response uncertainties, forcing uncertainties and emissions uncertainties is impossible without such forcing diagnostics.

In summary, simple coupled gas-cycle/climate models like MAGICC 6.0, provided

they are properly calibrated over a wide range of emissions scenarios against more complex climate and gas cycle models, serve as useful tools for the analysis, extension and synthesis of the results from large model inter-comparison exercises. Furthermore, these models allow us to greatly expand the range of emissions scenarios that can be produced with AOGCMs, primarily because of the high computational demands of such models. Scientist, policy analysts and decision makers involved in the study and assessment of climate impacts, and adaptation and mitigation strategies, rely heavily on physical climate system projections that go beyond single-model, single-scenario studies. Emulation tools like MAGICC provide an important facility, therefore, of benefit to both the research and stakeholder communities.

Appendix A

MAGICC model description

This Appendix provides a detailed description of MAGICC 6.0 and its different modules (see Fig. 12). Specifically, subsections describe MAGICC's carbon cycle (Sect. A1), the atmospheric-chemistry parameterizations and derivation of non-CO₂ mixing abundances (Sect. A2), radiative forcing routines (Sect. A3), and the climate module to get from radiative forcing to hemispheric (land and ocean, separately) and global-mean temperatures (Sect. A4), as well as oceanic heat uptake. Finally, details are provided on the implementation scheme for the upwelling-diffusion-entrainment ocean climate module (Sect. A5). A technical upgrade is that MAGICC 6.0 has been re-coded in Fortran95, updated from previous Fortran77 versions.

A1 The Carbon cycle

A change in atmospheric CO₂ mixing ratio, χCO_2 , is determined by CO₂ emissions from fossil and industrial sources (E_{fossil}), other directly human-induced CO₂ emis-

Title Page

Abstract

Introduction

Conclusions

References

Tables

Figures

◀

▶

◀

▶

Back

Close

Full Screen / Esc

Printer-friendly Version

Interactive Discussion



sions from or removals to the terrestrial biosphere (E_{Iu}), the contribution from oxidized methane of fossil fuel origin (E_{fCH_4}), the flux due to ocean carbon uptake (F_{ocn}) and the net non-‘directly human-induced’ carbon uptake or release by the terrestrial biosphere (F_{terr}) due to CO_2 fertilization and climate feedbacks. Hence, the budget Eq. (A1) for a change in atmospheric CO_2 concentrations is:

$$\frac{\Delta \chi CO_2(t)}{\Delta t} = E_{foss}(t) + E_{Iu}(t) + E_{fCH_4}(t) - F_{ocn}(t) - F_{terr}(t) \quad (A1)$$

A1.1 Terrestrial carbon cycle

The terrestrial carbon cycle is modeled with three boxes, one living plant box P (see Fig. 13) and two dead biomass boxes, of which one is for detritus H and one for organic matter in soils S. The plant box comprises woody material, leaves/needles, grass, and roots, but does not include the rapid turnover part of living biomass, which can be assumed to have a zero lifetime on the timescales of interest here (dashed extension of plant box P in Fig. 13). Thus, a fraction of gross primary product (GPP) cycles through the plant box directly back to the atmosphere due to autotrophic respiration and can be ignored (dashed arrows). Only the remaining part of GPP, namely the net primary production (NPP) is simulated. The NPP flux is channeled through the “rapid turnover” part of the plant box and partitioned into carbon fluxes to the remainder plant box (default $g_P=35\%$), detritus ($g_H=60\%$) and soil box ($g_S=1-g_P-g_H=5\%$).

The plant box has two decay terms, litter production L and a part of gross deforestation D_{Iu}^P . Litter production is partitioned to both the detritus ($\phi_H=98\%$) and soil box ($\phi_S=1-\phi_H=2\%$). Thus, the mass balance for the plant box is:

$$\Delta P / \Delta t = g_P NPP - R - L - D_{gross}^P \quad (A2)$$

The detritus box has sources from litter production ($\phi_H L$) and sinks to the atmosphere due to landuse (D_{Iu}^H), non-landuse related oxidization (Q_A), and a sink to the

[Title Page](#)
[Abstract](#)
[Introduction](#)
[Conclusions](#)
[References](#)
[Tables](#)
[Figures](#)
[◀](#)
[▶](#)
[◀](#)
[▶](#)
[Back](#)
[Close](#)
[Full Screen / Esc](#)
[Printer-friendly Version](#)
[Interactive Discussion](#)


soil box (Q_S); the mass balance for the detritus box is thus

$$\Delta H/\Delta t = g_H \text{NPP} + \phi_H L - Q_A - Q_S - D_{lu}^H \quad (\text{A3})$$

The soil box has sources from litter production ($\phi_S L$), the detritus box (Q_S) and fluxes to the atmosphere due to landuse (D_{gross}^S), non-landuse related oxidization (U); the mass balance for the soil box is thus

$$S/\Delta t = g_S \text{NPP} + \phi_S L + Q_S - U - D_{lu}^S \quad (\text{A4})$$

The decay of each pool (L, Q and U) are assumed to be proportional to the P, H and S box masses, respectively. The turnover times τ_P , τ_H and τ_S are determined by the initial steady-state conditions for box sizes and fluxes.

$$L_0 = P_0/\tau_0^P \quad (\text{A5})$$

$$Q_0 = H_0/\tau_0^H \quad (\text{A6})$$

$$U_0 = S_0/\tau_0^S \quad (\text{A7})$$

Constant relaxation times τ ensure that the box masses will relax back to their initial sizes if perturbed by a one-off land use change related carbon release or uptake – assuming no changes in fertilization and temperature feedback terms. This relaxation acts as an effective re-growth term so that deforestation $\Sigma D_{\text{gross}} = D_{\text{gross}}^P + D_{\text{gross}}^H + D_{\text{gross}}^S$ represents the gross land use emissions, related to net landuse emissions E_{lu} by re-growth $\Sigma G = G^P + G^H + G^S$

$$\Sigma D_{\text{gross}} - \Sigma G = E_{lu} \quad (\text{A8})$$

$$D_{\text{gross}}^P - G^P = d_P E_{lu} \quad (\text{A9})$$

$$D_{\text{gross}}^H - G^H = d_H E_{lu} \quad (\text{A10})$$

$$D_{\text{gross}}^S - G^S = d_S E_{lu} \quad (\text{A11})$$

Title Page

Abstract

Introduction

Conclusions

References

Tables

Figures

◀

▶

◀

▶

Back

Close

Full Screen / Esc

Printer-friendly Version

Interactive Discussion



Gross landuse related emissions might be smaller (compared to a case where relaxation times are assumed constant) as some human landuse activities, e.g. deforestation, can lead to persistent changes of the ecosystems over the time scales of interest, thereby preventing full regrowth to the initial state P_0 , H_0 or S_0 . A factor ψ is introduced in MAGICC 6.0, stating the fraction that will not regrow ($0 \leq \psi \leq 1$). Thus, the relaxation times τ are made time-dependent according to the following equation:

$$\tau^P(t) = \left(P_0 - \psi \int_0^t d_P E_{lu}(t') dt' \right) / L_0 \quad (\text{A12})$$

$$\tau^H(t) = \left(H_0 - \psi \int_0^t d_H E_{lu}(t') dt' \right) / Q_0 \quad (\text{A13})$$

$$\tau^S(t) = \left(S_0 - \psi \int_0^t d_S E_{lu}(t') dt' \right) / U_0 \quad (\text{A14})$$

Formulation for CO_2 fertilization

CO_2 fertilization indicates the enhancement in net primary production (NPP) due to elevated atmospheric CO_2 concentration. As described in Wigley (1993), there are two common forms used in simple models to simulate the CO_2 fertilization effect: a) the logarithmic form (fertilization parameter $\beta_m=1$) and b) the Michaelis-Menton, rectangular hyperbolic or sigmoidal growth function ($\beta_m=2$) (see e.g. Gates, 1985). The Michaelis-Menton formulation provides more realistic results for both low and high concentrations so that NPP does not rise unlimitedly as CO_2 concentrations increase. While in previous versions, MAGICC employed as default the second Michaelis-Menton formulation, it now allows to use a linear combination of both formulations ($1 \leq \beta_m \leq 2$).

The classic logarithmic fertilization formulation calculates the enhancement of NPP as being proportional to the logarithm of the change in CO_2 concentrations C above the preindustrial level C_0 :

$$\beta_{\log} = (1 + \beta_s \ln(C/C_0)) \quad (\text{A15})$$

Title Page

Abstract

Introduction

Conclusions

References

Tables

Figures

◀

▶

◀

▶

Back

Close

Full Screen / Esc

Printer-friendly Version

Interactive Discussion



The rectangular hyperbolic or sigmoidal growth parameterization for fertilization is given by

$$N = \frac{C - C_b}{1 + b(C - C_b)} = \frac{N_0(C_0 - C_b)(1 + b(C_0 - C_b))}{(C_0 - C_b)(1 + b(C - C_b))} \quad (\text{A16})$$

5 where N_0 is the net primary production and C_0 the CO_2 concentrations at pre-industrial conditions, C_b the concentration value at which NPP is zero (default setting: $C_b=31$ ppm, see [Gifford, 1993](#)).

10 For better comparability with models using the logarithmic formulation, the CO_2 fertilization factor β_s expresses the NPP enhancement due to a CO_2 increase from 340 ppm to 680 ppm, valid under both formulations. Thus, MAGICC first determines the NPP ratio r for a given β_s fertilization factor according to:

$$r = \frac{N(680)}{N(340)} = \frac{N_0(1 + \beta_s \ln(680 \text{ ppm}/C_0))}{N_0(1 + \beta_s \ln(340 \text{ ppm}/C_0))} \quad (\text{A17})$$

Following from here, b in Eq. (A16) is determined by

$$b = \frac{(680 \text{ ppm} - C_b) - r(340 \text{ ppm} - C_b)}{(r - 1)(680 \text{ ppm} - C_b)(340 \text{ ppm} - C_b)} \quad (\text{A18})$$

15 which can in turn be used in Eq. (A16) to calculate the effective CO_2 fertilization factor β_{sig} at time t as

$$\beta_{\text{sig}}(t) = \frac{1/(C_0 - C_b) + b}{1/(C(t) - C_b) + b} \quad (\text{A19})$$

Title Page

Abstract

Introduction

Conclusions

References

Tables

Figures

◀

▶

◀

▶

Back

Close

Full Screen / Esc

Printer-friendly Version

Interactive Discussion



MAGICC 6.0 allows for an increased flexibility, as any linear combination between the two fertilization parameterizations can be chosen ($1 \leq \beta_m \leq 2$), so that the effective fertilization factor β_{eff} is given by:

$$\beta_{\text{eff}}(t) = (2 - \beta_m)\beta_{\text{log}} + (\beta_m - 1)\beta_{\text{sig}} \quad (\text{A20})$$

The CO_2 fertilization effect affects NPP so that $\beta_{\text{eff}} = \text{NPP}/\text{NPP}_0$. MAGICC's terrestrial carbon cycle does furthermore apply the fertilization factor on one of the heterotrophic respiration fluxes R that cycles through the detritus box, which makes up 18.5% of the total heterotrophic respiration ($\sum R = R + U_a + Q$) at the initial steady-state.

Temperature effect on respiration and decomposition

global-mean temperature increase is taken as a proxy for climate-related impacts on the carbon cycle fluxes induced by temperature, cloudiness or precipitation regime changes. Those impacts are commonly referred to as carbon cycle feedbacks as the resulting changes in CO_2 fluxes again affect the climate. Here, the terrestrial carbon fluxes NPP, and the heterotrophic respiration/decomposition fluxes R, Q and U are scaled assuming an exponential relationship,

$$F_i(t) = F'_i(t) \cdot \exp(\sigma_i \Delta T(t)) \quad (\text{A21})$$

where $\Delta T(t)$ is the temperature above a reference year level, e.g. for 1990 or 1900, and F'_i (F_i) stands for the (feedback-adjusted) fluxes NPP, R, Q and U. The parameters σ_i (K^{-1}) are their respective sensitivities to temperature changes. In order to model the actual change in those fluxes Q and U, the relaxation times τ for the detritus and soil pool are adjusted, respectively. Landuse CO_2 emissions in many emission scenarios (e.g. SRES, [Nakicenovic and Swart, 2000](#)) reflect the net directly human-induced emissions. At each time-step, the gross landuse emissions are subtracted from the plant, detritus and soil carbon pools. The difference between net and gross landuse emissions is the CO_2 uptake due to regrowth, e.g. due to historical perturbations of the

Title Page

Abstract

Introduction

Conclusions

References

Tables

Figures

◀

▶

◀

▶

Back

Close

Full Screen / Esc

Printer-friendly Version

Interactive Discussion



carbon pools by deforestation. Thus, a separation between directly human-induced (deforestation related emissions) and indirectly human-induced effects (regrowth) on the carbon cycle is required. As both regrowth and the temperature sensitivity are modeled by adjusting the turnover times, a no-feedback case is computed separately, retrieving the regrowth, then calculating the feedback-case including the formerly calculated regrowth.

A1.2 Ocean carbon cycle

For modeling the perturbation of ocean surface dissolved inorganic carbon, an efficient impulse response substitute for the 3-D-GFDL model [Sarmiento et al. \(1992\)](#) is incorporated into MAGICC. The applied analytical representation of the pulse response function is provided in Appendix A.2.2 of [Joos et al. \(1996\)](#).

The sea-to-air flux F_{ocn} is determined by the partial pressure differential for CO_2 between the atmosphere χCO_2 and surface layer of the ocean ρCO_2 (in units of ppm and μatm , respectively)

$$F_{\text{ocn}} = k(\chi\text{CO}_2 - \rho\text{CO}_2) \quad (\text{A22})$$

where k is the global average gas exchange coefficient (see [Joos et al., 2001](#)). This exchange coefficient is here calibrated to the individual C4MIP carbon cycle models (default value $(7.66 \text{ yr})^{-1}$). The perturbation in dissolved inorganic carbon in the surface ocean $\Delta\Sigma\text{CO}_2(t)$ at any point t in time is obtained from the convolution integral of the mixed layer impulse response function r_s and the net air-to-sea flux F_{ocn} :

$$\Delta\Sigma\text{CO}_2(t) = \frac{c}{hA} \left\{ \int_{t_0}^t F_{\text{ocn}}(t') r_s(t - t') dt' \right\} \quad (\text{A23})$$

(A24)

The impulse response function r_s is given for the time immediately after the impulse injection ($< 1 \text{ yr}$) by (see Appendix A.2.4 of [Joos et al., 1996](#)):

Title Page

Abstract

Introduction

Conclusions

References

Tables

Figures

◀

▶

◀

▶

Back

Close

Full Screen / Esc

Printer-friendly Version

Interactive Discussion



$$r_s(t) = 1.0 - 2.2617t + 14.002t^2 - 48.770t^3 + 82.986t^4 - 67.527t^5 + 21.037t^6 \quad (\text{A25})$$

and for $t \geq 1$ year is given by:

$$r_s(t) = \sum_{i=1}^6 \gamma_i e^{-\tau_i t} \quad (\text{A26})$$

5 with the partitioning γ and relaxation τ coefficients:

$$\gamma = \begin{bmatrix} 0.01481 \\ 0.70367 \\ 0.24966 \\ 0.066485 \\ 0.038344 \\ 0.019439 \end{bmatrix}, \tau = \begin{bmatrix} 0 \\ 1/0.70177 \\ 1/2.3488 \\ 1/15.281 \\ 1/65.359 \\ 1/347.55 \end{bmatrix} \quad (\text{A27})$$

The relationship between the perturbation to dissolved inorganic carbon $\Delta \Sigma \text{CO}_2(t)$ and ocean surface partial pressures $\Delta \rho \text{CO}_2(T_0)$ (expressed in ppm or μatm) at preindustrial temperature level T_0 is given by the Eq. (A24) in Joos et al. (2001). Furthermore, the temperature-sensitivity effect on CO_2 solubility and hence oceanic carbon uptake is parameterized with a simple exponential expression. The modeled partial pressure $\rho \text{CO}_2(t)$ increases with sea surface temperatures according to:

$$\rho \text{CO}_2(t) = [\rho \text{CO}_2(t_0) + \Delta \rho \text{CO}_2(T_0)] \exp(\alpha_T \Delta T) \quad (\text{A28})$$

15 where α_T (default $\alpha_T = 0.0423 \text{ K}^{-1}$) is the sensitivity of the sea surface partial pressure to changes in temperature (ΔT) away from the preindustrial level (see Eq. A25 in Joos et al., 2001, based on Takahashi et al., 1993).

Title Page

Abstract

Introduction

Conclusions

References

Tables

Figures

◀

▶

◀

▶

Back

Close

Full Screen / Esc

Printer-friendly Version

Interactive Discussion



A2 Non-CO₂ mixing abundances

This section provides the employed formulas in the step from emissions to concentrations, whereas the next Sect. (A3) does provide details on the derivation of radiative forcing.

5 A2.1 Methane

Natural emissions of methane are inferred by balancing the budget for a user-defined historical period, e.g. from 1980–1990, so that

$$E_{\theta}^n = \theta(\Delta C_{\theta} - C_{\theta'} / \tau_{\text{tot}}) - E_{\theta}^f - E_{\theta}^b \quad (\text{A29})$$

where E_{θ}^n , E_{θ}^f and E_{θ}^b are the average natural, fossil and landuse related emissions, respectively; θ is the conversion factor between atmospheric concentrations and emissions. $C_{\theta'}$ (and ΔC_{θ}) are the average (annual changes in) concentrations. The net atmospheric lifetime being τ_{tot} is in case of methane the net atmospheric lifetime, consisting of time-dependent tropospheric, soil and other (e.g. stratospheric) sink components according to

$$15 \quad \frac{1}{\tau_{\text{tot}}} = \frac{1}{\tau_{\text{tropos}}} + \frac{1}{\tau_{\text{soil}}} + \frac{1}{\tau_{\text{other}}} \quad (\text{A30})$$

The feedback of methane upon tropospheric OH and its own lifetime follows the results of the OxComp work (tropospheric oxidant model comparison) (see [Ehhalt et al., 2001](#), in particular Table 4.11), which provides simple parameterizations for simulating complex three-dimensional atmospheric chemistry models. As default, tropospheric OH abundances are assumed to decrease by 0.32% for every 1% increase in CH₄. The change in tropospheric OH abundances is thus modeled as:

$$\Delta \ln(\text{tropOH}) = S_{\text{CH}_4}^{\text{OH}} \Delta \ln(\text{CH}_4)$$

Title Page

Abstract

Introduction

Conclusions

References

Tables

Figures

◀

▶

◀

▶

Back

Close

Full Screen / Esc

Printer-friendly Version

Interactive Discussion



$$+S_{\text{NO}_x}^{\text{OH}} E_{\text{NO}_x} + S_{\text{CO}}^{\text{OH}} E_{\text{CO}} + S_{\text{VOC}}^{\text{OH}} E_{\text{VOC}} \quad (\text{A31})$$

where S_x^{OH} is the sensitivity of tropospheric OH towards CH_4 , NO_x , CO and VOC , with default values of -0.32 , $+0.0042$, $-1.05\text{e-}4$ and $-3.15\text{e-}4$, respectively. Increases in tropospheric OH abundances decrease the tropospheric lifetime τ' of methane (default 9.6 yrs^{-1}), which is approximated as a simple exponential relationship

$$\tau'_{\text{CH}_4, \text{tropos}} = \tau_{\text{CH}_4, \text{tropos}}^0 \exp \Delta \ln(\text{tropOH}) \quad (\text{A32})$$

Approximating the temperature sensitivity of the net effect of tropospheric chemical reaction rates, the tropospheric lifetime of CH_4 is adjusted:

$$\tau_{\text{CH}_4, \text{tropos}} = \frac{\tau_{\text{CH}_4, \text{tropos}}^0}{\frac{\tau_{\text{CH}_4, \text{tropos}}^0}{\tau'_{\text{CH}_4, \text{tropos}}} + S_{\tau_{\text{CH}_4}} \Delta T} \quad (\text{A33})$$

where $S_{\tau_{\text{CH}_4}}$ is the sensitivity coefficient upon temperature ΔT (default $S_{\tau_{\text{CH}_4}} = 3.16\text{e-}2$).

A2.2 Nitrous oxide

As for methane, natural nitrous oxide emissions are estimated by a budget Eq. A29. For nitrous oxide however, the average concentrations $C_{\theta'} = C_{\theta-3}$ are taken for a period shifted by 3 years to account for a three year delay of transport of tropospheric N_2O to the main stratospheric sink. The feedback of the atmospheric burden $C_{\text{N}_2\text{O}}$ of nitrous oxide upon its own lifetime is approximated by:

$$\tau_{\text{N}_2\text{O}} = \tau_{\text{N}_2\text{O}}^0 \left(\frac{C_{\text{N}_2\text{O}}}{C_{\text{N}_2\text{O}}^0} \right)^{S_{\tau_{\text{N}_2\text{O}}}} \quad (\text{A34})$$

where $S_{\tau_{\text{N}_2\text{O}}}$ is the sensitivity coefficient (default $S_{\tau_{\text{N}_2\text{O}}} = -5\text{e-}2$) and the superscript "0" indicates a pre-industrial reference state.

Title Page

Abstract

Introduction

Conclusions

References

Tables

Figures

◀

▶

◀

▶

Back

Close

Full Screen / Esc

Printer-friendly Version

Interactive Discussion



A2.3 Tropospheric aerosols

Due to their short atmospheric residence time, changes in hemispheric abundances of aerosols are approximated by changes in their hemispheric emissions. historical emissions of tropospheric aerosols are extended into the future either by emission scenarios (SO_x, NO_x, CO) or, if scenario data is not available, with proxy emissions. As many other emission scenarios, the harmonized IPCC SRES scenarios do not provide black (BC) and organic carbon (OC) emissions. Hence, various ad-hoc scaling approaches have been applied, often scaling BC and OC synchronously (Takemura et al., 2006), sometimes linearly with CO₂ emissions. The MESSAGE emission scenario modeling group is one of the few explicitly including BC and OC emissions in their multi-gas emission scenarios (Rao et al., 2005; Rao and Riahi, 2006). By analyzing MESSAGE scenarios, a scaling factor was derived for this study in relation to carbon monoxide emissions (CO), varying linearly in time to 0.4 by 2100 relative to current BC/CO or OC/CO emission ratios.

A2.4 Halogenated gases

The derivation of mixing ratios of halogenated gases controlled under either the Kyoto or Montreal Protocol assumes constant lifetimes, as in the IPCC/TEAP Special Report Metz et al. (2005) or WMO2006 Ozone Assessment (WMO, 2006). The mixing ratio $M_{t,i}$ for the beginning of each year t is updated according to:

$$M_{t+1,i} = \tau_i E_{t,i} \frac{\rho_{\text{atm}}}{m_{\text{atm}} \mu_i} (1 - e^{-\frac{1}{\tau_i}}) + M_{t,i} (1 - e^{-\frac{1}{\tau_i}}) \quad (\text{A35})$$

where τ_i is the lifetime, $E_{t,i}$ the average emissions of gas i throughout the year t , ρ_{atm} the average density of air, m_{atm} the total mass of the atmosphere (Trenberth and Guillemot, 1994), and μ_i is the mass per mol of the gas i .

Title Page

Abstract

Introduction

Conclusions

References

Tables

Figures

◀

▶

◀

▶

Back

Close

Full Screen / Esc

Printer-friendly Version

Interactive Discussion



A3 Radiative forcing

The following section highlights the key parameterizations taken for estimating the radiative forcing due to human-induced changes in greenhouse gas concentrations, tropospheric ozone and aerosols. The radiative forcing applied in MAGICC is in general the forcing at tropopause level after stratospheric temperature adjustment. Efficacies of the forcings, as discussed by Hansen et al. (2005) and Meehl et al. (2007) can be applied.

A3.1 Carbon dioxide

Taking into account the “saturation” effect of CO₂ forcing, i.e., the decreasing forcing efficiency for a unit increases of CO₂ concentrations with higher background concentrations, the first IPCC Assessment (IPCC, 1990) presented the simplified expression of the form:

$$\Delta Q_{\text{CO}_2} = \alpha_{\text{CO}_2} \ln(C/C_0) \quad (\text{A36})$$

where ΔQ_{CO_2} is the adjusted radiative forcing by CO₂ (Wm⁻²) for a CO₂ concentration C (ppm) above the pre-industrial concentration C₀ (278 ppm). This expression proved to be a good approximation, although the scaling parameter α_{CO_2} has since been updated to a best-estimate of 5.35 Wm⁻² ($= \frac{3.71}{\ln(2)} \text{Wm}^{-2}$) (Myhre et al., 1998), used as default in MAGICC. When applying AOGCM specific CO₂ forcing, α_{CO_2} is set to:

$$\alpha_{\text{CO}_2} = \frac{\Delta Q_{2x}}{\ln(2)} \quad (\text{A37})$$

A3.2 Methane and nitrous oxide

Methane and nitrous oxide have overlapping absorption bands so that higher concentrations of the one gas will reduce the effective absorption by the other and vice versa.

Title Page

Abstract

Introduction

Conclusions

References

Tables

Figures

◀

▶

◀

▶

Back

Close

Full Screen / Esc

Printer-friendly Version

Interactive Discussion



This is reflected in the standard simplified expression for methane and nitrous oxide forcing, ΔQ_{CH_4} and $\Delta Q_{\text{N}_2\text{O}}$, respectively (see [Ramaswamy et al., 2001](#); [Myhre et al., 1998](#)):

$$\Delta Q_{\text{CH}_4} = \alpha_{\text{CH}_4} (\sqrt{C_{\text{CH}_4}} - \sqrt{C_{\text{CH}_4}^0}) - f(C_{\text{CH}_4}, C_{\text{N}_2\text{O}}^0) - f(C_{\text{CH}_4}^0, C_{\text{N}_2\text{O}}^0) \quad (\text{A38})$$

$$\Delta Q_{\text{N}_2\text{O}} = \alpha_{\text{N}_2\text{O}} (\sqrt{C_{\text{N}_2\text{O}}} - \sqrt{C_{\text{N}_2\text{O}}^0}) - f(C_{\text{CH}_4}^0, C_{\text{N}_2\text{O}}) - f(C_{\text{CH}_4}^0, C_{\text{N}_2\text{O}}^0) \quad (\text{A39})$$

where the overlap is captured by the function

$$f(M, N) = 0.47 \ln \left(1 + 0.6356 \left(\frac{MN}{10^6} \right)^{0.75} + 0.007 \frac{M}{10^3} \left(\frac{MN}{10^6} \right)^{1.52} \right) \quad (\text{A40})$$

with M and N being CH_4 and N_2O concentrations in ppb. For methane, an additional forcing factor is due to methane-induced enhancement of stratospheric water vapor content. This enhancement is assumed to equate a proportional share (default $\beta=15\%$) of “pure” methane radiative forcing, i.e., without subtraction of N_2O absorption band overlaps:

$$\Delta Q_{\text{CH}_4}^{\text{stratoH}_2\text{O}} = \beta \alpha_{\text{CH}_4} (\sqrt{C_{\text{CH}_4}} - \sqrt{C_{\text{CH}_4}^0}) \quad (\text{A41})$$

A.3.3 Tropospheric ozone

From the tropospheric ozone precursor emissions and following the updated parameterizations of OxComp as given in footnote a of Table 4.11 in [Ehhalt et al. \(2001\)](#), the

Title Page

Abstract

Introduction

Conclusions

References

Tables

Figures

◀

▶

◀

▶

Back

Close

Full Screen / Esc

Printer-friendly Version

Interactive Discussion



change in hemispheric tropospheric ozone concentrations (in DU) is parameterized as:

$$\Delta(\text{tropO}_3) = S_{\text{CH}_4}^{\text{O}_3} \Delta \ln(\text{CH}_4) + S_{\text{NO}_x}^{\text{O}_3} E_{\text{NO}_x} + S_{\text{CO}}^{\text{O}_3} E_{\text{CO}} + S_{\text{VOC}}^{\text{O}_3} E_{\text{VOC}} \quad (\text{A42})$$

where $S_x^{\text{O}_3}$ are the respective sensitivity coefficients of tropospheric ozone to methane concentrations and precursor emissions. The radiative forcing is then approximated by a linear abundance to forcing relationship so that $\Delta Q_{\text{tropO}_3} = \alpha_{\text{tropO}_3} \Delta(\text{tropO}_3)$ with α_{tropO_3} being the radiative efficiency factor (default 0.042).

A3.4 Halogenated gases

The global-mean radiative forcing $\Delta Q_{t,i}$ of halogenated gases is simply derived from their atmospheric mixing ratios (Sect. A2.4) and radiative efficiencies q_i (following Ehhalt et al., 2001, Table 4.11).

$$\Delta Q_{t,i} = q_i (M_{t,i} - M_{0,i}) \quad (\text{A43})$$

The land-ocean forcing contrast in each hemisphere for halogenated gases is assumed to follow the one Hansen et al. (2005) estimated for CFC-11. The hemispheric forcing contrast is dependent on the lifetime of the gas. For short-lived gases (<1 yr) the hemispheric forcing contrast is assumed to equal the time-variable hemispheric emission ratio. For longer lived gases (default >8 yrs), the hemispheric forcing contrast is assumed to equal the one from CFC-11 with linear scaling in between these two approaches for gases with a medium lifetime.

A3.5 Stratospheric ozone

The depletion of the stratospheric ozone layer invokes a negative global-mean radiative forcing ΔQ_t . The depletion and hence radiative forcing is assumed to be dependent on

Title Page

Abstract

Introduction

Conclusions

References

Tables

Figures

◀

▶

◀

▶

Back

Close

Full Screen / Esc

Printer-friendly Version

Interactive Discussion



the equivalent effective stratospheric chlorine (EESC) concentrations as follows:

$$\Delta Q_t = \eta_1 (\eta_2 \times \Delta \text{EESC}_t)^{\eta_3} \quad (\text{A44})$$

where η_1 is a sensitivity scaling factor (default $-4.49\text{e-}4 \text{ Wm}^{-2}$), ΔEESC_t the EESC concentrations above 1980 levels (in ppb), the factor η_2 equals $\frac{1}{100} (\text{ppb}^{-1})$ and η_3 is the sensitivity exponent (default 1.7).

EESC concentrations are derived from the modeled concentrations of 16 ozone depleting substances controlled under the Montreal Protocol, their respective chlorine and bromine atoms, fractional release factors and a bromine versus chlorine ozone depletion efficiency (default 45) (Daniel et al., 1999).

A3.6 Tropospheric aerosols

The direct effect of aerosols is approximated by simple linear forcing-abundance relationships for sulfate, nitrate, black carbon and organic carbon. Time-variable abundances of these short-lived aerosols are in turn approximated by their hemispheric emissions. The ratio of direct forcing over land and ocean areas in each hemisphere is taken from Hansen et al. (2005) (available at <http://data.giss.nasa.gov/efficacy/>). By specifying the global-mean direct radiative forcing for one particular year, the time series of forcing is thus derived from a time series of hemispheric emissions and the land-ocean abundance ratio.

The indirect radiative forcing, formerly modeled as dependent on SO_x abundances only (Wigley, 1991a), is now estimated by taking into account time-series of sulfate, nitrate, black carbon and organic carbon optical thickness:

$$\Delta Q_{\text{Alb},i} = r \times P_{\text{Alb},i} \times \log\left(\frac{\sum_g w_g N_{g,i}}{\sum_g w_g N_{g,i}^0}\right) \quad (\text{A45})$$

where $\Delta Q_{\text{Alb},i}$ is the first indirect aerosol forcing in the four atmospheric boxes i , representing land and ocean areas in each hemisphere; P_{Alb} is the four-element

Title Page

Abstract

Introduction

Conclusions

References

Tables

Figures

◀

▶

◀

▶

Back

Close

Full Screen / Esc

Printer-friendly Version

Interactive Discussion



MAGICC 6.0

M. Meinshausen et al.

Title Page

Abstract

Introduction

Conclusions

References

Tables

Figures

◀

▶

◀

▶

Back

Close

Full Screen / Esc

Printer-friendly Version

Interactive Discussion



pattern of aerosol indirect effects related to albedo (Twomey, 1977) in a reference year. The second indirect effect on cloud cover changes (Albrecht, 1989) is modeled equivalently – using a reference year pattern $P_{Cvr,i}$. The respective default patterns are derived from data displayed in Fig. 13 of Hansen et al. (2005). The scaling factor r allows to specify a global-mean first or second indirect forcing for a specific reference year. The time-variable number concentrations of soluble aerosols $N_{g,i}$ above their pre-industrial level in each hemisphere $N_{g,i}^0$ are normed to unity in that reference year for sulfates, nitrates, black carbon and organic carbon, where for black carbon the differential solubility from industrial (fossil fuel) and biomass burning sources is taken into account (default solubility ratio 0.6/0.8) (Hansen et al., 2005). The default contribution shares w_g of the individual aerosol types g to the indirect aerosol effect were assigned to reflect the preliminary results by Hansen et al. (2005), namely 36% for sulfates, 36% for organic carbon, 23% for nitrates and 5% for black carbon. Note though, that these estimates of the importance of non-SO_x aerosol contributions are very uncertain, as well because the solubility for organic carbon and nitrates has large uncertainties. The number concentrations $N_{g,i}$ are here approximated by historical optical thickness estimates (as provided on <http://data.giss.nasa.gov/efficacy/> see as well <http://www.atmos-chem-phys-discuss.net/8/6153/2008/acpd-8-6153-2008-supplement.pdf>) and extrapolated into the future by scaling with hemispheric emissions. The general logarithmic relation between number concentrations and forcing is based on the findings by Gultepe and Isaac (1999) and as well used in Hansen et al. (2005).

A4 From forcing to temperatures: the upwelling-diffusion climate model

In the early stages, MAGICC's climate module evolved from the simple climate model introduced by Hoffert et al. (1980) and modified by Schlesinger (1984). MAGICC's atmosphere has four boxes with zero heat capacity, one over land and one over ocean for each hemisphere. The atmospheric boxes over the ocean are coupled to the mixed layer of the ocean hemispheres, with a set of $n-1$ vertical layers below (see Fig. 14).

[Title Page](#)
[Abstract](#)
[Introduction](#)
[Conclusions](#)
[References](#)
[Tables](#)
[Figures](#)




[Back](#)
[Close](#)
[Full Screen / Esc](#)
[Printer-friendly Version](#)
[Interactive Discussion](#)


The heat exchange between the oceanic layers is driven by vertical diffusion and advection. In the previous model version, the ocean area profile is uniform with depth and the corresponding downwelling is modeled as a stream of polar sinking water from the top mixed layer to the bottom layer. In this study, an updated upwelling-diffusion-entrainment (UDE) ocean model is implemented with a depth-dependent ocean area – using an ocean area profile from HadCM2. For simplicity, the following equations govern the uniform area upwelling-diffusion of the model. Section A5 provides details on the UDE algorithms.

A4.1 Partitioning of feedbacks

Going beyond the globally averaged energy balance equation (see Eq. 1) and in order to improve the comparability between MAGICC and AOGCMs, Jones and Wigley (1995) introduced a differentiation of feedback parameters over land and ocean. This allows an adjustable land to ocean warming ratio in equilibrium comparable to AOGCMs. Given that in equilibrium the oceanic heat uptake is zero, the global energy balance equation can be written as:

$$\Delta Q_G = \lambda_G \Delta T_G = f_L \lambda_L \Delta T_L + f_O \lambda_O \Delta T_O \quad (\text{A46})$$

where $\Delta Q_G, \lambda_G$ and ΔT_G are the global-mean forcing, feedback, and temperature, respectively. The right hand side states the area fractions f , feedbacks λ , and mean temperatures T for ocean (O) and land (L). The non-linear set of equations that determines λ_O and λ_L for a given set of equilibrium land-ocean warming ratio $RLO (=T_L/T_O)$, global-mean feedback λ_G , heat exchange and enhancement factors (k, μ), is solved by an iterative procedure involving the set of linear Eqs. (A47–A50), seeking the solution for λ_L closest to λ_G . The amended procedure takes into account the time-constant radiative forcing pattern by CO_2 for the four boxes with hemispheric land/ocean regions, if prescribed.

Following [Wigley and Schlesinger \(1985\)](#), it is assumed that the atmosphere is in equilibrium with the underlying surface, so that the energy balance equations for the northern hemispheric ocean (NO) is:

$$\begin{aligned}
 f_{\text{NO}}\lambda_O\Delta T_{\text{NO}} &= \text{infrared outgoing flux} \\
 f_{\text{NO}}\Delta Q_{\text{NO}} &= \text{forcing} \\
 +k_{\text{LO}}(\Delta T_{\text{NL}} - \mu\Delta T_{\text{NO}}) &= \text{land-ocean heat ex.} \\
 +k_{\text{NS}}\alpha(\Delta T_{\text{SO}} - \Delta T_{\text{NO}}) &= \text{hemispheric heat ex.}
 \end{aligned}
 \tag{A47}$$

where ΔT_{NO} is the surface temperature change over the northern hemispheric ocean, ΔQ_{NO} the radiative forcing over that region, f_{NO} the northern ocean's area fraction of the earth surface, k_{LO} the land-ocean heat exchange coefficient [$\text{W m}^{-2}\text{C}^{-1}$], a heat transport enhancement factor μ allowing for asymmetric heat exchange between land and ocean ($1 \leq \mu$ – see Sect. [A4.2](#) below), and k_{NS} is the hemispheric heat exchange coefficient over oceans. Correspondingly, the equilibrium energy balance equations for the northern hemispheric land (NL), southern hemispheric ocean (SO) and southern hemispheric land (SL) are:

$$\begin{aligned}
 f_{\text{NL}}\lambda_L\Delta T_{\text{NL}} &= f_{\text{NL}}\Delta Q_{\text{NL}} \\
 &+k_{\text{LO}}(\mu\Delta T_{\text{NO}} - \Delta T_{\text{NL}})
 \end{aligned}
 \tag{A48}$$

$$\begin{aligned}
 f_{\text{SO}}\lambda_O\Delta T_{\text{SO}} &= f_{\text{SO}}\Delta Q_{\text{SO}} \\
 &+k_{\text{LO}}(\Delta T_{\text{SL}} - \mu\Delta T_{\text{SO}}) \\
 &+k_{\text{NS}}\alpha(\Delta T_{\text{NO}} - \Delta T_{\text{SO}})
 \end{aligned}
 \tag{A49}$$

$$\begin{aligned}
 f_{\text{SL}}\lambda_L\Delta T_{\text{SL}} &= f_{\text{SL}}\Delta Q_{\text{SL}} \\
 &+k_{\text{LO}}(\mu\Delta T_{\text{SO}} - \Delta T_{\text{SL}})
 \end{aligned}
 \tag{A50}$$

As detailed below Sect. [A4.3](#), the feedback factors λ in this energy balance equation can be dependent on the total radiative forcing, if the sensitivity factor ξ is set different

Title Page

Abstract

Introduction

Conclusions

References

Tables

Figures

◀

▶

◀

▶

Back

Close

Full Screen / Esc

Printer-friendly Version

Interactive Discussion



from zero (see Eq. A52). As both the forcing-dependent feedback factors and the heat exchange enhancement factors are newly introduced in this MAGICC version, the following two Sects. (A4.2 and A4.2) are intended to provide both the motivation and details of these parameterizations.

5 A4.2 Amended land-ocean heat exchange formulation

This section highlights a “geometric” effect that can be the reason for effective climate sensitivities changing over time, namely that the global-mean sensitivity increases simply due to a shift of temperatures across different regions with regionally different, but constant sensitivities. To control the temperature shifts between ocean and land, a heat transport enhancement factor μ is introduced that allows for asymmetric heat exchange between land and ocean. Enhancing the ocean-to-land heat transport ($\mu \geq 1$) has the benefit that the simple climate model can better simulate some characteristic AOGCM responses. AOGCMs often show a land-ocean-warming ratio (RLO) that decreases over time but stays above unity combined with an increasing effective climate sensitivity (see bottom rows in Fig. 16, 17, and 18). In previous MAGICC versions, the higher land than ocean warming (RLO > 1) has been achieved by a smaller feedback (greater climate sensitivity) over land compared to the ocean boxes. However, as the RLO decreased over time (due to less and less ocean heat uptake towards equilibrium), so did the effective global-mean climate sensitivity in previous model versions. The way chosen here to allow both a RLO above unity and a non-decreasing effective climate sensitivity is to assume an asymmetric heat exchange between land and oceans. In fact, there is no reason other than simplicity that the land-to-ocean and ocean-to-land heat exchange fluxes should be equally proportional to temperature perturbations above land and ocean. For example, an enhanced hydrological cycle, namely an increased latent heat transport from oceans to land could be approximated by such an asymmetric heat exchange formulation. Thus, this version allows that ocean temperature perturbations are influencing the heat exchange more than the land perturbations,

Title Page

Abstract

Introduction

Conclusions

References

Tables

Figures

◀

▶

◀

▶

Back

Close

Full Screen / Esc

Printer-friendly Version

Interactive Discussion



so that the land-ocean heat exchange term can be written as:

$$HX_{LO} = k_{LO}(\Delta T_L - \mu \Delta T_O) \quad (A51)$$

where HX_{LO} is the land-ocean heat exchange (positive in direction land to ocean), μ is the ocean-to-land enhancement factor and ΔT_L and ΔT_O are the temperature perturbations for the land and ocean region, respectively (cf. Eq. A47 ff.).

A4.3 Accounting for climate-state dependent feedbacks

Some AOGCMs runs indicate higher effective climate sensitivities for higher forcings and/or temperatures. For example, the ECHAM5/MPI-OM model shows an effective climate sensitivity of approximately 3.5°C after a stabilization at twice pre-industrial CO₂ concentrations and 4°C for a stabilization at quadrupled pre-industrial CO₂ concentrations (see Fig. 1b – see as well Raper et al., 2001; Hansen et al., 2005). Given that the transient land-ocean warming ratio (RLO) is the same for the 1pctto2x and 1pctto4x runs (see Fig. 16 last row), the “geometric” effect discussed in the previous Sect. A4.2 does not allow to emulate this increase in climate sensitivity. Hence, an alternative explanation could be climate-state dependent, non-constant feedbacks within AOGCMs. In other words, the assumption in the standard energy balance Eq. (1) might be too simplistic that climate feedbacks (λ) are time-constant and that the energy outflux (λT) thus scales proportionally with temperature. For example, the slow feedback due to retreating ice-sheets can lead to changes over diagnosed effective sensitivities in AOGCMs (see e.g. Raper et al., 2001) over long time-scales. Hansen et al. (2005) shows that the 100-year climate response in the GISS model is more sensitive to higher forcings than to lower or negative forcings. Hansen et al. (2005) express this effect by increasing efficacies for increasing radiative forcing. Table 1 in Hansen et al. (2005) suggests a gradient of roughly 1% increase in efficacy per each additional Wm⁻² (OLS-regression of E_a versus F_a across the full range of CO₂ experiments), although some intervals (e.g. from 1.25 to 1.5×CO₂) can show a slightly higher sensitivity, i.e., 3% per Wm⁻².

Title Page

Abstract

Introduction

Conclusions

References

Tables

Figures

◀

▶

◀

▶

Back

Close

Full Screen / Esc

Printer-friendly Version

Interactive Discussion



Title Page

Abstract

Introduction

Conclusions

References

Tables

Figures

◀

▶

◀

▶

Back

Close

Full Screen / Esc

Printer-friendly Version

Interactive Discussion



The findings by Hansen et al. (2005) might suggest that efficacies (simply expressed as a scaling factor on the actual forcing in the simple climate model) could be adapted for different forcing strengths. Alternatively, the climate sensitivity can be made dependent on the forcing level. This distinction, on whether to modify forcing or sensitivity, is not important at or close to the equilibrium of the climate. However, the transient climate response after a forcing change will be slightly faster, if the efficacies of the forcing, instead of the feedback parameters were adjusted. In this MAGICC version, if a forcing dependency of the sensitivity is assumed, the land and ocean feedback parameters λ_L and λ_O are scaled as

$$\lambda = \frac{\Delta Q_{2x}}{\frac{\Delta Q_{2x}}{\lambda_{2x}} + \xi(\Delta Q - \Delta Q_{2x})} \quad (\text{A52})$$

where λ_{2x} is the feedback parameter ($= \frac{\Delta Q_{2x}}{\Delta T_{2x}}$) at the forcing level for twice pre-industrial CO_2 concentrations. The sensitivity factor ξ ($\text{KW}^{-1} \text{m}^2$) does scale the climate sensitivity in proportion to the difference of forcing away from the model-specific ‘twice pre-industrial CO_2 forcing level’ ($\Delta Q - \Delta Q_{2x}$). The 1% increase in efficacy for each additional unit forcing in Hansen’s findings translates into a feedback sensitivity factor ϵ of $0.03 \text{KW}^{-1} \text{m}^2$ (assuming a climate sensitivity ΔT_{2x} of 3°C). Note that this scaling convention (Eq. A52) ensures that climate sensitivities are comparable on the basis of equilibrium warming that corresponds to twice preindustrial CO_2 concentration levels. (see Table 4).

A4.4 Efficacies

Efficacy is defined as the ratio of global-mean temperature response for a particular radiative forcing over the global-mean temperature response for the same amount of global-mean radiative forcing induced by CO_2 (see Sect. 2.8.5 in Forster et al., 2007). In most cases, the predominant reason why efficacies are different between different

forcing agents are both their geographical and vertical distribution of the forcing (Boer and Yu, 2003; Joshi et al., 2003; Hansen et al., 2005). This version of MAGICC introduces the option to apply different efficacy terms for the different forcings agents. The effective radiative forcing (Q_e) is thus used in the energy balance equations (see Eq. 1), which is the product of the standard forcing – after thermal adjustment of the stratosphere – (Q_a) and the corresponding efficacy term (E_a). Note that this parameterization yields slightly faster transient climate responses compared to an approach where different climate sensitivities were applied for each individual forcing agent (cf. Sect. A4.3 above).

If the hemispheric land/ocean patterns of forcings are applied in MAGICC, the combination with different land ocean feedback factors does result in MAGICC 6.0 exhibiting efficacies different from unity for non- CO_2 forcing agents. MAGICC calculates these internal efficacies using reference year (default 2005) forcing patterns. After norming these forcing patterns to a global-mean of ΔQ_{2x} (default 3.71 Wm^{-2}), the internal efficacy can be determined as

$$E_{\text{int}} = \frac{T_{\text{eff}2x}}{\Delta T_{2x}}, \quad (\text{A53})$$

where $T_{\text{eff}2x}$ is the actual global-mean equilibrium temperature resulting from the applied and normed forcing pattern and ΔT_{2x} is the corresponding warming for the CO_2 forcing, the climate sensitivity. For most forcing agents, these internal efficacies are very close to one, except for forcings with a strong land/ocean forcing contrast, such as direct aerosol forcings, with a value of 1.14 for the example case of HadCM3 emulation (calibration IIIa – see Table B3) settings. By default, these internal efficacies are taken into account when applying prescribed efficacies, so that:

$$Q_e = \frac{E_a}{E_{\text{int}}} Q_a \quad (\text{A54})$$

Title Page

Abstract

Introduction

Conclusions

References

Tables

Figures

◀

▶

◀

▶

Back

Close

Full Screen / Esc

Printer-friendly Version

Interactive Discussion



A4.5 The upwelling diffusion equations

The transient temperature evolution is largely influenced by the climate system's inertia, in turn dependent on the nature of the heat uptake by the climate system. The transient energy balance equations can be written as:

$$\begin{aligned}
 5 \quad & f_{\text{NO}}(\zeta_o \frac{d\Delta T_{\text{NO},1}}{dt} - \Delta Q_{\text{NO}} + \lambda_o \alpha \Delta T_{\text{NO},1} + F_N) = \dots \\
 & \dots k_{\text{LO}}(\Delta T_{\text{NL}} - \mu \alpha \Delta T_{\text{NO},1}) + k_{\text{NS}} \alpha (\Delta T_{\text{SO},1} - \Delta T_{\text{NO},1}) \quad (\text{A55})
 \end{aligned}$$

$$\begin{aligned}
 & f_{\text{NL}}(\zeta_L \frac{d\Delta T_{\text{NL}}}{dt} - \Delta Q_{\text{NL}} + \lambda_L \Delta T_{\text{NL}}) = \dots \\
 & \dots k_{\text{LO}}(\mu \alpha \Delta T_{\text{NO},1} - \Delta T_{\text{NL}}) \quad (\text{A56})
 \end{aligned}$$

$$\begin{aligned}
 10 \quad & f_{\text{SO}}(\zeta_o \frac{d\Delta T_{\text{SO},1}}{dt} - \Delta Q_{\text{SO}} + \lambda_o \alpha \Delta T_{\text{SO},1} + F_S) = \dots \\
 & \dots k_{\text{LO}}(\Delta T_{\text{SL}} - \mu \alpha \Delta T_{\text{SO},1}) + k_{\text{NS}} \alpha (\Delta T_{\text{NO},1} - \Delta T_{\text{SO},1}) \quad (\text{A57})
 \end{aligned}$$

$$\begin{aligned}
 & f_{\text{SL}}(\zeta_L \frac{d\Delta T_{\text{SL}}}{dt} - \Delta Q_{\text{SL}} + \lambda_L \Delta T_{\text{SL}}) = \dots \\
 & \dots k_{\text{LO}}(\mu \alpha \Delta T_{\text{SO},1} - \Delta T_{\text{SL}}) \quad (\text{A58})
 \end{aligned}$$

where the adjustment factor α (default 1.2) determines the ratio of changes in air (ΔT_{XO}) to mixed layer temperatures ($\Delta T_{\text{XO},1}$) over ocean areas. Based on ECHAM1/LSG analysis (Raper and Cubasch, 1996), this sea-ice factor was first introduced by Raper et al. (2001) to account for the fact that the air temperature will exhibit additional warming, as the atmosphere feels warmer ocean surface temperatures where sea ice retreats. The bulk heat capacity of the mixed layer in each hemisphere x is $f_x \zeta_o = f_x \rho c h_m$, where ρ denotes the density of seawater ($1.026 \times 10^6 \text{ g m}^{-3}$), c is the specific heat capacity ($0.9333 \text{ cal g}^{-1} \text{ }^\circ\text{C}^{-1} = 4.1856 \times 0.9333 \text{ Joule g}^{-1} \text{ }^\circ\text{C}^{-1}$) and h_m is the mixed layer's thickness [m]. The bulk heat capacity of the land areas is $f_x \zeta_L$, here

Title Page

Abstract

Introduction

Conclusions

References

Tables

Figures

◀

▶

◀

▶

Back

Close

Full Screen / Esc

Printer-friendly Version

Interactive Discussion



assumed to be zero. The net heat flux into the ocean below the mixed layer is denoted with F_x .

Equation (A56) can then be written as:

$$\Delta T_{NL} = \frac{f_{NL}\Delta Q_{NL} + k_{LO}\mu\alpha\Delta T_{NO,1}}{f_{NL}\lambda_L + k_{LO}} \quad (\text{A59})$$

5 Substituting T_{NL} in Eq. (A55) yields:

$$f_{NO}(\zeta_o \frac{d\Delta T_{NO,1}}{dt} - \Delta Q_{NO} + \lambda_o\alpha\Delta T_{NO,1} + F_N) = \frac{k_{LO}}{\frac{k_{LO}}{f_{NL}} + \lambda_L} (\Delta Q_{NL} - \lambda_L\mu\alpha\Delta T_{NO,1}) + k_{NS}\alpha(\Delta T_{SO,1} - \Delta T_{NO,1}) \quad (\text{A60})$$

10 Provided we knew the heat flux F_N into the ocean below the mixed layer, we could now derive $d\Delta T_{NO,1}/dt$. This net heat flux F_N at the bottom of the mixed layer is determined by vertical heat diffusivity (diffusion coefficient K_z [$\text{cm}^2 \text{s}^{-1} = 3155.76^{-1} \text{m}^2 \text{yr}^{-1}$]), upwelling and downwelling (upwelling velocity w [m yr^{-1}]), both acting on the perturbations ΔT from the initial temperature profile $T_{NO,z}^0$. If the upwelling w varies over time, the change in upwelling velocity $\Delta w^t = (w^t - w^0)$ compared to its initial state w^0 is assumed to act on the initial temperature profile, so that:

$$F_N = \frac{K_z}{0.5h_d}\rho c(\Delta T_{NO,1} - \Delta T_{NO,2}) - w\rho c(\Delta T_{NO,2} - \beta\Delta T_{NO,1}) - \Delta w\rho c(T_{NO,2}^0 - T_{NO,sink}^0) \quad (\text{A61})$$

20 where $T_{NO,z}^0$ is the initial temperature for layer z or initial temperature of the downwelling water (z ="sink").

Title Page

Abstract

Introduction

Conclusions

References

Tables

Figures

◀

▶

◀

▶

Back

Close

Full Screen / Esc

Printer-friendly Version

Interactive Discussion



Given that the top layer is assumed to be mixed, the gradient of the temperature perturbations is calculated by the difference of the perturbations divided by half the thickness h_d of the second layer (see Fig. 15). Substituting F_N in Eq. (A60) with Eq. (A61) and transforming the equation to discrete time steps, yields:

$$\begin{aligned}
 5 \quad \frac{d\Delta T_{\text{NO},1}}{dt} &\approx \frac{\Delta T_{\text{NO},1}^{t+1} - \Delta T_{\text{NO},1}^t}{\Delta t} = \\
 &\quad \frac{1}{\zeta_o} \Delta Q_{\text{NO}}^t \quad \text{:forcing} \\
 &\quad - \frac{\lambda_o \alpha}{\zeta_o} \Delta T_{\text{NO},1}^{t+1} \quad \text{:feedback} \\
 &\quad - \frac{K_z}{0.5h_d h_m} (\Delta T_{\text{NO},1}^{t+1} - \Delta T_{\text{NO},2}^{t+1}) \quad \text{:diffusion} \\
 &\quad + \frac{w^t}{h_m} (\Delta T_{\text{NO},2}^{t+1} - \beta \Delta T_{\text{NO},1}^{t+1}) \quad \text{:upwelling} \\
 10 \quad &\quad + \frac{\Delta w^t}{h_m} (T_{\text{NO},2}^0 - T_{\text{NO},\text{sink}}^0) \quad \text{:variable upwelling} \\
 &\quad + \frac{k_{\text{LO}} (\Delta Q_{\text{NL}}^t - \lambda_L \mu \alpha \Delta T_{\text{NO},1}^{t+1})}{\zeta_o f_{\text{NO}} (\frac{k_{\text{LO}}}{f_{\text{NL}}} + \lambda_L)} \quad \text{:land forcing} \\
 &\quad + \frac{k_{\text{NS}} \alpha}{\zeta_o f_{\text{NO}}} (\Delta T_{\text{SO},1}^t - \Delta T_{\text{NO},1}^t) \quad \text{:inter-hemispheric ex.} \quad (\text{A62})
 \end{aligned}$$

For the layers below the mixed layer ($2 \leq z \leq n-1$), the temperature updating is governed solely by diffusion (first two terms in following Eq. A63) and upwelling (last two terms), so that:

$$15 \quad \frac{\Delta T_{\text{NO},z}^{t+1} - \Delta T_{\text{NO},z}^t}{\Delta t} =$$

6222

Title Page

Abstract

Introduction

Conclusions

References

Tables

Figures

◀

▶

◀

▶

Back

Close

Full Screen / Esc

Printer-friendly Version

Interactive Discussion



$$\begin{aligned}
& \frac{K_z}{0.5(h_d + h'_d)h_d} (\Delta T_{\text{NO},z-1}^{t+1} - \Delta T_{\text{NO},z}^{t+1}) \\
& - \frac{K_z}{h_d^2} (\Delta T_{\text{NO},z}^{t+1} - \Delta T_{\text{NO},z+1}^{t+1}) \\
& + \frac{w^t}{h_d} (\Delta T_{\text{NO},z+1}^{t+1} - \Delta T_{\text{NO},z}^{t+1}) \\
& + \frac{\Delta w^t}{h_d} (T_{\text{NO},z+1}^0 - T_{\text{NO},z}^0)
\end{aligned} \tag{A63}$$

5 where h'_d is zero for the layer below the mixed layer ($z=2$) and h_d otherwise, Δw^t is the change from the initial upwelling rate.

For the bottom layer ($z=n$), the downwelling term has to be taken into account, so that:

$$\begin{aligned}
\frac{\Delta T_{\text{NO},n}^{t+1} - \Delta T_{\text{NO},n}^t}{\Delta t} &= \frac{K_z}{h_d^2} (\Delta T_{\text{NO},n-1}^{t+1} - \Delta T_{\text{NO},n}^{t+1}) \\
& + \frac{w^t}{h_d} (\beta \Delta T_{\text{NO},1}^t - \Delta T_{\text{NO},n}^{t+1}) \\
& + \frac{\Delta w^t}{h_d} (T_{\text{NO},\text{sink}}^0 - T_{\text{NO},n}^0)
\end{aligned} \tag{A64}$$

15 Corresponding to the temperature calculations shown here for the Northern Hemisphere ocean (NO), the equivalent steps apply for the Southern Hemisphere ocean (SO). For simplicity, these equations described the constant-depth area profile case, which is calculated by MAGICC, if the depth-dependency factor ϑ is set to zero. The detailed code for the general case with $0 \leq \vartheta \leq 1$ is given in Sect. A5.

Title Page

Abstract

Introduction

Conclusions

References

Tables

Figures

◀

▶

◀

▶

Back

Close

Full Screen / Esc

Printer-friendly Version

Interactive Discussion



A4.6 Calculating heat uptake

Heat uptake by the climate system can be calculated in different ways. For example, by using the global energy balance (Eq. 1). Using the effective sensitivity as in Eq. (A46) the heat uptake F^t is estimated as:

$$5 \quad \frac{dH^t}{dt} = F^t = Q^t - (f_L \lambda_L T_L^t + f_O \lambda_O T_O^t) \quad (\text{A65})$$

As verification, MAGICC 6.0 does as well integrate the heat content change of each layer in the ocean – yielding identical results, given the assumed zero heat capacity of the atmosphere and land areas:

$$\Delta H^t = \sum_{i=1}^n \frac{1}{\rho c h_i} \frac{(f_{\text{NO}} \Delta T_{\text{NO},i}^t + f_{\text{SO}} \Delta T_{\text{SO},i}^t)}{f_O} + \epsilon \quad (\text{A66})$$

10 where h_i is the thickness of the layer, i.e., h_m for the mixed layer and h_o for the others and ϵ is a small term to account for the heat content of the polar sinking water.

A4.7 Depth-dependent ocean with entrainment

[Harvey and Schneider \(1985a,b\)](#) introduced the upwelling-diffusion model with entrainment from the polar sinking water by varying the upwelling velocity w with depth. Building on the work by [Raper et al. \(2001\)](#), MAGICC 6.0 also includes the option of a depth-dependent ocean area profile. If the depth-dependency parameter ϑ is set to 1 (default), a standard depth-dependent ocean area profile is assumed as in HadCM2 and used in [Raper et al. \(2001\)](#). A constant upwelling velocity is assumed and maintained by entrainment from the downwelling pipe. As in the model by [Harvey and Schneider \(1985b\)](#), the upwelling stream mass flux decreases with depth. Thus, the amount of entrainment into layer z is proportional to the decrease in area from the top to the bottom of each layer (cf. Fig. 15). We differ from the model structures tested by [Raper et al. \(2001\)](#), by equating the temperature of the entraining water to that of

Title Page

Abstract

Introduction

Conclusions

References

Tables

Figures

◀

▶

◀

▶

Back

Close

Full Screen / Esc

Printer-friendly Version

Interactive Discussion



the downwelling pipe, namely a fraction β (default 0.2) of the mixed layer temperature $\Delta T_{H,1}^{t-1}$ of the previous timestep in Hemisphere H. For a detailed description of the code, see the following Sect. A5.

Simple upwelling-diffusion models can overestimate the ocean heat uptake for higher warming scenarios when applying parameter sets that allowed to match heat uptake for lower warming scenarios (see e.g. Fig. 17b in Harvey et al., 1997). Thus, MAGICC 6.0 includes a warming-dependent vertical diffusivity gradient. A strengthened thermal stratification and hence reduced vertical mixing might be contributing to the decreased heat uptake for higher warming levels. Thus, the effective vertical diffusivity at $K_{z,L}$ between ocean layer L and L+1 is given by:

$$K_{z,L} = \max(K_{z,\min}, (1 - d_L) \frac{dK_{ztop}}{dT} (\Delta T_{H,1}^{t-1} - \Delta T_{H,n}^{t-1}) + K_z) \quad (A67)$$

where $K_{z,\min}$ is the minimal vertical diffusivity (default $0.1 \text{ cm}^2 \text{ s}^{-1}$); d_L is the relative depth of the layer boundary with zero at the bottom of the mixed layer and one for the top of the bottom layer; $\frac{dK_{ztop}}{dT}$ is the newly introduced sensitivity coefficient specifying how the vertical diffusivity K_{ztop} between the mixed layer n and layer 2 is changing with a change in the temperature difference between the top and the bottom layer of the respective hemisphere at the previous timestep t-1 ($\Delta T_{H,1}^{t-1} - \Delta T_{H,n}^{t-1}$).

A5 Implementation of upwelling-diffusion-entrainment equations

This section details how the equations governing the upwelling-diffusive-entrainment (UDE) ocean (Eqs. A62, A63, A64) are implemented and amended by entrainment terms and depth-dependent ocean area (see Fig. 15). Thus, the following equations represent the core of the UDE model and build on the initial work by Harvey and Schneider (1985b,a); Hoffert et al. (1980).

The entrainment is here modeled so that the upwelling velocity in the main column is the same in each layer. Thus, the three area correction factors applied below are:

Title Page

Abstract

Introduction

Conclusions

References

Tables

Figures

◀

▶

◀

▶

Back

Close

Full Screen / Esc

Printer-friendly Version

Interactive Discussion



$$\theta_z^{\text{top}} = \frac{A_z}{(A_{z+1} + A_z)/2}$$

$$\theta_z^b = \frac{A_{z+1}}{(A_{z+1} + A_z)/2}$$

$$\theta_z^{\text{dif}} = \frac{A_{z+1} - A_z}{(A_{z+1} + A_z)/2}$$

(A68)

5 where A_z is the area at the top of layer z or bottom of layer $z-1$ and the denominator is thus an approximation for the mean area of each ocean layer.

For the mixed layer, all terms in Eq. (A62) involving $\Delta T_{\text{NO},1}^{t+1}$ are collected on the left hand side in variable $A(1)$. All terms involving $\Delta T_{\text{NO},2}^{t+1}$ are collected in variable $B(1)$ on the left hand side. All other terms are held in variable $D(1)$ on the right hand side, so
 10 that the equation reads:

$$\Delta T_{\text{NO},1}^{t+1} = -\frac{B(1)}{A(1)} \Delta T_{\text{NO},2}^{t+1} + \frac{D(1)}{A(1)} \quad (\text{A69})$$

with

$$A(1) = 1.0 + \theta_1^{\text{top}} \Delta t \frac{\lambda_o \alpha}{\zeta_o} \quad \text{:feedback over ocean}$$

$$+ \theta_1^b \Delta t \frac{K_z}{0.5 h_m h_d} \quad \text{:diffusion to layer 2}$$

$$+ \theta_1^b \Delta t \frac{w^t \beta}{h_m} \quad \text{:downwelling}$$

$$+ \theta_1^{\text{top}} \Delta t \frac{k_{\text{LO}} \lambda_L \mu \alpha}{\zeta_o f_{\text{NO}} \left(\frac{k_{\text{LO}}}{f_{\text{NL}}} + \lambda_L \right)} \quad \text{:feedback over land} \quad (\text{A70})$$

6226

Title Page

Abstract

Introduction

Conclusions

References

Tables

Figures

◀

▶

◀

▶

Back

Close

Full Screen / Esc

Printer-friendly Version

Interactive Discussion



$$B(1) = -\theta_1^b \Delta t \frac{K_z}{0.5h_m h_d} \text{ :diffusion from layer 2}$$

$$-\theta_1^b \Delta t \frac{w^t}{h_m} \text{ :upwelling from layer 2}$$
(A71)

$$D(1) = \Delta T_{NO,1}^t \text{ :previous temp}$$

$$+\theta_1^{\text{top}} \Delta t \frac{1}{\zeta_o} Q_{NO} \text{ :forcing ocean}$$

$$+\theta_1^{\text{top}} \Delta t \frac{\alpha k_{NS}}{\zeta_o f_{NO}} (\Delta T_{SO,1}^t - \Delta T_{NO,1}^t) \text{ :inter-hemispheric ex.}$$

$$+\theta_1^{\text{top}} \Delta t \frac{k_{LO} \Delta Q_{NL}}{\zeta_o f_{NO} (\frac{k_{LO}}{f_{NL}} + \lambda_L)} \text{ :land forcing}$$

$$+\theta_1^b \Delta t \frac{\Delta w^t}{h_m} (T_{NO,2}^0 - T_{NO,sink}^0) \text{ :variable upwelling}$$
(A72)

For the medium layers ($2 \leq z \leq n$), the terms are re-ordered, so that A(z) comprises the terms for $\Delta T_{NO,z-1}^{t+1}$, B(z) the terms for $\Delta T_{NO,z}^{t+1}$, C(z) the terms for $\Delta T_{NO,z+1}^{t+1}$ and D(z) the remaining terms, according to:

$$\Delta T_{NO,z-1}^{t+1} = -\frac{B(z)}{A(z)} \Delta T_{NO,z}^{t+1} - \frac{C(z)}{A(z)} \Delta T_{NO,z+1}^{t+1} + \frac{D(z)}{A(z)}$$
(A73)

with

$$A(z) = -\theta_z^{\text{top}} \Delta t \frac{K_z}{0.5(h_d + h'_d)h_d} \text{ :diffusion from layer above}$$
(A74)

[Title Page](#)
[Abstract](#)
[Introduction](#)
[Conclusions](#)
[References](#)
[Tables](#)
[Figures](#)
[◀](#)
[▶](#)
[◀](#)
[▶](#)
[Back](#)
[Close](#)
[Full Screen / Esc](#)
[Printer-friendly Version](#)
[Interactive Discussion](#)


$$\begin{aligned}
 B(z) &= 1.0 + \theta_z^b \Delta t \frac{K_z}{h_d^2} && \text{:diffusion to layer below} \\
 &+ \theta_z^{top} \Delta t \frac{K_z}{0.5(h_d + h'_d)h_d} && \text{:diffusion to layer above} \\
 &+ \theta_z^{top} \Delta t \frac{w^t}{h_d} && \text{:upwelling to layer above}
 \end{aligned} \tag{A75}$$

$$\begin{aligned}
 C(z) &= -\theta_z^b \Delta t \frac{K_z}{h_d^2} && \text{:diffusion from layer below} \\
 &-\theta_z^b \Delta t \frac{w^t}{h_d} && \text{:upwelling from layer below}
 \end{aligned} \tag{A76}$$

$$\begin{aligned}
 D(z) &= \Delta T_{NO,z}^t && \text{:previous temp} \\
 &+ \Delta t \frac{\Delta w^t}{h_d} (\theta_z^b T_{NO,z+1}^0 - \theta_z^{top} T_{NO,z}^0) && \text{:variable upwelling} \\
 &+ \theta_z^{dif} \Delta t \frac{w^t}{h_d} \beta \Delta T_{NO,1}^{t-1} && \text{:entrainment} \\
 &+ \theta_z^{dif} \Delta t \frac{\Delta w^t}{h_d} T_{NO,sink}^0 && \text{:variable entrainment}
 \end{aligned} \tag{A77}$$

where h'_d is zero for the layer below the mixed layer and h_d otherwise. For the bottom layer, the respective sum factor $A(n)$ for $\Delta T_{NO,n-1}^{t+1}$, $B(n)$ for $\Delta T_{NO,n}^{t+1}$ and $D(n)$ for the remaining terms are:

[Title Page](#)
[Abstract](#)
[Introduction](#)
[Conclusions](#)
[References](#)
[Tables](#)
[Figures](#)
[◀](#)
[▶](#)
[◀](#)
[▶](#)
[Back](#)
[Close](#)
[Full Screen / Esc](#)
[Printer-friendly Version](#)
[Interactive Discussion](#)


$$\Delta T_{\text{NO},n-1}^{t+1} = -\frac{B(n)}{A(n)} \Delta T_{\text{NO},n}^{t+1} + \frac{D(n)}{A(n)} \quad (\text{A78})$$

with

$$A(n) = -\theta_n^{\text{top}} \Delta t \frac{K_z}{h_d^2} \quad \text{:diffusion from layer n-1} \quad (\text{A79})$$

5

$$B(n) = 1.0 + \theta_n^{\text{top}} \Delta t \frac{K_z}{h_d^2} \quad \text{:diffusion to layer n-1}$$

$$+ \theta_n^{\text{top}} \Delta t \frac{W^t}{h_d} \quad \text{:upwelling to layer n-1} \quad (\text{A80})$$

10

$$D(n) = \Delta T_{\text{NO},n}^t \quad \text{:previous temp}$$

$$+ \theta_n^{\text{top}} \Delta t \frac{W^t}{h_d} \beta \Delta T_{\text{NO},1}^{t-1} \quad \text{:downwelling from top layer}$$

$$- \theta_n^{\text{top}} \Delta t \frac{\Delta W^t}{h_d} T_{\text{NO},n}^0 \quad \text{:variable upwelling}$$

$$+ \theta_n^{\text{top}} \Delta t \frac{\Delta W^t}{h_d} T_{\text{NO},\text{sink}}^0 \quad \text{:variable downwelling} \quad (\text{A81})$$

15

With those Eqs. (A69–A81), the ocean temperatures can be solved consecutively from the bottom to the top layer at each time step.

Title Page

Abstract

Introduction

Conclusions

References

Tables

Figures

◀

▶

◀

▶

Back

Close

Full Screen / Esc

Printer-friendly Version

Interactive Discussion



Appendix B

Calibration result details

This Appendix provides additional details on the calibration procedures and results. The provided results are the individual parameter settings for each CMIP3 AOGCM for the three calibration procedures (see Table 1, and Tables B1, B2 and B3) as well as graphical comparisons between the original CMIP3 AOGCM data and their “calibration IIIa” emulations (see Figs. 16,17 and 18). Furthermore, detailed results are provided for the calibrations to CMIP4 carbon cycle models, the optimized MAGICC parameters, and goodness-of-fit statistics (see Table B4). Graphical comparisons are given for the calibrated carbon pools and fluxes of C4MIP models and their emulations (see Fig. 19).

By calibrating a simple model to more than a single dataserie, some arbitrariness arises in relation to how the overall goodness of fit is composed. In particular, fitting dataserie with different units, like temperature (K) and ocean heat uptake (W/m^2) requires some sort of normalization to avoid that some dataserie are dominating the calibration result simply because they are measured in larger units. The normalization could be done by weighing the dataserie by the (the inverse of) their cross-variance matrix, either using observational, control run or de-drifted model output segments. As this study is attempting to obtain a single set of calibrated parameters for each AOGCM or carbon cycle model rather than (joint) probability distributions for the parameters, a more pragmatic method was chosen, though. Weights for the root mean square errors to the available time series are chosen after a series of calibration iterations so that each time-series’ contribution to the overall goodness of fit is of similar magnitude, thereby avoiding that one single time series dominates the calibration result. It should be noted however that this approach contains some arbitrariness, although the calibration results were tested as not being sensitive to the chosen weights. Specifically, for the calibrations to AOGCM, the chosen weights are 10 (heat-uptake series, W/m^2): 1 (temperature dataserie, K). For calibrating to the C4MIP carbon cycle models, the cho-

Title Page

Abstract

Introduction

Conclusions

References

Tables

Figures

◀

▶

◀

▶

Back

Close

Full Screen / Esc

Printer-friendly Version

Interactive Discussion



sen weights are as follows: 1 (global-mean surface temperature, K) : 25 (net air-to-land flux, GtC/yr): 100 (net air-to-ocean flux, GtC/yr): 50 (atm. CO₂ concentrations, ppm): 25 (NPP and heterotrophic respiration fluxes, GtC/yr): 1 (plant carbon pool, GtC): 0.5 (dead, detritus and soil, carbon pools, GtC). Furthermore, all time series of AOGCMs and carbon cycle models that were used for calibration were lowpass-filtered in order to reduce the noise introduced by natural variability (or the modelled part thereof), as only the mean signal, not the variability, is simulated by MAGICC. The lowpass-filtering employed a pass band boundary of 1/20 cycle/yr and roughness constraint (Mann, 2004).

Acknowledgements. Foremost, we would like to thank the numerous collaborations in preparation of IPCC AR4 and beyond, without which this study would not have been possible. Namely, we would like to thank J. Gregory, K. Taylor, P. Gleckler, B. SanTERS, J. Meehl, J. Arblaster, R. Lieberman, F. Joos and R. Knutti. F. Joos is especially thanked for providing ocean carbon cycle parameterisations as described in Joos et al. (1996, 2001). R. Knutti is as well deeply thanked for discussions and comments on an earlier manuscript, as well as J. Lowe, T. Schneider von Deimling, R. Schofield, V. Brovkin, B. Hare, and E. Kriegler. For providing various emission and concentration datasets on halocarbons, we thank J. Daniel and G. Velders. Furthermore, all those that were helping in various ways to developing MAGICC over the past 20 years clearly deserve acknowledgement, namely M. Salmon, M. Schlesinger, M. Hulme, T. Osborn, S. McGinnis and many more – including those that helped by being sharp critics at times. Remaining errors are of course the sole property of the authors.

We acknowledge the modeling groups for providing their data for analysis, the Program for Climate Model Diagnosis and Intercomparison (PCMDI) for collecting and archiving the model output of the third coupled model intercomparison (CMIP3), and the JSC/CLIVAR Working Group on Coupled Modelling (WGCM) for organizing the model data analysis activity. The multi-model data archive is supported by the Office of Science, U.S. Department of Energy.

References

Albrecht, B.: Aerosols, cloud microphysics, and fractional cloudiness, *Science*, 245, 1227–1230, 1989. [6213](#)

Title Page

Abstract

Introduction

Conclusions

References

Tables

Figures

◀

▶

◀

▶

Back

Close

Full Screen / Esc

Printer-friendly Version

Interactive Discussion



- Allen, M.: Do-it-yourself climate prediction, *Nature*, 401, 642–642, 1999. [6155](#)
- Andrews, T. and Forster, P. M.: CO₂ forcing induces semi-direct effects with consequences for climate feedback interpretations, *Geophys. Res. Lett.*, 35, L04802, 2008. [6162](#)
- Ammann, C. M., Joos, F., Schimel, D. S., Otto-Bliesner, B. L., and Tomas, R. A.: Solar influence on climate during the past millennium: Results from transient simulations with the NCAR Climate System Model, *PNAS*, 104, 3713–3718, 2007. [6186](#)
- Boer, G. J. and Yu, B.: Climate sensitivity and response, *Clim. Dynam.*, 20, 415–429, 2003. [6219](#)
- Brohan, P., Kennedy, J., Harris, I., Tett, S. F. B., and Jones, P. D.: Uncertainty estimates in regional and global observed temperature changes: A new data set from 1850, *J. Geophys. Res.-Atmos.*, 111, D12106, doi:10.1029/2005JD006548, 2006. [6263](#)
- Bryan, K., Manabe, S., and Pacanowski, R. C.: Global Ocean-Atmosphere Climate Model.2. Oceanic Circulation, *J. Phys. Oceanogr.*, 5, 30–46, 1975. [6155](#)
- Collins, W. D., Ramaswamy, V., Schwarzkopf, M. D., Sun, Y., Portmann, R. W., Fu, Q., Casanova, S. E. B., Dufresne, J. L., Fillmore, D. W., Forster, P. M. D., Galin, V. Y., Gohar, L. K., Ingram, W. J., Kratz, D. P., Lefebvre, M. P., Li, J., Marquet, P., Oinas, V., Tsushima, Y., Uchiyama, T., and Zhong, W. Y.: Radiative forcing by well-mixed greenhouse gases: Estimates from climate models in the Intergovernmental Panel on Climate Change (IPCC) Fourth Assessment Report (AR4), *J. Geophys. Res.-Atmos.*, 111, D14317, 10.1029/2005JD006713, 2006. [6157](#), [6172](#)
- Cubasch, U., Meehl, G. A., Boer, G. J., Stouffer, R. J., Dix, M., Noda, A., Senior, C. A., Raper, S., and Yap, K.: Projections of Future Climate Change, in: *Climate Change 2001: The Scientific Basis*, edited by Houghton, J., Ding, Y., Griggs, D., Noguer, M., van der Linden, P., Dai, X., Maskell, K., and Johnson, C., Cambridge University Press, Cambridge, UK, 892 pp., 2001. [6156](#)
- Daniel, J. S., Solomon, S., Portmann, R. W., and Garcia, R. R.: Stratospheric ozone destruction: The importance of bromine relative to chlorine, *J. Geophys. Res.-Atmos.*, 104, 23 871–23 880, 1999. [6212](#)
- Ehhalt, D., Prather, M. J., Dentener, F., Derwent, R., Dlugokencky, E., Holland, E., Isaksen, I., Katima, J., Kirchhoff, V., Matson, P., Midgley, P., and Wang, M.: Atmospheric Chemistry and Greenhouse Gases, in: *Climate Change 2001: The Scientific Basis*, edited by: Houghton, J., Ding, Y., Griggs, D., Noguer, M., van der Linden, P., Dai, X., Maskell, K., and Johnson, C., p. 892, Cambridge University Press, Cambridge, UK, 2001. [6206](#), [6210](#), [6211](#)

MAGICC 6.0

M. Meinshausen et al.

[Title Page](#)[Abstract](#)[Introduction](#)[Conclusions](#)[References](#)[Tables](#)[Figures](#)[◀](#)[▶](#)[◀](#)[▶](#)[Back](#)[Close](#)[Full Screen / Esc](#)[Printer-friendly Version](#)[Interactive Discussion](#)

MAGICC 6.0

M. Meinshausen et al.

Title Page

Abstract

Introduction

Conclusions

References

Tables

Figures

◀

▶

◀

▶

Back

Close

Full Screen / Esc

Printer-friendly Version

Interactive Discussion



- Folland, C. K., Rayner, N. A., Brown, S. J., Smith, T. M., Shen, S. S. P., Parker, D. E., Macadam, I., Jones, P. D., Jones, R. N., Nicholls, N., and Sexton, D. M. H.: Global temperature change and its uncertainties since 1861, *Geophys. Res. Lett.*, 28, 2621–2624, 2001. [6261](#)
- Forster, P., Ramaswamy, V., Artaxo, P., Bernsten, T., Betts, R., Fahey, D., Haywood, J., Lean, J., Lowe, D., Myhre, G., Nganga, J., Prinn, R., Raga, G., Schulz, M., and Van Dorland, R.: Chapter 2: Changes in Atmospheric Constituents and in Radiative Forcing, in: *IPCC Fourth Assessment Report WG 1*, edited by IPCC, Cambridge University Press, Cambridge, 2007. [6164](#), [6170](#), [6171](#), [6172](#), [6185](#), [6218](#)
- Forster, P. M. D. and Taylor, K. E.: Climate forcings and climate sensitivities diagnosed from coupled climate model integrations, *J. Climate*, 19, 6181–6194, 2006. [6157](#), [6168](#), [6169](#), [6170](#), [6180](#), [6185](#), [6188](#), [6189](#), [6190](#), [6194](#), [6242](#), [6244](#), [6245](#), [6252](#), [6253](#), [6259](#), [6261](#)
- Friedlingstein, P., Cox, P., Betts, R., Bopp, L., von Bloh, W., Brovkin, V., Cadule, P., Doney, S., Eby, M., Fung, I., Bala, G., John, J., Jones, C., Joos, F., Kato, T., Kawamiya, M., Knorr, W., Lindsay, K., Matthews, H., Raddatz, T., Rayner, P., Reick, C., Roeckner, E., Schnitzler, K.-G., Schnur, R., Strassmann, K., Weaver, K., Yoshikawa, C., and Zeng, N.: ClimateCarbon Cycle Feedback Analysis: Results from the C4MIP Model Intercomparison, *J. Climate*, 19, 3337–3353, 2006. [6158](#), [6163](#), [6174](#), [6250](#)
- Gates, D.: Global biospheric response to increasing atmospheric carbon dioxide concentration, in: *Direct effects of increasing carbon dioxide on vegetation*, edited by: Strain, B. and Cure, J., pp. 171–184, DOE/ER0238, U.S. Dept. of Energy, Carbon Dioxide Research Division, Washington, DC, 1985. [6201](#)
- Gifford, R.: Implications of CO₂ effects on vegetation for the global carbon budget, in: *The global carbon cycle*, edited by: Heimann, M., 115, 159–200, Springer-Verlag, Berlin, 1993. [6202](#)
- Gregory, J. M. and Webb, M.: Tropospheric Adjustment induces a cloud component of CO₂ forcing, *J. Climate*, 21, 58–71, 2008. [6162](#)
- Gregory, J. M., Ingram, W. J., Palmer, M. A., Jones, G. S., Stott, P. A., Thorpe, R. B., Lowe, J. A., Johns, T. C., and Williams, K. D.: A new method for diagnosing radiative forcing and climate sensitivity, *Geophys. Res. Lett.*, 31, L03205, 2004. [6188](#), [6245](#)
- Gultepe, I. and Isaac, G.: Scale Effects on Averaging of Cloud Droplet and Aerosol Number Concentrations: Observations and Models, *J. Clim.*, 12, 1268, 1999. [6213](#)
- Hansen, J., Sato, M., Ruedy, R., Nazarenko, L., Lacis, A., Schmidt, G. A., Russell, G., Aleinov, I., Bauer, M., Bauer, S., Bell, N., Cairns, B., Canuto, V., Chandler, M., Cheng, Y., Del Genio,

MAGICC 6.0

M. Meinshausen et al.

Title Page

Abstract

Introduction

Conclusions

References

Tables

Figures

I◀

▶I

◀

▶

Back

Close

Full Screen / Esc

Printer-friendly Version

Interactive Discussion



A., Faluvegi, G., Fleming, E., Friend, A., Hall, T., Jackman, C., Kelley, M., Kiang, N., Koch, D., Lean, J., Lerner, J., Lo, K., Menon, S., Miller, R., Minnis, P., Novakov, T., Oinas, V., Perlwitz, J., Perlwitz, J., Rind, D., Romanou, A., Shindell, D., Stone, P., Sun, S., Tausnev, N., Thresher, D., Wielicki, B., Wong, T., Yao, M., and Zhang, S.: Efficacy of climate forcings, *J. Geophys. Res.*, 110, D18104, doi: 10.1029/2005JD005776, 2005. [6157](#), [6165](#), [6169](#), [6209](#), [6211](#), [6212](#), [6213](#), [6217](#), [6218](#), [6219](#)

Harvey, L.: Managing atmospheric CO₂, *Climatic Change*, 15, 343–381, 1989. [6163](#)

Harvey, L. and Schneider, S.: Transient Climate Response to External Forcing on 10(0)-10(4) Year Time Scales.1. Experiments with Globally Averaged, Coupled, Atmosphere and Ocean Energy-Balance Models, *J. Geophys. Res.-Atmos.*, 90, 2191–2205, 1985a. [6155](#), [6224](#), [6225](#)

Harvey, L. and Schneider, S. H.: Transient Climate Response to External Forcing on 10(0)-10(4) Year Time Scales.2. Sensitivity Experiments with a Seasonal, Hemispherically Averaged, Coupled Atmosphere, Land, and Ocean Energy-Balance Model, *J. Geophys. Res.-Atmos.*, 90, 2207–2222, 1985b. [6155](#), [6224](#), [6225](#)

Harvey, L., Gregory, J. M., Hoffert, M., Jain, A., Lal, M., Leemans, R., Raper, S. C. B., Wigley, T. M. L., and de Wolde, J.: An Introduction to Simple Climate Models used in the IPCC Second Assessment Report, Tech. rep., Intergovernmental Panel on Climate Change, 1997. [6165](#), [6225](#)

Hasselmann, K., Sausen, R., Maierreimer, E., and Voss, R.: On the Cold Start Problem in Transient Simulations with Coupled Atmosphere-Ocean Models, *Clim. Dynam.*, 9, 53–61, 1993. [6171](#), [6254](#)

Hegerl, G., Zwiers, F. W., Braconnot, P., Gillett, N., Luo, Y., Marengo Orsini, J., Nicholls, N., Penner, J., and Stott, P.: Understanding and Attributing Climate Change, in: *Climate Change 2007: The Physical Science Basis. Contribution of Working Group I to the Fourth Assessment Report of the Intergovernmental Panel on Climate Change*, edited by: Solomon, S., Qin, D., Manning, M., Chen, Z., Marquis, M., Averyt, K., Tignor, M., and Miller, H., Cambridge University Press, Cambridge, United Kingdom and New York, NY, USA, 2007. [6192](#)

Hoffert, M. I., Callegari, A. J., and Hsieh, C. T.: The Role of Deep-Sea Heat-Storage in the Secular Response to Climatic Forcing, *J. Geophys. Res.*, 85, 6667–6679, 1980. [6155](#), [6213](#), [6225](#)

IPCC: *Climate Change: The IPCC Scientific Assessment*, Cambridge University Press, Cambridge, UK, UK, 365 pp., 1990. [6168](#), [6209](#)

MAGICC 6.0

M. Meinshausen et al.

[Title Page](#)[Abstract](#)[Introduction](#)[Conclusions](#)[References](#)[Tables](#)[Figures](#)[I◀](#)[▶I](#)[◀](#)[▶](#)[Back](#)[Close](#)[Full Screen / Esc](#)[Printer-friendly Version](#)[Interactive Discussion](#)

- Johns, T. C., Carnell, R. E., Crossley, J. F., Gregory, J. M., Mitchell, J. F. B., Senior, C. A., Tett, S. F. B., and Wood, R. A.: The second Hadley Centre coupled ocean-atmosphere GCM: Model description, spinup and validation, *Clim. Dynam.* 13, 103–134, 1997. [6172](#)
- Jones, P. and Wigley, T. M. L.: Detection of greenhouse-gas-induced climatic change. Progress report, 1 July 1994 – 31 July 1995, Technical report, Climatic Research Unit, East Anglia Univ., 1995. [6214](#)
- Jones, P. D. and Moberg, A.: Hemispheric and large-scale surface air temperature variations: An extensive revision and an update to 2001, *J. Climate*, 16, 206–223, 2003. [6261](#)
- Joos, F., Bruno, M., Stocker, T., Siegenthaler, U., Le Quere, C., and Sarmiento, J.: An efficient and accurate representation of complex oceanic and biospheric models of anthropogenic carbon uptake, *Tellus B*, 48B, 397–417, 1996. [6163](#), [6175](#), [6204](#)
- Joos, F., Prentice, I. C., Sitch, S., Meyer, R., Hooss, G., Plattner, G.-K., Gerber, S., and Hasselmann, K.: Global Warming feedbacks on terrestrial carbon uptake under the Intergovernmental Panel on Climate Change (IPCC) emission scenarios, *Global Biogeochem. Cy.*, 15, 891–907, 2001. [6163](#), [6204](#), [6205](#)
- Joshi, M., Shine, K., Ponater, M., Stuber, N., Sausen, R., and Li, L.: A comparison of climate response to different radiative forcings in three general circulation models: towards an improved metric of climate change, *Clim. Dynam.*, 20, 843, 2003. [6165](#), [6219](#)
- Kattenberg, A., Giorgi, F., Grassl, H., Meehl, G., Mitchell, J. F. B., Stouffer, R. J., Tokika, T., Weaver, A. J., and Wigley, T. M. L.: Climate models - Projection of future climate. Pp. 285–357 (Chapter 6), in: *Climate Change 1995: The Science of Climate Change*, Contribution of Working Group I to the Second Assessment Report of the Intergovernmental Panel on Climate Change, edited by Houghton, J., Meira Filho, L., Callander, B., Harris, N., Kattenberg, A., and Maskell, K., p. 572, Cambridge University Press, Cambridge, 1996. [6156](#)
- Knutti, R., Allen, M., Friedlingstein, P., Gregory, J., Hegerl, G., Meehl, G., Meinshausen, M., Murphy, J., Plattner, G.-K., Raper, S., Stocker, T., Stott, P., Teng, H., and Wigley, T. M. L.: A review of uncertainties in global temperature projections over the twenty-first century, *J. Climate*, in press, 2008. [6179](#), [6192](#), [6196](#)
- Manabe, S. and Bryan, K.: Climate Calculations with a Combined Ocean-Atmosphere Model, *J. Atmos. Sci.*, 26, 786–789, 1969. [6155](#)
- Manabe, S., Bryan, K., and Spelman, M. J.: Global Ocean-Atmosphere Climate Model.1. Atmospheric Circulation, *J. Phys. Oceanogr.*, 5, 3–29, 1975. [6155](#)
- Mann, M.: On smoothing potentially non-stationary climate time series, *Geophys. Res. Lett.*,

31, 2004. [6231](#), [6269](#)

Meehl, G. A., Covey, C., McAvaney, B., Latif, M., and Stouffer, R.: Overview of coupled model intercomparison project, *Bulletin of the American Meteorological Society (BAMS)*, 86, 2005a. [6180](#)

5 Meehl, G. A., Washington, W. M., Collins, W. D., Arblaster, J. M., Hu, A. X., Buja, L. E., Strand, W. G., and Teng, H. Y.: How much more global warming and sea level rise?, *Science*, 307, 1769–1772, 2005b. [6193](#)

Meehl, G. A., Stocker, T. F., Collins, W., Friedlingstein, P., Gaye, A., Gregory, J. M., Kitoh, A., Knutti, R., Murphy, J., Noda, A., Raper, S. C. B., Watterson, I., Weaver, A., and Zhao, Z.-C.: Chapter 10: Global Climate Projections, in: *IPCC Fourth Assessment Report*, edited by: IPCC, Cambridge University Press, Cambridge, 2007. [6157](#), [6168](#), [6171](#), [6173](#), [6188](#), [6191](#), [6192](#), [6209](#), [6242](#), [6247](#), [6261](#)

10 Meinshausen, M.: What does a 2C target mean for greenhouse gas concentrations? - A brief analysis based on multi-gas emission pathways and several climate sensitivity uncertainty estimates., in: *Avoiding Dangerous Climate Change*, edited by: Schellnhuber, J., Cramer, W., Nakicenovic, N., Wigley, T., and Yohe, G., Cambridge University Press, Cambridge, 2006. [6193](#)

15 Meinshausen, M., Hare, B., Wigley, T. M. L., van Vuuren, D., den Elzen, M. G. J., and Swart, R.: Multi-gas emission pathways to meet climate targets, *Climatic Change*, 75, 151–194, 2006. [6246](#)

20 Metz, B., Kuijpers, L., Solomon, S., Andersen, S., Davidson, O., Pons, J., de Jager, D., Kestin, T., Manning, M., and Meyer, L., eds.: *Safeguarding the Ozone Layer and the Global Climate System: Issues Related to Hydrofluorocarbons and Perfluorocarbons*, Intergovernmental Panel on Climate Change, Cambridge, 2005. [6208](#)

25 Murphy, J. M. and Mitchell, J. F. B.: Transient-Response of the Hadley-Center Coupled Ocean-Atmosphere Model to Increasing Carbon-Dioxide.2. Spatial and Temporal Structure of Response, *J. Climate*, 8, 57–80, 1995. [6161](#), [6188](#), [6190](#)

Myhre, G., Highwood, E. J., Shine, K. P., and Stordal, F.: New estimates of radiative forcing due to well mixed greenhouse gases, *Geophys. Res. Lett.*, 25, 2715–2718, 1998. [6168](#), [6172](#), [6209](#), [6210](#), [6247](#)

30 Nakicenovic, N. and Swart, R.: *IPCC Special Report on Emissions Scenarios*, Cambridge University Press, Cambridge, United Kingdom, 570 pp., 2000. [6203](#)

O'Neill, B. and Melnikov: Learning about parameter and structural uncertainty in carbon cycle

MAGICC 6.0

M. Meinshausen et al.

Title Page

Abstract

Introduction

Conclusions

References

Tables

Figures

◀

▶

◀

▶

Back

Close

Full Screen / Esc

Printer-friendly Version

Interactive Discussion



MAGICC 6.0

M. Meinshausen et al.

Title Page

Abstract

Introduction

Conclusions

References

Tables

Figures

I◀

▶I

◀

▶

Back

Close

Full Screen / Esc

Printer-friendly Version

Interactive Discussion



- models, Climatic Change, in press, 2008. [6156](#)
- Osborn, T., Raper, S., and Briffa, K.: Simulated climate change during the last 1000 years: comparing the ECHO-G general circulation model with the MAGICC simple climate model., *Clim. Dynam.*, 27, 185–197, 2006. [6156](#)
- 5 Ramaswamy, V., Boucher, O., Haigh, J., Hauglustaine, D., Haywood, J., Myhre, G., Nakajima, T., Shi, G., and Solomon, S.: Radiative Forcing of Climate Change, in: *Climate Change 2001: The Scientific Basis*, edited by: Houghton, J., Ding, Y., Griggs, D., Noguer, M., van der Linden, P., Dai, X., Maskell, K., and Johnson, C., , Cambridge University Press, 892 pp., Cambridge, UK, 2001. [6210](#)
- 10 Randall, D., Wood, R., Bony, S., Colman, R., Fichefet, T., Fyfe, J., Kattsov, V., Pitman, A., Shukla, J., Srinivasan, J., Stouffer, R., Sumi, A., and Taylor, K. E.: Chapter 8: Climate Models and Their Evaluation, in: *IPCC Fourth Assessment Report*, edited by: IPCC, Cambridge University Press, Cambridge, 590–662, 2007. [6244](#), [6245](#)
- Rao, S. and Riahi, K.: The role of Non-CO2 greenhouse gases in climate change mitigation: Long-term scenarios for the 21st century, *Energy Journal*, 177–200, 2006. [6208](#)
- 15 Rao, S., Riahi, K., Kupiainen, K., and Klimont, Z.: Long-term scenarios for black and organic carbon emissions, *Environmental Sciences*, 2, 205–216, 2005. [6208](#)
- Raper, S. C. B.: Interpretation of Model Results that Show Changes in the Effective Climate Sensitivity with Time, in: *IPCC Workshop on Climate Sensitivity*, edited by IPCC, pp. 131–133, IPCC, available at http://ipcc-wg1.ucar.edu/meeting/CSW/product/CSW_Report.pdf, Paris, France, 2004. [6162](#)
- 20 Raper, S. C. B. and Cubasch, U.: Emulation of the results from a coupled general circulation model using a simple climate model, *Geophys. Res. Lett.*, 23, 1107–1110, 1996. [6156](#), [6220](#)
- Raper, S. C. B., Wigley, T. M. L., and Warrick, R. A.: Global Sea-level Rise: Past and Future, in: *Sea-Level Rise and Coastal Subsidence: Causes, Consequences and Strategies*, edited by Milliman, J. and Haq, B., 11–45, Kluwer, Dordrecht, Netherlands, 1996. [6159](#)
- 25 Raper, S. C. B., Gregory, J. M., and Osborn, T. J.: Use of an upwelling-diffusion energy balance climate model to simulate and diagnose A/OGCM results, *Clim. Dynam.*, 17, 601–613, 2001. [6156](#), [6161](#), [6164](#), [6188](#), [6190](#), [6217](#), [6220](#), [6224](#)
- 30 Sarmiento, J. L., Orr, J. C., and Siegenthaler, U.: A perturbation simulation of CO₂ uptake in an ocean general circulation model, *J. Geophys. Res.*, 97, 3621–3645, 1992. [6163](#), [6204](#)
- Schlesinger, M.: Mathematical modeling and simulation of climate and climate change. Contribution n 41, Tech. rep., Institut D’Astronomie et de Geophysique George Lemaitre, Univer-

- sität Catholique de Louvain, Louvain-la-Neuve, Belgium, 1984. [6213](#)
- Schlesinger, M. E. and Jiang, X. J.: Simple-Model Representation of Atmosphere-Ocean Gcms and Estimation of the Time Scale of CO₂-Induced Climate Change, *J. Climate*, 3, 1297–1315, 1990. [6155](#)
- 5 Schlesinger, M. E. and Jiang, X. J.: Revised Projection of Future Greenhouse Warming, *Nature*, 350, 219–221, 1991. [6155](#)
- Schneider, S. H. and Thompson, S. L.: Atmospheric CO₂ and Climate – Importance of the Transient-Response, *J. Geophys. Res.*, 86, 3135–3147, 1981. [6155](#)
- Senior, C. A. and Mitchell, J. F. B.: The time-dependence of climate sensitivity, *Geophys. Res. Lett.*, 27, 2685–2688, 2000. [6161](#), [6188](#), [6190](#)
- 10 Stainforth, D. A., Aina, T., Christensen, C., Collins, M., Faull, N., Frame, D. J., Kettleborough, J. A., Knight, S., Martin, A., Murphy, J. M., Piani, C., Sexton, D., Smith, L. A., Spicer, R. A., Thorpe, A. J., and Allen, M. R.: Uncertainty in predictions of the climate response to rising levels of greenhouse gases, *Nature*, 433, 403–406, 2005. [6155](#)
- 15 Stern, N.: *The Economics of Climate Change – The Stern Review*, Cambridge University Press, Cambridge, UK, 2006. [6193](#)
- Stott, P. A., Tett, S. F. B., Jones, G. S., Allen, M. R., Mitchell, J. F. B., and Jenkins, G. J.: External Control of 20th Century Temperature by Natural and Anthropogenic Forcings, *Science*, 290, 2133–2137, 2000. [6173](#)
- 20 Stouffer, R. J.: Time scales of climate response, *J. Climate*, 17, 209–217, 2004. [6190](#)
- Takahashi, T., Olafson, J., Goddard, J., Chipman, D., and Sutherland, S.: Seasonal variation of CO₂ and nutrients in the high-latitude surface oceans: A comparative study, *Global Biogeochem. Cy.*, 7, 843–878, 1993. [6163](#), [6205](#)
- Takemura, T., Tsushima, Y., Yokohata, T., Nozawa, T., Nagashima, T., and Nakajima, T.: Time evolutions of various radiative forcings for the past 150 years estimated by a general circulation model, *Geophys. Res. Lett.*, 33, L19705, 2006. [6157](#), [6208](#)
- 25 Tebaldi, C. and Knutti, R.: The use of the multi-model ensemble in probabilistic climate projections, *Philos. T. R. Soc. A*, 365, 2053–2075, 2007. [6191](#)
- Trenberth, K. E. and Guillemot, C. J.: The Total Mass of the Atmosphere, *J. Geophys. Res.-Atmos.*, 99, 23 079–23 088, 1994. [6208](#)
- 30 Twomey, S.: The influence of pollution on the shortwave albedo of clouds, *J. Atmos. Sci.*, 34, 1149–1152, 1977. [6164](#), [6213](#)
- UNDP: Human Development Report 2007/2008: Fighting climate change: Human solidarity in

MAGICC 6.0

M. Meinshausen et al.

Title Page

Abstract

Introduction

Conclusions

References

Tables

Figures

◀

▶

◀

▶

Back

Close

Full Screen / Esc

Printer-friendly Version

Interactive Discussion



- a divided world, Palgrave Macmillan, New York, USA, 2007. [6193](#)
- Wigley, T. and Raper, S.: Thermal-Expansion of Sea-Water Associated with Global Warming, *Nature*, 330, 127–131, 1987. [6159](#)
- Wigley, T. M. L.: Could reducing fossil-fuel emissions cause global warming?, *Nature*, 349, 503–506, 1991a. [6212](#)
- 5 Wigley, T. M. L.: A Simple Inverse Carbon Cycle Model, *Global Biogeochem. Cy.*, 5, 373–382, 1991b. [6163](#)
- Wigley, T. M. L.: Balancing the Carbon Budget – Implications for Projections of Future Carbon-Dioxide Concentration Changes, *Tellus B*, 45, 409–425, 1993. [6163](#), [6201](#)
- 10 Wigley, T. M. L.: The climate change commitment, *Science*, 307, 1766–1769, 2005. [6193](#)
- Wigley, T. M. L. and Raper, S. C. B.: Implications for climate and sea level of revised IPCC emissions scenarios, *Nature*, 357, 293–300, 1992. [6159](#)
- Wigley, T. M. L. and Raper, S. C. B.: Interpretation of high projections for global-mean warming, *Science*, 293, 451–454, 2001. [6159](#), [6196](#)
- 15 Wigley, T. M. L. and Schlesinger, M.: Analytical Solution for the effect of increasing CO₂ on global mean temperature, *Nature*, 315, 649–652, 1985. [6215](#)
- Wigley, T. M. L., Richels, R., and Edmonds, J.: Overshoot pathways to CO₂ stabilization in a multi-gas context, in: *Human Induced Climate Change: An Interdisciplinary Assessment*, edited by: Schlesinger, M., Kheshgi, H., Smith, J., de la Chesnaye, F., Reilly, J., Wilson, T., and Kostad, C., 84–92, Cambridge University Press, Cambridge, UK, 84–92, 2007. [6195](#)
- 20 WMO: Scientific Assessment of Ozone Depletion: 2006, Tech. Rep., World Meteorological Organization, 2006. [6208](#)

[Title Page](#)[Abstract](#)[Introduction](#)[Conclusions](#)[References](#)[Tables](#)[Figures](#)[◀](#)[▶](#)[◀](#)[▶](#)[Back](#)[Close](#)[Full Screen / Esc](#)[Printer-friendly Version](#)[Interactive Discussion](#)

Table 1. Overview of calibration exercises.

| Calibration Method | Experiments Used | Calibrated Parameters ^a |
|---------------------|--|---|
| I. “Basic/AR4-like” | Idealized Scenarios (1pctto2x, 1pctto4x) | ΔT_{2x} , RLO, Kz |
| II. “Medium” | Idealized Scenarios (1pctto2x, 1pctto4x) | ΔT_{2x} , ξ , RLO, Kz, $\frac{dKz_{top}}{dT}$, k_{NS} , k_{LO} , μ |
| III. “Full” | Idealized Scenarios (1pctto2x, 1pctto4x) and Multi-Forcing Runs (20c3m, commit, sresb1, sresa1b) | ΔT_{2x} , ξ , RLO, Kz, $\frac{dKz_{top}}{dT}$, k_{NS} , k_{LO} , μ |

^a The calibrated parameters are as follows: ΔT_{2x} =climate sensitivity (KW^{-1}m^2), i.e., warming after a doubling of CO_2 concentrations; RLO=Land-Ocean warming ratio at equilibrium; Kz=vertical diffusivity in ocean (cm^2s^{-1}); ξ =sensitivity of feedback factors λ to radiative forcing change ΔQ away from doubled pre-industrial CO_2 forcing level ΔQ_{2x} , see Eq. (A52); $\frac{dKz_{top}}{dT}$ =sensitivity of vertical diffusivity at mixed layer boundary to global-mean surface temperatures (i.e., thermal stratification). A linear diffusivity profile change is assumed for layers between mixed and bottom layer; k_{LO} = Land-Ocean heat exchange coefficient ($\text{Wm}^{-2}\text{K}^{-1}$); μ = an amplification factor for the ocean to land heat exchange (see Eq. A51).

Title Page

Abstract

Introduction

Conclusions

References

Tables

Figures

◀

▶

◀

▶

Back

Close

Full Screen / Esc

Printer-friendly Version

Interactive Discussion



Table 2.

| | Emulations IIIa-IIIb |
|--------------------------------|---|
| (BCCR-BCM2.0) | CMNstFDula |
| (BCC-CM1) | CMNstFDiva |
| CCSM3 | CMNSTFDBOuv _(0.86) a |
| CGCM3.1(T47) | CMNstFDulv _(0.0) a |
| (CGCM3.1(T63)) | CMNstFDulv _(0.0) a |
| CNRM-CM3 | CMNSTFDu |
| CSIRO-Mk3.0 | CMNSTFD |
| ECHAM5/MPI-OM | CMNstFDI ^{1*} |
| ECHO-G | CMNsTFDI ¹ v _(0.70) a |
| FGOALS-g1.0 | CMNstFDa |
| GFDL-CM2.0 | CMNSTFDBOulv _(0.70) a |
| GFDL-CM2.1 | CMNSTFDBOulv _(0.70) a |
| (GISS-AOM) | CMNstFD |
| GISS-EH | CMNSTFDBORI ² uLv _(0.70) a' |
| GISS-ER | CMNSTFDBORI ² uLv _(0.70) a' |
| INM-CM3.0 | CMNstDv _(0.2) a |
| IPSL-CM4 | CMNFDI ¹ |
| MIROC3.2(H) | CMNSTFDBOI ^{1,2} Ulv _(0.52) a |
| MIROC3.2(M) | CMNSTFDBOI ^{1,2} Ulv _(0.35) a |
| MRI-CGCM2.3.2 | CMNstFDv _(0.40) a |
| PCM | CMNSTFDv _(0.7) a |
| UKMO-HadCM3 | CMNSTFDI ^{1*} v _(0.0) a |
| UKMO-HadGEM1 "Full Forcing" | CMNSTFDBOI ^{1,2} Lv _(0.0) a |
| Emulation IIIc/d | CMNSTFDBOI ^{1,2} ulv _(0.7) a |

Title Page

Abstract

Introduction

Conclusions

References

Tables

Figures

◀

▶

◀

▶

Back

Close

Full Screen / Esc

Printer-friendly Version

Interactive Discussion



MAGICC 6.0

M. Meinshausen et al.

Table 2. The subsets of considered forcing agents during the “calibration III” exercise to match the setup of CMIP3 AOGCMs multi-forcing runs (cf. Table 10.1, Meehl et al., 2007).

^a The forcing agents included for the multi-forcing simulations are indicated by the following symbols: C=carbon dioxide; M=methane; N=nitrous oxide; S=stratospheric ozone; T=tropospheric ozone; F=halogenated carbons (CFCs); D=direct SO_x aerosol; B=direct black carbon; O=direct organic carbon; R=nitrate aerosols; I¹=first indirect aerosol effects; I²=second indirect aerosol effects; U=mineral dust; L=landuse; V=volcanic; A=solar; Capital letters denote that a time-variable forcing agent is included for simulations prior and after 2000; small letters denote that forcing agent varies with time in 20th century (20c3m) simulations and is set constant thereafter; italic letters denote that forcing was included as CO₂ equivalent, hence efficacies were set to 1 during calibration. Bracketed subscripts indicate the applied volcanic forcing scaling factor derived from Fig. 4 in Forster and Taylor (2006). Note that for some models, the forcing analysis by Forster and Taylor (2006) detects no volcanic forcing ($v_{(0)}$), although Table 10.1 in Meehl et al. (2007) indicate the inclusion of volcanic aerosols. Future solar forcing in GISS-EH and GISS-ER has been assumed cyclic, but is here assumed constant, denoted by a'. Mineral dust (U) forcings and land use albedo (L) effects have been assumed constant after 2000 in all emulations IIIa-IIIId. For ECHAM5/MPI-OM and UKMO-HadCM3, denoted with a “*”, the first indirect effect was assumed equal to the default joint forcing of 1st and 2nd indirect effect ($=-0.7 \text{ Wm}^{-2} * 1.5$ efficacy) given the substantial negative shortwave forcing analyzed by Forster and Taylor (2006) for these models.

Title Page

Abstract

Introduction

Conclusions

References

Tables

Figures

I◀

▶I

◀

▶

Back

Close

Full Screen / Esc

Printer-friendly Version

Interactive Discussion



Table 3. Comparison of global-mean temperatures from AOGCMs and emulations for three periods. The means across all available CMIP3 AOGCMs for each scenario (number of available AOGCM datasets given in column “n”) are compared to the mean across the matching number of emulations (IIIa) using AOGCM-specific “like-with-like” forcings. Furthermore, the “full” forcing emulations, averaged across all 19 emulations, are shown (column III d).

| Scenario | n | Period 1: 1980–1999 vs. startyear | | Period 2: 2090–2099 vs. 1980–1999 | | | Period 3: 2100 vs. 2090–2099 | | | |
|----------|----|-----------------------------------|-----------|-----------------------------------|-------|-----------|------------------------------|-------|-----------|-------|
| | | AOGCM | Emulation | | AOGCM | Emulation | | AOGCM | Emulation | |
| | | | IIIa | III d | | IIIa | III d | | IIIa | III d |
| COMMIT | 16 | 0.56 | 0.59 | 0.50 | 0.58 | 0.48 | 0.57 | – | 0.00 | 0.01 |
| SRESA1B | 19 | 0.54 | 0.61 | 0.53 | 2.82 | 2.79 | 2.77 | – | 0.10 | 0.10 |
| SRESA2 | 16 | 0.58 | 0.59 | 0.50 | 3.32 | 3.30 | 3.20 | – | 0.27 | 0.25 |
| SRESB1 | 17 | 0.56 | 0.59 | 0.50 | 1.85 | 1.89 | 1.90 | – | 0.03 | 0.06 |

[Title Page](#)
[Abstract](#)
[Introduction](#)
[Conclusions](#)
[References](#)
[Tables](#)
[Figures](#)
[Back](#)
[Close](#)
[Full Screen / Esc](#)
[Printer-friendly Version](#)
[Interactive Discussion](#)


MAGICC 6.0

M. Meinshausen et al.

Title Page

Abstract

Introduction

Conclusions

References

Tables

Figures

I ◀

▶ I

◀

▶

Back

Close

Full Screen / Esc

Printer-friendly Version

Interactive Discussion



Table 4.

| AOGCM | IPCC AR4 Slab Ocean | Forster& Taylor | IPCC AR4 MAGICC 4.2 | This Study (MAGICC 6.0) | | |
|---------------|------------------------|--------------------|------------------------|-------------------------|------------------|------------------|
| | | | | Calibration:(I) | (II) | (III) |
| BCCR-BCM2.0 | n/a | n/a | n/a | n/a | n/a | n/a |
| BCC-CM1 | n/a | n/a | n/a | n/a | n/a | n/a |
| CCSM3 | 2.7 | 2.1 | 2.4 | 2.4 | 2.2 ^c | 2.1 ^c |
| CGCM3.1(T47) | 3.4 | 3.0 | 3.0 | 3.1 | 3.3 | 3.0 |
| CGCM3.1(T63) | 3.4 ^a | 3.6 ^b | n/a | n/a | n/a | |
| CNRM-CM3 | n/a | 2.5 ^b | 2.5 | 2.5 | 2.2 ^c | 3.0 |
| CSIRO-Mk3.0 | 3.1 | 2.3 ^b | 2.2 | 2.2 | 2.2 | 2.2 |
| ECHAM5/MPI-OM | 3.4 | 3.6 | 3.9 | 3.9 | 3.5 ^c | 3.2 ^c |
| ECHO-G | 3.2 | 2.5 ^b | 3.0 | 3.1 | 3.1 | 2.6 |
| FGOALS-g1.0 | 2.3 ^a | 2.0 ^b | 2.0 | 2.1 | 2.1 | 2.4 ^c |
| GFDL-CM2.0 | 2.9 | 2.3 ^b | 2.4 | 2.4 | 2.3 ^c | 2.3 ^c |
| GFDL-CM2.1 | 3.4 | 2.1 ^b | 2.3 | 2.3 | 2.2 ^c | 2.3 ^c |
| GISS-AOM | n/a | n/a | n/a | n/a | n/a | |
| GISS-EH | 2.7 | 2.5 | 3.0 | 2.8 | 2.9 | 2.5 |
| GISS-ER | 2.7 | 2.2 ^b | 2.6 | 2.7 | 2.5 ^c | 2.3 ^c |
| INM-CM3.0 | 2.1 | 2.3 ^b | 2.3 | 2.3 | 2.3 | 2.4 |
| IPSL-CM4 | 4.4 | 3.8 | 3.8 | 3.9 | 4.0 | 4.1 |
| MIROC3.2(H) | 4.3 | 3.9 | 5.9 | 6.0 | 6.3 | 5.7 |
| MIROC3.2(M) | 4.0 | 3.7 | 3.9 | 4.1 | 4.1 | 4.0 |
| MRI-CGCM2.3.2 | 3.2 | 3.0 ^b | 3.0 | 2.8 | 2.9 | 2.5 |
| PCM | 2.1 | 2.0 ^b | 1.9 | 1.9 | 1.8 ^c | 1.9 |
| UKMO-HadCM3 | 3.3 | 3.0 | 3.1 | 3.1 | 3.1 | 3.2 |
| UKMO-HadGEM1 | 4.4 | 2.7 | 2.6 | 3.1 | 2.9 ^c | 3.0 ^c |
| AVERAGE | 3.21 | 2.76 | 2.93 | 2.99 | 2.95 | 2.88 |

^a These climate sensitivities were estimated from the coupled model versions available in the PCMDI database, while other values in this column denote reported equilibrium climate sensitivities of the slab-ocean model versions (Table 8.2 [Randall et al., 2007](#)).

^b Derived feedback constant using a default 3.7 Wm^{-2} value for forcing at doubled CO_2 concentrations, given that no ΔQ_{2x} value was available (see Table 2 of [Forster and Taylor, 2006](#)).

^c Note that these calibrations II and III include a non-zero sensitivity parameter ξ for climate feedback upon forcing. The effective climate sensitivity S is therefore increasing for forcings higher than twice pre-industrial CO_2 concentrations (ΔQ_{2x}).

MAGICC 6.0

M. Meinshausen et al.

Table 4. Comparison of retrieved climate sensitivities for CMIP3 AOGCMs (ΔQ_{2x}). The first column shows climate sensitivities estimated for the slab-ocean versions of the AOGCMs as given in Table 8.2 of [Randall et al. \(2007\)](#). The second column provides the climate sensitivities derived from the net climate feedbacks given by [Forster and Taylor \(2006\)](#), who use the method by [Gregory et al. \(2004\)](#) to retrieve feedbacks within the idealized 1% CO₂ scenarios. These climate feedbacks λ were converted to climate sensitivities ΔT_{2x} using $\Delta T_{2x} = \frac{\Delta Q_{2x}}{\lambda}$, with the forcing ΔQ_{2x} at doubled CO₂ concentrations taken from Table 2 in [Forster and Taylor \(2006\)](#), where available, and using 3.7 Wm^{-2} as default. The third column presents results for the MAGICC 4.2 calibration as done for IPCC AR4 and presented in Table S8.1 in [Randall et al. \(2007\)](#). The fourth to sixth column present this study's results using MAGICC 6.0 under calibration exercises I, II and III (see Table 1). The last row provides the average climate sensitivities for each column.

[Title Page](#)[Abstract](#)[Introduction](#)[Conclusions](#)[References](#)[Tables](#)[Figures](#)[I ◀](#)[▶ I](#)[◀](#)[▶](#)[Back](#)[Close](#)[Full Screen / Esc](#)[Printer-friendly Version](#)[Interactive Discussion](#)

Table 5. Distributions of temperature projections for 2050, 2075 and 2100 for the six SRES marker scenarios and the “Year 2000 concentration stabilization” (COMMIT) experiment – relative to the 1980–1999 mean. The distribution percentiles in the header row denote the cumulative density of occurrence of the 190 emulations of cross-combination between calibrations to 19 CMIP3 AOGCM and 10 C4MIP carbon cycle. The bottom row indicates the average deviations from the mean across all six SRES scenarios and the three time slices. In addition, distributions are provided for the HALVED-BY-2050 EQW emission pathway (Meinshausen et al., 2006) shown in Fig. 10.

| Scenario | Years | MIN | 5% | 16.7% | MEDIAN | MEAN | 83.3% | 95% | MAX |
|----------------|-------|------|------|-------|--------|------|-------|------|------|
| SRES A1B | 2050 | 1.00 | 1.10 | 1.23 | 1.51 | 1.57 | 1.85 | 2.18 | 2.77 |
| | 2075 | 1.42 | 1.64 | 1.83 | 2.27 | 2.33 | 2.77 | 3.27 | 4.40 |
| | 2100 | 1.65 | 1.94 | 2.18 | 2.78 | 2.87 | 3.44 | 4.14 | 5.89 |
| SRES A1FI | 2050 | 1.11 | 1.22 | 1.36 | 1.67 | 1.71 | 1.99 | 2.35 | 2.94 |
| | 2075 | 1.87 | 2.14 | 2.39 | 2.97 | 3.02 | 3.51 | 4.28 | 5.32 |
| | 2100 | 2.43 | 2.85 | 3.26 | 3.96 | 4.09 | 4.79 | 5.88 | 7.74 |
| SRES A1T | 2050 | 1.02 | 1.11 | 1.23 | 1.52 | 1.56 | 1.84 | 2.22 | 2.78 |
| | 2075 | 1.33 | 1.50 | 1.69 | 2.07 | 2.16 | 2.59 | 3.12 | 4.20 |
| | 2100 | 1.37 | 1.64 | 1.85 | 2.32 | 2.45 | 2.99 | 3.67 | 5.31 |
| SRES A2 | 2050 | 0.82 | 0.92 | 1.02 | 1.27 | 1.32 | 1.56 | 1.85 | 2.42 |
| | 2075 | 1.44 | 1.63 | 1.83 | 2.28 | 2.33 | 2.74 | 3.22 | 4.21 |
| | 2100 | 2.07 | 2.42 | 2.70 | 3.37 | 3.45 | 4.05 | 4.88 | 6.43 |
| SRES B1 | 2050 | 0.68 | 0.77 | 0.86 | 1.07 | 1.12 | 1.34 | 1.63 | 2.16 |
| | 2075 | 0.97 | 1.07 | 1.25 | 1.57 | 1.63 | 1.99 | 2.38 | 3.21 |
| | 2100 | 1.06 | 1.25 | 1.46 | 1.87 | 1.96 | 2.38 | 2.86 | 4.23 |
| SRES B2 | 2050 | 0.81 | 0.90 | 1.00 | 1.23 | 1.28 | 1.52 | 1.87 | 2.38 |
| | 2075 | 1.14 | 1.26 | 1.44 | 1.77 | 1.85 | 2.22 | 2.71 | 3.60 |
| | 2100 | 1.42 | 1.64 | 1.85 | 2.34 | 2.43 | 2.91 | 3.54 | 4.97 |
| ØDev.fromMean | | −39% | −31% | −22% | −3% | 0% | 19% | 43% | 91% |
| COMMIT | 2050 | 0.36 | 0.36 | 0.39 | 0.47 | 0.51 | 0.59 | 0.93 | 0.93 |
| | 2075 | 0.38 | 0.38 | 0.42 | 0.50 | 0.55 | 0.64 | 1.03 | 1.03 |
| | 2100 | 0.39 | 0.39 | 0.44 | 0.51 | 0.57 | 0.67 | 1.10 | 1.10 |
| HALVED-BY-2050 | 2050 | 0.71 | 0.77 | 0.87 | 1.07 | 1.13 | 1.36 | 1.71 | 2.17 |
| | 2075 | 0.66 | 0.77 | 0.89 | 1.12 | 1.20 | 1.48 | 1.88 | 2.64 |
| | 2100 | 0.54 | 0.71 | 0.84 | 1.08 | 1.17 | 1.47 | 1.88 | 2.90 |

Title Page

Abstract

Introduction

Conclusions

References

Tables

Figures



Back

Close

Full Screen / Esc

Printer-friendly Version

Interactive Discussion



MAGICC 6.0

M. Meinshausen et al.

Title Page

Abstract

Introduction

Conclusions

References

Tables

Figures

◀

▶

◀

▶

Back

Close

Full Screen / Esc

Printer-friendly Version

Interactive Discussion



Table B1. AOGCM calibration I results: MAGICC 6.0 parameters to emulate CMIP3 AOGCM models using idealized scenarios and three calibrated parameters only. See Table 1.

| | ΔQ_{2x}^b | ξ | Fixed ^a | | | | Calibrated parameters | | |
|---------------|---------------------|---------------------------------|------------------------|---------------------|---------------------|-------|-----------------------|------|--------------------|
| | | | $\frac{dKz_{top}}{dT}$ | k_{NS} | k_{LO} | μ | ΔT_{2x} | RLO | Kz |
| | $(\frac{W}{m^2})$ | $(\frac{K m^2}{W}) \times 1000$ | $(\frac{cm^2}{2K})$ | $(\frac{W}{m^2 K})$ | $(\frac{W}{m^2 K})$ | | (K) | | $(\frac{cm^2}{g})$ |
| AOGCM | | | | | | | | | |
| BCC-CM1 | not sufficient data | | | | | | | | |
| BCCR-BCM2.0 | not sufficient data | | | | | | | | |
| CCSM3 | 3.95 | 0 | 0 | 0.50 | 1.00 | 1.00 | 2.35 | 1.25 | 1.13 |
| CGCM3.1(T47) | 3.32 | 0 | 0 | 0.50 | 1.00 | 1.00 | 3.13 | 1.25 | 0.84 |
| CGCM3.1(T63) | not sufficient data | | | | | | | | |
| CNRM-CM3 | 3.48 | 0 | 0 | 0.50 | 1.00 | 1.00 | 2.46 | 1.27 | 0.72 |
| CSIRO-Mk3.0 | 3.47 | 0 | 0 | 0.50 | 1.00 | 1.00 | 2.18 | 1.24 | 1.35 |
| ECHAM5/MPI-OM | 4.01 | 0 | 0 | 0.50 | 1.00 | 1.00 | 3.95 | 1.31 | 0.50 |
| ECHO-G | 3.71 | 0 | 0 | 0.50 | 1.00 | 1.00 | 3.10 | 1.52 | 1.98 |
| FGOALS-g1.0 | 3.71 | 0 | 0 | 0.50 | 1.00 | 1.00 | 2.06 | 1.23 | 3.74 |
| GFDL-CM2.0 | 3.50 | 0 | 0 | 0.50 | 1.00 | 1.00 | 2.41 | 1.40 | 0.79 |
| GFDL-CM2.1 | 3.50 | 0 | 0 | 0.50 | 1.00 | 1.00 | 2.34 | 1.42 | 1.39 |
| GISS-AOM | not sufficient data | | | | | | | | |
| GISS-EH | 4.06 | 0 | 0 | 0.50 | 1.00 | 1.00 | 2.84 | 1.20 | 1.94 |
| GISS-ER | 4.06 | 0 | 0 | 0.50 | 1.00 | 1.00 | 2.66 | 1.23 | 3.14 |
| INM-CM3.0 | 3.71 | 0 | 0 | 0.50 | 1.00 | 1.00 | 2.26 | 1.30 | 0.59 |
| IPSL-CM4 | 3.48 | 0 | 0 | 0.50 | 1.00 | 1.00 | 3.93 | 1.21 | 1.71 |
| MIROC3.2(H) | 3.14 | 0 | 0 | 0.50 | 1.00 | 1.00 | 6.03 | 1.17 | 0.73 |
| MIROC3.2(M) | 3.09 | 0 | 0 | 0.50 | 1.00 | 1.00 | 4.12 | 1.36 | 1.21 |
| MRI-CGCM2.3.2 | 3.47 | 0 | 0 | 0.50 | 1.00 | 1.00 | 2.77 | 1.22 | 1.33 |
| PCM | 3.71 | 0 | 0 | 0.50 | 1.00 | 1.00 | 1.94 | 1.32 | 1.16 |
| UKMO-HadCM3 | 3.81 | 0 | 0 | 0.50 | 1.00 | 1.00 | 3.10 | 1.35 | 0.65 |
| UKMO-HadGEM1 | 3.78 | 0 | 0 | 0.50 | 1.00 | 1.00 | 3.09 | 1.35 | 0.64 |

^a The land/ocean area fractions are assumed identical to those provided in Table B3.

^b If all-sky radiative forcing data for doubled carbon dioxide concentrations has not been available (cf. Table 10.2 in Meehl et al., 2007), a default net (longwave+shortwave) forcing of 3.71 Wm^{-2} following Myhre et al. (1998) has been assumed (denoted in italics).

Table B2. AOGCM calibration II results: MAGICC 6.0 parameters to emulate CMIP3 AOGCM models using idealized scenarios and eight calibrated parameters. See Table 1.

| AOGCM | Fixed ^a | | | Calibrated parameters | | | | | |
|---------------|--|------------------------|---|-----------------------|----------------------------|---|----------------------------------|----------------------------------|-------|
| | ΔQ_{2x}^b ($\frac{W}{m^2}$) | ΔT_{2x} (K) | ξ ($\frac{Km^2}{W}$) $\times 1000$ | RLO | Kz ($\frac{cm^2}{s}$) | $\frac{dKz_{top}}{dT}$ ($\frac{cm^2}{sK}$) | k_{NS} ($\frac{W}{m^2K}$) | k_{LO} ($\frac{W}{m^2K}$) | μ |
| BCC-CM1 | not sufficient data | | | | | | | | |
| BCCR-BCM2.0 | not sufficient data | | | | | | | | |
| CCSM3 | 3.95 | 2.16 | 71 | 1.35 | 1.36 | -0.08 | 0.20 | 2.00 | 1.23 |
| CGCM3.1(T47) | 3.32 | 3.34 | 0 | 1.37 | 1.79 | -0.50 | 0.20 | 2.00 | 1.32 |
| CGCM3.1(T63) | not sufficient data | | | | | | | | |
| CNRM-CM3 | 3.48 | 2.23 | 75 | 1.19 | 0.65 | -0.00 | 0.20 | 0.20 | 1.00 |
| CSIRO-Mk3.0 | 3.47 | 2.17 | 0 | 1.05 | 2.15 | -1.00 | 0.20 | 0.20 | 1.00 |
| ECHAM5/MPI-OM | 4.01 | 3.46 | 75 | 1.51 | 0.62 | -0.00 | 1.00 | 2.00 | 1.26 |
| ECHO-G | 3.71 | 3.10 | 0 | 1.57 | 2.70 | -1.00 | 0.20 | 2.00 | 1.29 |
| FGOALS-g1.0 | 3.71 | 2.11 | 0 | 1.00 | 3.99 | -0.00 | 0.20 | 0.20 | 1.00 |
| GFDL-CM2.0 | 3.50 | 2.32 | 34 | 1.51 | 0.88 | -0.00 | 0.20 | 2.00 | 1.29 |
| GFDL-CM2.1 | 3.50 | 2.19 | 53 | 1.55 | 2.67 | -1.00 | 0.20 | 2.00 | 1.32 |
| GISS-AOM | not sufficient data | | | | | | | | |
| GISS-EH | 4.06 | 2.89 | 0 | 1.13 | 2.67 | -1.00 | 0.20 | 0.20 | 1.34 |
| GISS-ER | 4.06 | 2.52 | 57 | 1.39 | 4.69 | -1.00 | 1.66 | 1.36 | 1.26 |
| INM-CM3.0 | 3.71 | 2.28 | 0 | 1.19 | 0.89 | -1.00 | 0.20 | 0.20 | 1.00 |
| IPSL-CM4 | 3.48 | 4.03 | 0 | 1.11 | 2.20 | -0.24 | 0.20 | 0.32 | 1.00 |
| MIROC3.2(H) | 3.14 | 6.29 | 0 | 1.28 | 0.76 | -0.00 | 0.20 | 2.00 | 1.23 |
| MIROC3.2(M) | 3.09 | 4.15 | 0 | 1.42 | 1.52 | -0.32 | 0.20 | 2.00 | 1.24 |
| MRI-CGCM2.3.2 | 3.47 | 2.87 | 0 | 1.20 | 2.43 | -0.68 | 0.46 | 0.85 | 1.00 |
| PCM | 3.71 | 1.83 | 34 | 1.20 | 1.67 | -1.00 | 0.20 | 0.20 | 1.00 |
| UKMO-HadCM3 | 3.81 | 3.13 | 0 | 1.65 | 1.50 | -0.85 | 0.20 | 1.68 | 1.54 |
| UKMO-HadGEM1 | 3.78 | 2.90 | 75 | 1.28 | 0.84 | -0.00 | 0.20 | 0.20 | 1.00 |

^a See note a below Table B1.^b See note b below Table B1.**MAGICC 6.0**

M. Meinshausen et al.

Title Page

Abstract

Introduction

Conclusions

References

Tables

Figures

◀

▶

◀

▶

Back

Close

Full Screen / Esc

Printer-friendly Version

Interactive Discussion



Title Page

Abstract

Introduction

Conclusions

References

Tables

Figures

◀

▶

◀

▶

Back

Close

Full Screen / Esc

Printer-friendly Version

Interactive Discussion



Table B3. AOGCM calibration III results: MAGICC 6.0 parameters to emulate CMIP3 AOGCM models using both idealized and multi-forcing runs and an extended set of eight calibrated parameters. For a description of the calibrated parameters, see Table 1. The fixed parameters are ΔQ_{2X} , the AOGCM's forcing at doubled CO_2 concentration levels, and the land area fractions on the northern (F_{NL}) and Southern Hemisphere (F_{SL}).

| AOGCM | Fixed | | | Calibrated parameters | | | | | | | |
|---------------|--|---------------|---------------|------------------------|--|------|----------------------------|--|----------------------------------|----------------------------------|-------|
| | ΔQ_{2X}^b ($\frac{W}{m^2}$) | F_{NL} % | F_{SL} % | ΔT_{2X} (K) | ξ ($\frac{K m^2}{W}$) $\times 1000$ | RLO | Kz ($\frac{cm^2}{s}$) | $\frac{dK_{z,10p}}{dT}$ ($\frac{cm^2}{sK}$) | k_{NS} ($\frac{W}{m^2K}$) | k_{LO} ($\frac{W}{m^2K}$) | μ |
| BCC-CM1 | not sufficient data | | | | | | | | | | |
| BCCR-BCM2.0 | not sufficient data | | | | | | | | | | |
| CCSM3 | 3.95 | 49 | 25 | 2.14 | 64 | 1.37 | 1.27 | -0.21 | 0.20 | 2.00 | 1.22 |
| CGCM3.1(T47) | 3.32 | 50 | 25 | 2.97 | 0 | 1.34 | 0.68 | -0.00 | 1.03 | 0.68 | 1.00 |
| CGCM3.1(T63) | not sufficient data | | | | | | | | | | |
| CNRM-CM3 | 3.48 | 46 | 22 | 2.98 | 0 | 1.20 | 0.89 | -0.22 | 0.20 | 0.22 | 1.00 |
| CSIRO-Mk3.0 | 3.47 | 45 | 22 | 2.24 | 0 | 1.39 | 2.57 | -0.98 | 0.20 | 2.00 | 1.35 |
| ECHAM5/MPI-OM | 4.01 | 44 | 22 | 3.23 | 75 | 1.52 | 0.61 | -0.06 | 1.22 | 2.00 | 1.25 |
| ECHO-G | 3.71 | 47 | 23 | 2.63 | 0 | 1.63 | 0.43 | -1.00 | 0.29 | 2.00 | 1.20 |
| FGOALS-g1.0 | 3.71 | 56 | 29 | 2.42 | 75 | 1.35 | 1.48 | -0.52 | 0.20 | 2.00 | 1.08 |
| GFDL-CM2.0 | 3.50 | 50 | 25 | 2.31 | 55 | 1.52 | 0.85 | -0.02 | 0.20 | 2.00 | 1.30 |
| GFDL-CM2.1 | 3.50 | 51 | 26 | 2.28 | 50 | 1.56 | 2.31 | -1.00 | 0.20 | 2.00 | 1.33 |
| GISS-AOM | not sufficient data | | | | | | | | | | |
| GISS-EH | 4.06 | 53 | 27 | 2.54 | 0 | 1.10 | 2.14 | -1.00 | 0.58 | 0.20 | 1.00 |
| GISS-ER | 4.06 | 53 | 27 | 2.26 | 75 | 1.39 | 2.61 | -0.00 | 2.00 | 2.00 | 1.23 |
| INM-CM3.0 | 3.71 | 53 | 27 | 2.35 | 0 | 1.38 | 0.65 | -0.17 | 0.29 | 2.00 | 1.23 |
| IPSL-CM4 | 3.48 | 56 | 30 | 4.15 | 0 | 1.27 | 2.00 | -0.02 | 2.00 | 0.72 | 1.01 |
| MIROC3.2(H) | 3.14 | 48 | 24 | 5.73 | 0 | 1.29 | 0.73 | -0.00 | 1.93 | 1.99 | 1.00 |
| MIROC3.2(M) | 3.09 | 47 | 23 | 4.00 | 0 | 1.42 | 1.65 | -0.35 | 0.32 | 2.00 | 1.18 |
| MRI-CGCM2.3.2 | 3.47 | 57 | 29 | 2.48 | 0 | 1.28 | 1.05 | -0.24 | 0.22 | 2.00 | 1.18 |
| PCM | 3.71 | 55 | 29 | 1.90 | 0 | 1.17 | 1.36 | -0.18 | 0.20 | 0.20 | 1.00 |
| UKMO-HadCM3 | 3.81 | 47 | 23 | 3.21 | 0 | 1.59 | 0.70 | -0.00 | 0.56 | 2.00 | 1.39 |
| UKMO-HadGEM1 | 3.78 | 46 | 23 | 3.00 | 75 | 1.32 | 0.77 | -0.00 | 0.20 | 0.20 | 1.00 |

^a See Table note b in Table B1.

^b If available, the land area fractions were retrieved from the land area fraction sftlf variable of the pre-industrial control runs as given in the CMIP3 database. If not available, a standard land-sea mask has been used, as available for the landsea mask function within NCL, the NCAR Command Language.

Table B4.

| Calibrated parameters ^b | | | | | | | | | | | | | | |
|------------------------------------|------------------------|----------------------------|------|--------------------------------|----------------|---------------|-------|-------|--------------------------------------|-------------------------------------|-------------------------------------|---------------|-----------|------|
| Model | Ocean | | | | Flux Partition | | | | Temp. Sensitivity | | | Fertilization | | |
| | ΔT_{2x} (K) | k (yr ⁻¹) | r | α (K ⁻¹) | ϕ_H | q_S ×100 | g_P | g_H | σ_{NPP} (K ⁻¹) | σ_{E1} (K ⁻¹) | σ_{U1} (K ⁻¹) | β_m | β_s | |
| BERNcc | 2.41 | 0.24 | 0.95 | 0.04 | 0.50 | 0.10 | 0.45 | 0.40 | 0.01 | 0.07 | -0.14 | 0.15 | 1.10 | 0.65 |
| CSM1 | 1.66 | 0.09 | 1.68 | 0.04 | 1.00 | 0.10 | 0.48 | 0.35 | 0.01 | -0.02 | -0.28 | 0.15 | 1.81 | 0.44 |
| CLIMBER2LPJ | 3.57 | 0.26 | 2.87 | 0.00 | 0.98 | 0.10 | 0.45 | 0.41 | 0.04 | 0.10 | -0.26 | 0.23 | 1.95 | 0.52 |
| FRCGC ^c | 4.37 | 0.17 | 1.12 | 0.00 | 1.00 | 6.18 | 0.66 | 0.23 | 0.02 | -0.20 | 0.40 | 0.22 | 2.00 | 0.26 |
| HadCM3LC | 5.75 | 0.17 | 2.71 | 0.00 | 0.38 | 0.10 | 1.00 | 0.00 | 0.00 | 0.19 | -0.03 | 0.04 | 2.00 | 0.57 |
| IPSALCM2C | 5.38 | 0.01 | 0.01 | 0.00 | 1.00 | 0.10 | 0.87 | 0.00 | -0.06 | -0.20 | -0.10 | 0.09 | 2.00 | 0.75 |
| LLNL | 5.96 | 0.04 | 1.37 | 0.02 | 1.00 | 0.10 | 0.57 | 0.31 | 0.00 | -0.01 | -0.22 | 0.22 | 1.00 | 1.03 |
| MPI | 6.69 | 0.26 | 1.23 | 0.00 | 1.00 | 0.10 | 0.22 | 0.57 | -0.03 | -0.02 | -0.06 | 0.07 | 1.00 | 1.05 |
| UMD | 2.76 | 0.03 | 0.57 | 0.00 | 1.00 | 0.10 | 0.89 | 0.00 | -0.03 | 0.02 | -0.30 | 0.20 | 1.44 | 0.17 |
| UVIC27 | 5.39 | 0.19 | 1.74 | 0.01 | 1.00 | 0.10 | 0.69 | 0.00 | -0.02 | 0.01 | -0.18 | 0.11 | 1.95 | 0.57 |

| Model | Fixed parameters | | | | | | Goodness of fit CO ₂ (Coupled) | | | (Uncoupled) | | |
|--------------------|-------------------|-----------------------------------|------------------------------------|-------------------|--------------------|-------------------|---|----------------|---------------|----------------|----------------|---------------|
| | Y_{ref} (yr) | NPP_{mi} ($\frac{gC}{yr}$) | $R_{p,ini}$ ($\frac{gC}{yr}$) | P_{mi} (GtC) | D_{ini} (GtC) | S_{mi} (GtC) | C4MIP (ppm) | Emul. (ppm) | RMSE (ppm) | C4MIP (ppm) | Emul. (ppm) | RMSE (ppm) |
| BERNcc | 1765 | 66 | 12.3 | 885 | 93 | 1682 | 784 | 786 | 2.0 | 719 | 720 | 2.0 |
| CSM1 | 1820 | 67 | 12.3 | 870 | 57 | 1028 | 792 | 794 | 0.8 | 773 | 773 | 0.4 |
| CLIMBER2LPJ | 1901 | 64 | 11.9 | 919 | 95 | 1714 | 871 | 870 | 1.6 | 812 | 812 | 1.6 |
| FRCGC ^c | 1901 | 48 | 8.9 | 484 | 33 | 592 | 868 | 865 | 2.5 | 845 | 838 | 2.7 |
| HadCM3LC | 1860 | 61 | 11.3 | 495 | 61 | 1109 | 1025 | 1012 | 7.3 | 801 | 792 | 3.1 |
| IPSALCM2C | 1860 | 57 | 10.6 | 548 | 66 | 1205 | 769 | 746 | 8.0 | 695 | 683 | 4.7 |
| LLNL | 1870 | 67 | 12.4 | 735 | 103 | 1870 | 732 | 732 | 1.8 | 681 | 681 | 1.3 |
| MPI | 1860 | 53 | 9.9 | 351 | 72 | 1308 | 839 | 825 | 5.9 | 756 | 741 | 5.6 |
| UMD | 1860 | 53 | 9.8 | 493 | 70 | 1277 | 967 | 958 | 3.8 | 869 | 884 | 4.0 |
| UVIC27 | 1860 | 62 | 11.5 | 621 | 52 | 947 | 930 | 926 | 1.6 | 801 | 793 | 3.4 |

^a For a detailed description of the C4MIP carbon cycle models, see [Friedlingstein et al. \(2006\)](#) and references therein. For some models data was not available up to 2100 (MPI, IPSAL: up to 2099; FRCGC: up to 2098). In such cases, the latest available model years are provided in the Goodness of fit section. The RMSE is calculated over the last 101 years available.

^b In the automated calibration procedure, the climate module parameters vert. ocean diffusivity ($K_z=2.3 \text{ cm}^2 \text{ s}^{-1}$), and ocean-to-land heat exchange enhancement ($\mu=1.4$), land-ocean warming ratio (RLO=1.3) were kept at default values except climate sensitivity (ΔT_{2x}), which was calibrated in a first step to match temperatures of the coupled run for the model-specific CO₂ concentrations.

^c The terrestrial carbon pools of the FRCGC model were not used in the calibration routines as they exhibit significant drift at the start of their coupled and uncoupled runs.

Title Page

Abstract

Introduction

Conclusions

References

Tables

Figures

◀

▶

◀

▶

Back

Close

Full Screen / Esc

Printer-friendly Version

Interactive Discussion



MAGICC 6.0

M. Meinshausen et al.

Table B4. C4MIP calibration: Calibrated and fixed MAGICC 6.0 parameters to emulate ten of eleven C4MIP carbon cycle models. The upper part of the table lists calibrated parameters for MAGICC's ocean and terrestrial carbon cycle, with the latter including four parameters for the carbon flux partitions, four temperature sensitivity parameters and two parameters determining fertilization behavior. The lower part of the table provides the applied fixed parameters during the calibration procedure, such as reference years for each model, from which their scenarios started ($Y_{r_{ref}}$), initial carbon fluxes for net primary production (NPP_{ini}), the total heterotrophic respiration ($\sum R_{ini}$), initial pool sizes for the plant box (P_{ini}), the detritus box (D_{ini}) and the soil box (S_{ini}). For both the coupled and uncoupled model runs, some goodness of fit statistics are provided: Atmospheric CO_2 concentrations are given for year 2100 for the original C4MIP data (C4MIP) and the emulation by MAGICC (Emul.), as well as the root mean square error (RMSE) of concentrations over the whole 21st century (cf. Figs. 8 and 19).

Title Page

Abstract

Introduction

Conclusions

References

Tables

Figures

◀

▶

◀

▶

Back

Close

Full Screen / Esc

Printer-friendly Version

Interactive Discussion



MAGICC 6.0

M. Meinshausen et al.

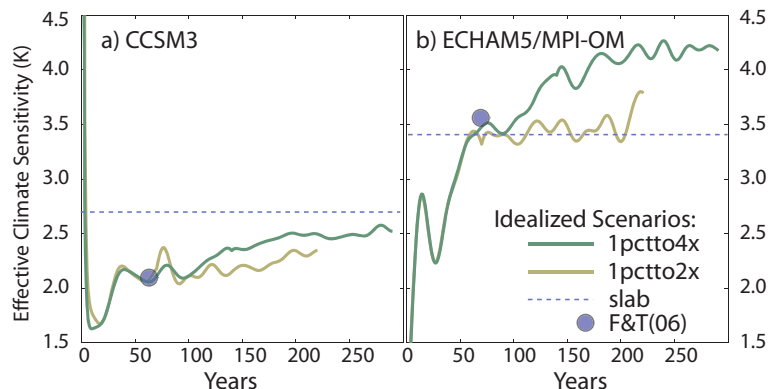


Fig. 1. The effective climate sensitivity diagnosed from lowpass filtered CCSM3 (a) and ECHAM5/MPI-OM (b) output for two idealized scenarios assuming an annual 1% increase in CO₂ concentrations until twice pre-industrial values in year 70 (1% to 2x) and quadrupled concentrations in year 140 (1% to 4x). Additionally, the reported slab ocean model equilibrium climate sensitivity (“slab”) and the sensitivity estimates by Forster and Taylor (2006) are shown (‘F&T(06)’).

[Title Page](#)[Abstract](#)[Introduction](#)[Conclusions](#)[References](#)[Tables](#)[Figures](#)[◀](#)[▶](#)[◀](#)[▶](#)[Back](#)[Close](#)[Full Screen / Esc](#)[Printer-friendly Version](#)[Interactive Discussion](#)

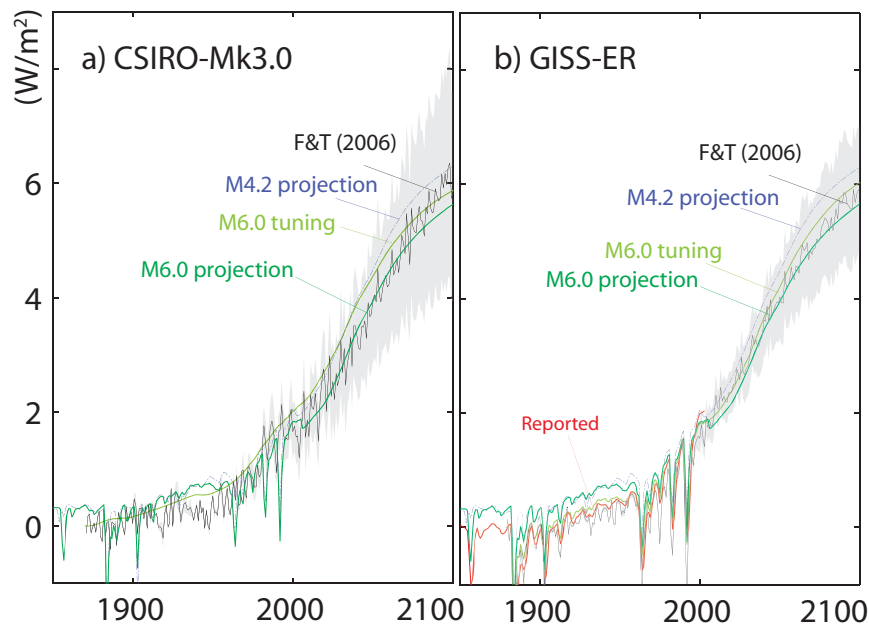


Fig. 2. Effective radiative forcing for the SRES A1B scenario from 1850 to 2100 for two CMIP3 AOGCMs. Shown are the net effective radiative forcing time-series used for calibrating MAGICC 6.0 to CSIRO-Mk3.0 **(a)** and GISS-ER **(b)**, respectively (“M6.0 calibration”). Due to various unification and completion adjustments, the effective forcings prescribed for the projections differ. Shown here is the mean for each AOGCM when combined with the ten C4MIP carbon cycle model calibrations (“M6.0 projection”). For comparison, the forcings used in IPCC AR4 for the medium carbon cycle feedback case (“M4.2 projection”) and the effective forcings (including uncertainties) as diagnosed by [Forster and Taylor \(2006\)](#) (“F&T, 2006”) are shown. In addition, in the case of the GISS-ER model, radiative forcing time series were made available by the modeling group (“Reported”) (Hansen, 2005, personal communication as reported in [Forster and Taylor, 2006](#)).

[Title Page](#)[Abstract](#)[Introduction](#)[Conclusions](#)[References](#)[Tables](#)[Figures](#)[◀](#)[▶](#)[◀](#)[▶](#)[Back](#)[Close](#)[Full Screen / Esc](#)[Printer-friendly Version](#)[Interactive Discussion](#)

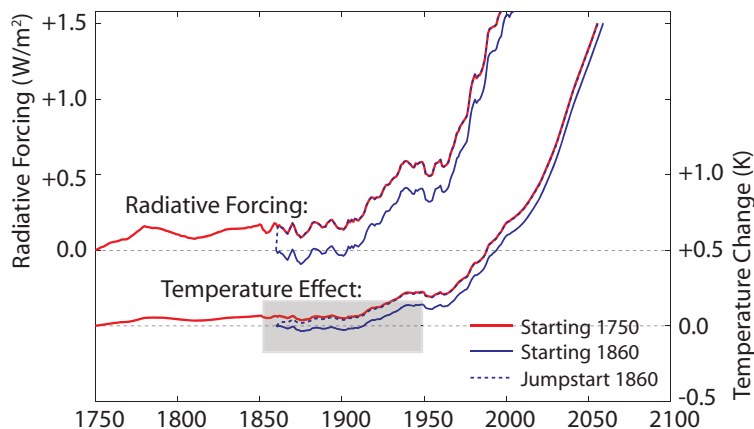


Fig. 3. Radiative forcing and temperature evolutions illustrating the “cold start problem” (Haselmann et al., 1993). A climate model run taking into account the forcing history since 1750 (red line) provides a different future projection compared to a run taking into account deviations from a later start year only, e.g. 1860 (blue solid line). A later common reference period, e.g. 1980–1999, or a “jump start” with radiative forcing being applied relative to 1750 (blue dashed line), minimize this initialization problem. The “jump start” run asymptotically approaches the run starting in 1750 (grey shaded area).

[Title Page](#)[Abstract](#)[Introduction](#)[Conclusions](#)[References](#)[Tables](#)[Figures](#)[◀](#)[▶](#)[◀](#)[▶](#)[Back](#)[Close](#)[Full Screen / Esc](#)[Printer-friendly Version](#)[Interactive Discussion](#)

MAGICC 6.0

M. Meinshausen et al.

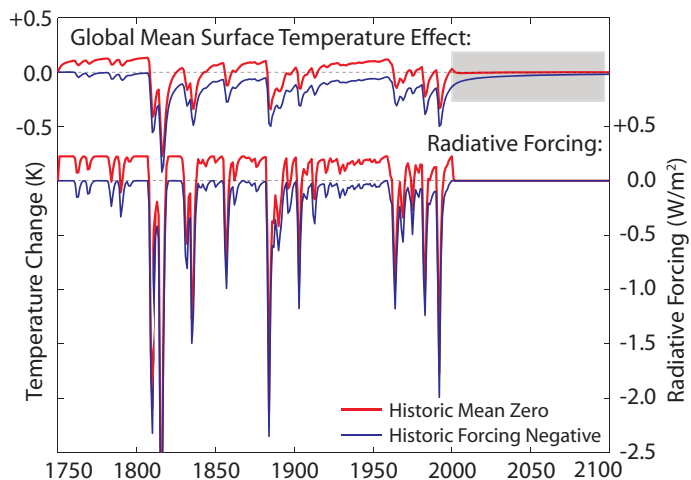
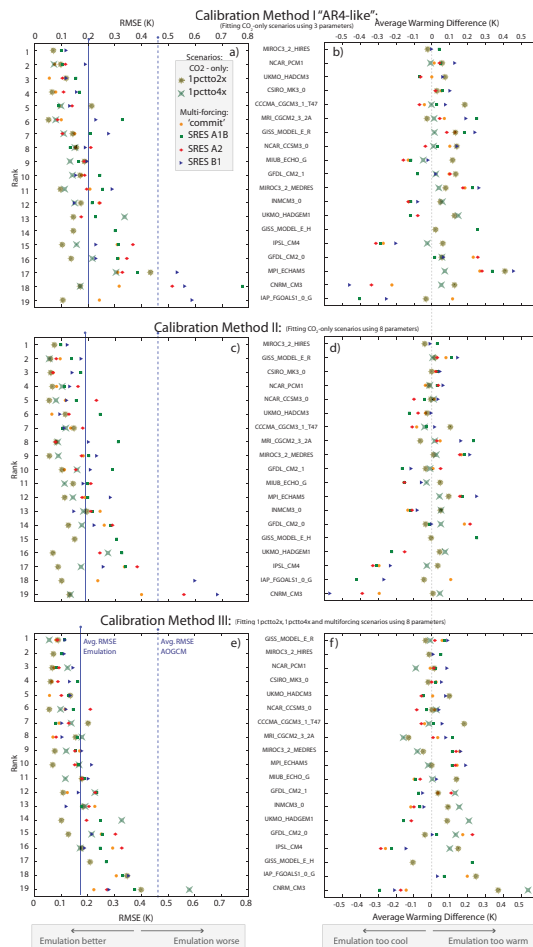


Fig. 4. Two conventions for applying volcanic radiative forcing: 1) Strictly negative forcing (blue) or 2) adjusted to a mean zero historical forcing (red). The grey shaded area shows the marginal temperature effect after year 2000, at which zero volcanic forcing is applied in both conventions, if pre-industrial is taken as the base value. The differences relative to 1750 vanish asymptotically, but do not vanish relative to other base years (such as year 2000, or the 1980–1999 mean).

[Title Page](#)[Abstract](#)[Introduction](#)[Conclusions](#)[References](#)[Tables](#)[Figures](#)[◀](#)[▶](#)[◀](#)[▶](#)[Back](#)[Close](#)[Full Screen / Esc](#)[Printer-friendly Version](#)[Interactive Discussion](#)

MAGICC 6.0

M. Meinshausen et al.



Title Page

Abstract Introduction

Conclusions References

Tables Figures

◀ ▶

◀ ▶

Back Close

Full Screen / Esc

Printer-friendly Version

Interactive Discussion



Fig. 5.

MAGICC 6.0

M. Meinshausen et al.

Fig. 5. The root mean square error (RMSE) and average warming differences between global-mean temperatures for individual AOGCMs and their emulations after calibrating MAGICC parameters with three different calibration procedures. Temperatures and ocean heat uptake for the 1%to2x and 1%to4x scenarios were fitted by calibrating three (“calibration I”; panel a,b) and eight (“calibration II”; panel c,d) MAGICC parameters, respectively (see Table 1). Calibration Method ‘III’ (panel e,f) used as well the multi-forcing runs SRES A1B, B1 and COMMIT into account when optimizing eight parameters (see Table 1). The emulations are ranked according to mean deviations (RMSE) between emulations and AOGCM data over the full length of all available scenarios. The AOGCM and MAGICC data were lowpass-filtered when calculating the RMSE values. For all emulations, “like-with-like” forcings were applied, i.e., the emulations were not subject to forcing adjustments. The mean RMSE for all emulations is given (“Avg. RMSE Emulations”) and compared to the average inter-model RMSE (‘Avg. RMSE AOGCM’). See text.

[Title Page](#)[Abstract](#)[Introduction](#)[Conclusions](#)[References](#)[Tables](#)[Figures](#)[◀](#)[▶](#)[◀](#)[▶](#)[Back](#)[Close](#)[Full Screen / Esc](#)[Printer-friendly Version](#)[Interactive Discussion](#)

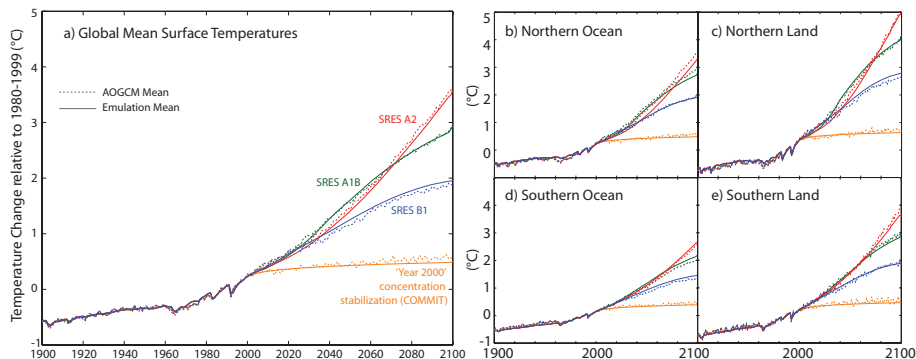


Fig. 6. Comparison of mean surface temperatures as diagnosed from CMIP3 AOGCMs (dashed) and the emulations with MAGICC 6.0 using “like-with-like” forcings using Method ‘III’ calibration results (solid lines, see Sect. 3.2). The scenarios shown are SRES A1B (green), B1 (blue) and A2 (red) in addition to the “year 2000 concentration stabilization” (COMMIT) experiment (orange). For the different scenarios, the number of available AOGCM datasets differs, which is taken into account, so that only the mean across the corresponding set of emulations is shown. The land and ocean regions in each hemisphere were determined from the individual AOGCMs’ land-ocean masks.

[Title Page](#)[Abstract](#)[Introduction](#)[Conclusions](#)[References](#)[Tables](#)[Figures](#)[◀](#)[▶](#)[◀](#)[▶](#)[Back](#)[Close](#)[Full Screen / Esc](#)[Printer-friendly Version](#)[Interactive Discussion](#)

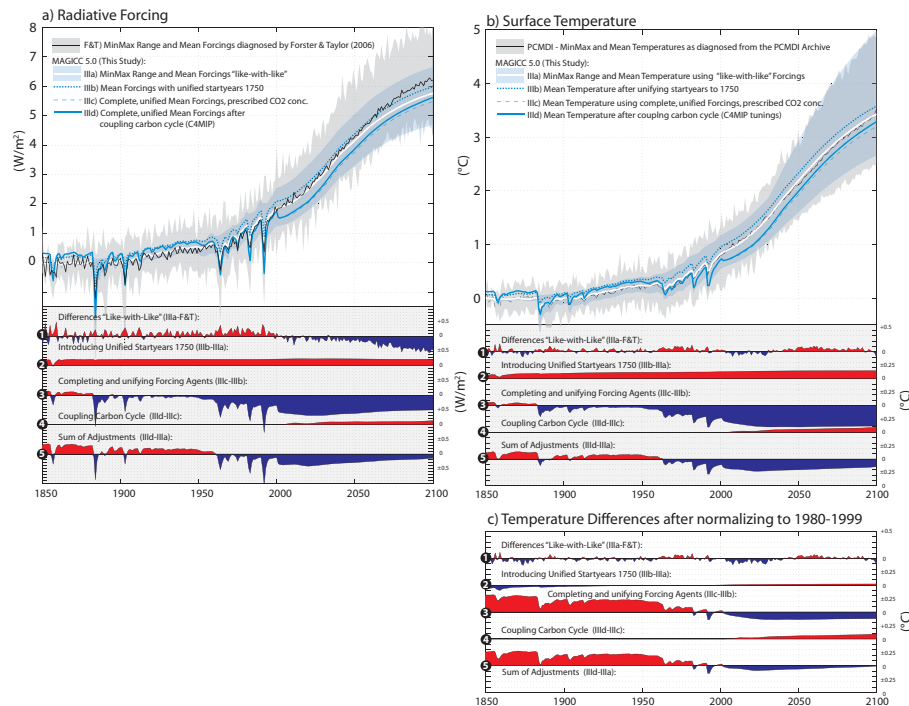


Fig. 7. Net Radiative Forcing (panel **a**) and global-mean surface temperatures (**b**) for the SRES A1B scenario according to the calibrated MAGICC 6.0 (calibration Illa) as presented in this study. For comparison, the radiative forcing applied is compared to the means across all 19 CMIP3 AOGCMs, as diagnosed by Forster and Taylor (2006) (panel a). For temperature, the MAGICC 6.0 emulations are compared to the means diagnosed from the matching set of 19 CMIP3 AOGCMs as in the PCMDI archive relative to the respective startyears of the simulations. Differences are shown as well after normalization to the period 1980–1899 (panel c). See Table 1 and text for discussion of the different forcing adjustments and temperature effects (black circled numbers).

[Title Page](#)
[Abstract](#)
[Introduction](#)
[Conclusions](#)
[References](#)
[Tables](#)
[Figures](#)
[◀](#)
[▶](#)
[◀](#)
[▶](#)
[Back](#)
[Close](#)
[Full Screen / Esc](#)
[Printer-friendly Version](#)
[Interactive Discussion](#)


MAGICC 6.0

M. Meinshausen et al.

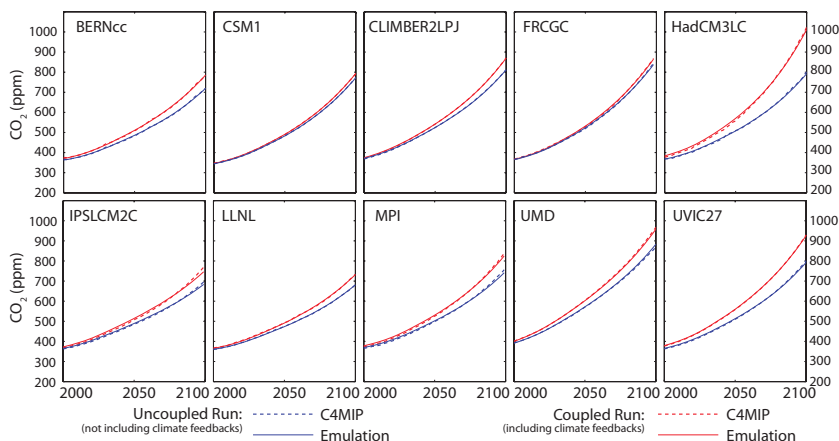


Fig. 8. Atmospheric CO₂ concentrations from 2000 to 2100 comparing C4MIP carbon cycle model results (dashed) with the calibrated MAGICC 6.0 (solid) model. Shown are the coupled (including climate feedbacks, red lines) and uncoupled (excluding climate feedbacks, blue lines) runs for the anthropogenic CO₂ emissions based on the IPCC SRES A2 scenario. See Fig. 19 in Appendix B for comparisons between emulations and C4MIP models of other carbon fluxes and pools.

[Title Page](#)[Abstract](#)[Introduction](#)[Conclusions](#)[References](#)[Tables](#)[Figures](#)[◀](#)[▶](#)[◀](#)[▶](#)[Back](#)[Close](#)[Full Screen / Esc](#)[Printer-friendly Version](#)[Interactive Discussion](#)

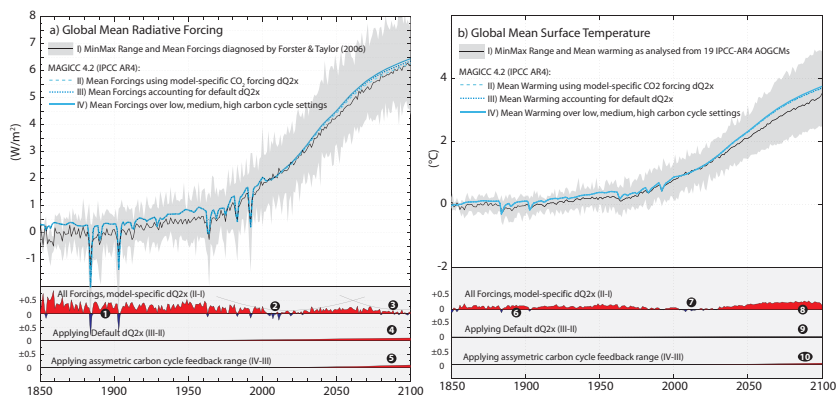


Fig. 9. Net Radiative Forcing (panel a) and global-mean surface temperatures (b,c) for the SRES A1B scenario within MAGICC 4.2 as presented in IPCC AR4. For comparison, the radiative forcing is compared to the means across all 19 CMIP3 AOGCMs, as diagnosed by Forster and Taylor (2006) (panel a). For temperature, the MAGICC 4.2 emulations are shown compared to the means diagnosed from the matching set of 19 CMIP3 AOGCMs. See text for discussion (black circled numbers). As presented in IPCC AR4 (see Fig. 10.26 in Meehl et al., 2007), MAGICC 4.2 temperature series are here normalized towards a 21-year mean around 1990 of 0.52°C above 1861–1890 (Folland et al., 2001; Jones and Moberg, 2003). The AOGCM temperature perturbations are shown relative to their control runs. The mean across AOGCMs relative to their control runs agrees well with the observational data around 1990, although there is a significant spread across AOGCMs (grey shading).

[Title Page](#)
[Abstract](#)
[Introduction](#)
[Conclusions](#)
[References](#)
[Tables](#)
[Figures](#)
[◀](#)
[▶](#)
[◀](#)
[▶](#)
[Back](#)
[Close](#)
[Full Screen / Esc](#)
[Printer-friendly Version](#)
[Interactive Discussion](#)

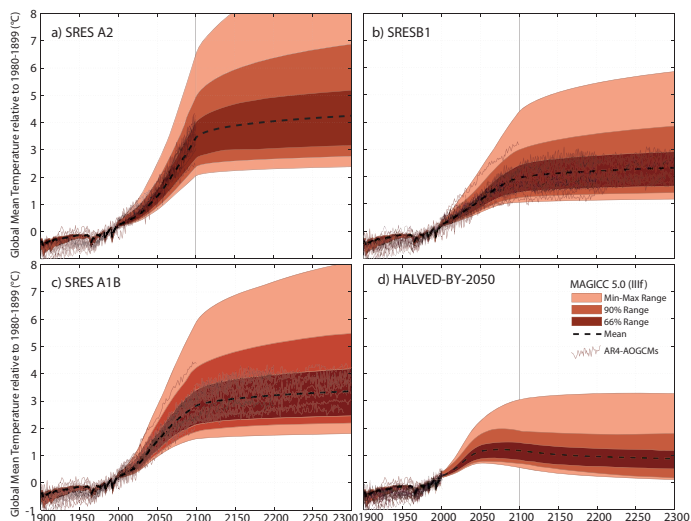



Fig. 10. Global-mean surface temperatures relative to 1980–1999 of original AOGCMs (thin lines) and the emulations using 10 C4MIP carbon cycle emulations and 19 CMIP3 AOGCM emulations for the three SRES scenario B1, A1B and A2 under complete and unified forcing assumptions (emulation IIIId, see Sect. 3.2). As well, temperature projections are given for an emission scenario with halved 2050 emissions relative to 1990 levels (“Halved-by-2050”-panel d). The shaded areas denote the ranges of the 190 cross-combinations of emulations, specifically the ranges in which the middle 66% (dark), 90% (medium) and all (bright patches) of the 190 emulations are located. For illustrative purposes, the 2°C level above pre-industrial temperatures is indicated by a red line.

[Title Page](#)[Abstract](#)[Introduction](#)[Conclusions](#)[References](#)[Tables](#)[Figures](#)[◀](#)[▶](#)[◀](#)[▶](#)[Back](#)[Close](#)[Full Screen / Esc](#)[Printer-friendly Version](#)[Interactive Discussion](#)

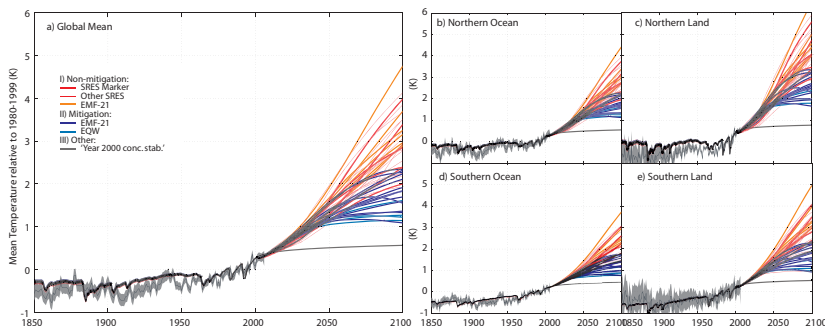


Fig. 11. Global-mean and hemispheric land-ocean surface temperatures relative to 1980–1999 for different non-mitigation and mitigation scenarios as well as the “Year 2000 concentration stabilization” experiment. The mean temperature evolution of 190 AOGCMs and C4MIP emulations for each of the 58 scenarios is derived from 11 020 total simulations and compared to historical observations including 90% uncertainty ranges (Brohan et al., 2006).

[Title Page](#)[Abstract](#)[Introduction](#)[Conclusions](#)[References](#)[Tables](#)[Figures](#)[◀](#)[▶](#)[◀](#)[▶](#)[Back](#)[Close](#)[Full Screen / Esc](#)[Printer-friendly Version](#)[Interactive Discussion](#)

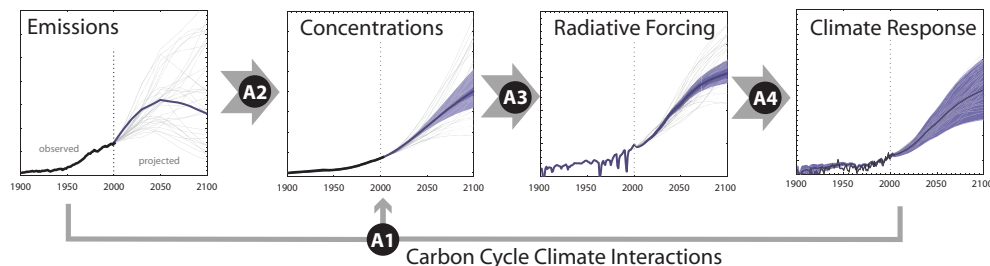


Fig. 12. Schematic overview of MAGICC, being a simple, but comprehensive carbon cycle climate model encompassing the key steps from emissions to global and hemispheric climate responses. Black circled numbers denote the sections in this Appendix describing the respective algorithms in use.

[Title Page](#)[Abstract](#)[Introduction](#)[Conclusions](#)[References](#)[Tables](#)[Figures](#)[I◀](#)[▶I](#)[◀](#)[▶](#)[Back](#)[Close](#)[Full Screen / Esc](#)[Printer-friendly Version](#)[Interactive Discussion](#)

MAGICC 6.0

M. Meinshausen et al.

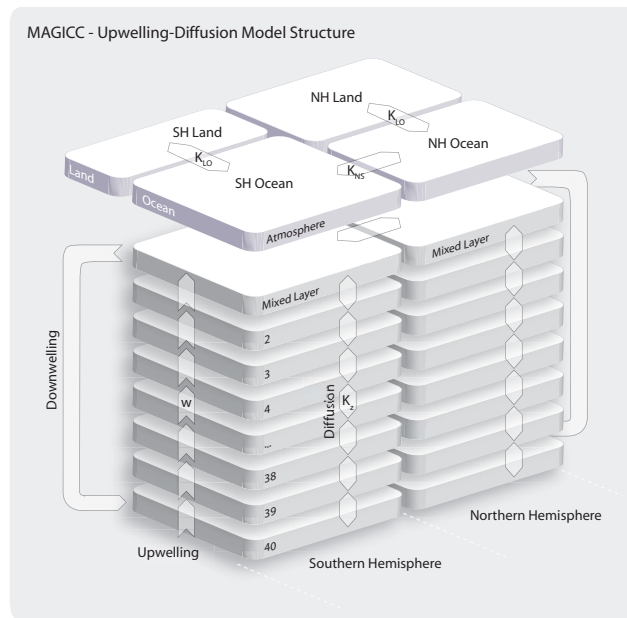


Fig. 14. The schematic structure of MAGICC's upwelling-diffusion energy balance module with land and ocean boxes in each hemisphere. The processes for heat transport in the ocean are deep-water formation, upwelling, diffusion, and heat exchange between the hemispheres. Not shown is the entrainment and the vertically depth-dependent area of the ocean layers (see Fig. 15 and text).

[Title Page](#)
[Abstract](#)
[Introduction](#)
[Conclusions](#)
[References](#)
[Tables](#)
[Figures](#)
[◀](#)
[▶](#)
[◀](#)
[▶](#)
[Back](#)
[Close](#)
[Full Screen / Esc](#)
[Printer-friendly Version](#)
[Interactive Discussion](#)


MAGICC 6.0

M. Meinshausen et al.

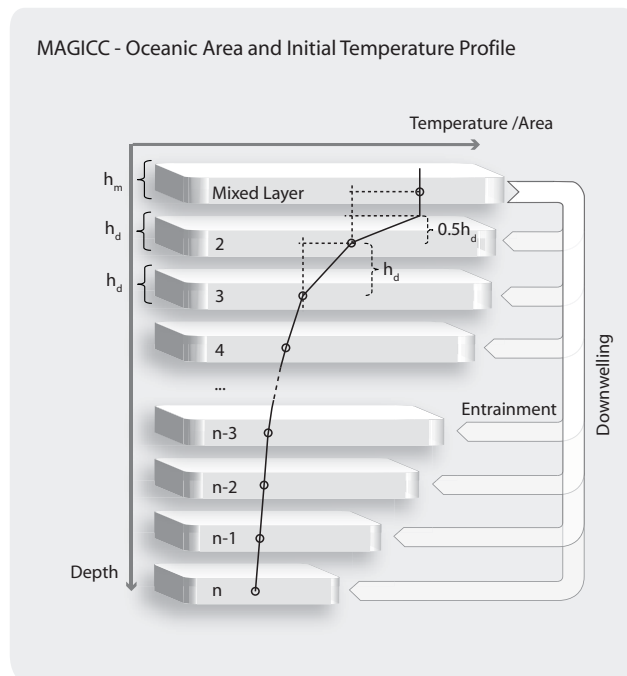
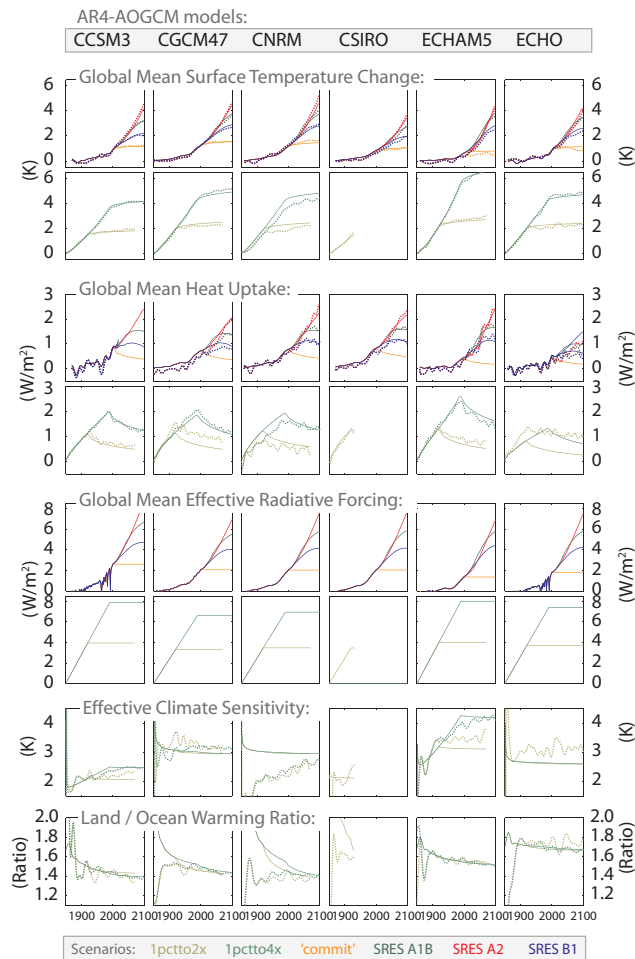


Fig. 15. The schematic oceanic area and initial temperature profile in MAGICC's ocean hemispheres. Diffusion driven heat transport is modeled proportional to the vertical gradient of temperatures, which is especially high below the mixed layer. The entrainment is modeled such that the upwelling velocity is vertically constant despite depth-variable ocean areas.

[Title Page](#)
[Abstract](#)
[Introduction](#)
[Conclusions](#)
[References](#)
[Tables](#)
[Figures](#)
[◀](#)
[▶](#)
[◀](#)
[▶](#)
[Back](#)
[Close](#)
[Full Screen / Esc](#)
[Printer-friendly Version](#)
[Interactive Discussion](#)


MAGICC 6.0

M. Meinshausen et al.



Title Page

Abstract

Introduction

Conclusions

References

Tables

Figures

◀

▶

◀

▶

Back

Close

Full Screen / Esc

Printer-friendly Version

Interactive Discussion



Fig. 16.

MAGICC 6.0

M. Meinshausen et al.

Fig. 16. Comparison of global-mean surface temperature (rows 1 and 2), heat uptake (rows 3,4), effective radiative forcing (rows 5,6), the effective climate sensitivity (row 7) and the land-ocean warming ratio (8), between CMIP3 AOGCM models (dotted) and the calibrated MAGICC 6.0 (solid) model (calibration IIIa) from 1850 to 2100. Shown are the comparisons for the idealized CO₂-only scenarios (1pctto2x and 1pctto4x) set to start in 1850 and the multi-forcing runs for 20th century (20c3m), three SRES and the commitment scenario. For the multi-gas scenarios, MAGICC is driven here by the AOGCM-specific subsets of forcing agents (see Table 2). AOGCM drift was removed by subtracting the respective lowpass-filtered control run segments. Both the AOGCM and the MAGICC temperature outputs were lowpass-filtered using a pass band boundary of 0.05 cycle/yr and roughness constraint (Mann, 2004). See following figures for the other CMIP3 AOGCMs emulations.

[Title Page](#)[Abstract](#)[Introduction](#)[Conclusions](#)[References](#)[Tables](#)[Figures](#)[◀](#)[▶](#)[◀](#)[▶](#)[Back](#)[Close](#)[Full Screen / Esc](#)[Printer-friendly Version](#)[Interactive Discussion](#)

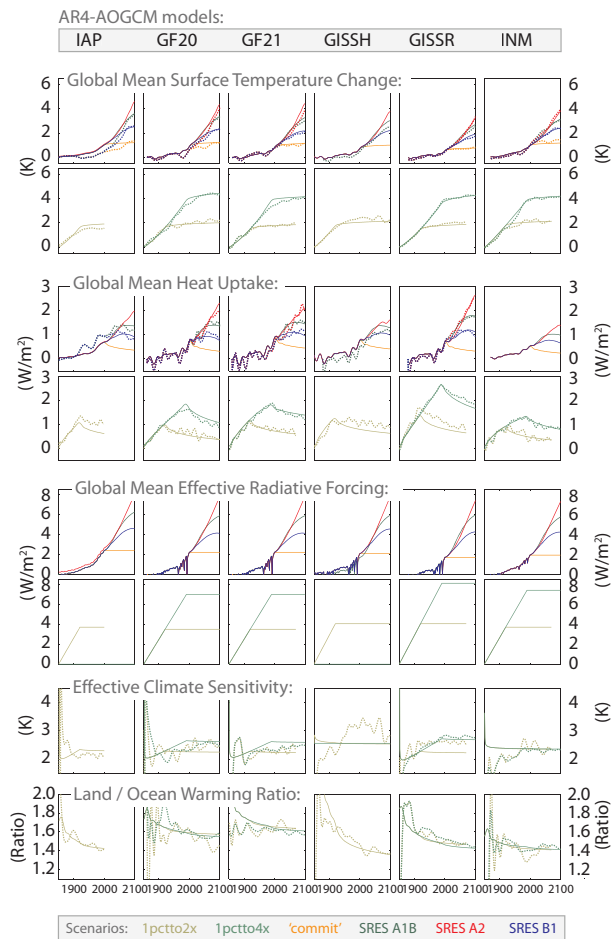

[Title Page](#)
[Abstract](#)
[Introduction](#)
[Conclusions](#)
[References](#)
[Tables](#)
[Figures](#)
[Back](#)
[Close](#)
[Full Screen / Esc](#)
[Printer-friendly Version](#)
[Interactive Discussion](#)


Fig. 17. As Fig. 16, but for another six of the 19 emulated CMIP3 AOGCMs.

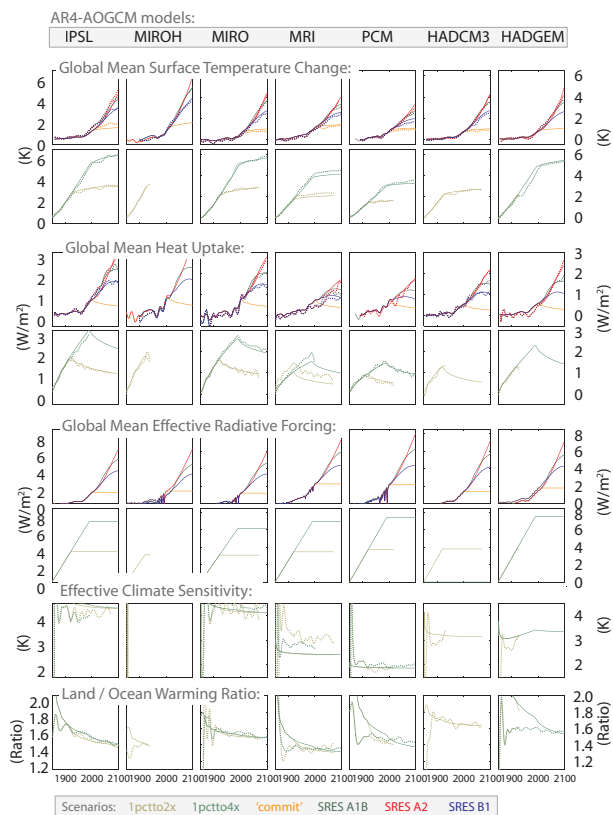


Fig. 18. As Fig. 16, but for another seven of the 19 emulated CMIP3 AOGCMs.

[Title Page](#)
[Abstract](#)
[Introduction](#)
[Conclusions](#)
[References](#)
[Tables](#)
[Figures](#)
[Back](#)
[Close](#)
[Full Screen / Esc](#)
[Printer-friendly Version](#)
[Interactive Discussion](#)


MAGICC 6.0

M. Meinshausen et al.

Title Page

Abstract

Introduction

Conclusions

References

Tables

Figures

◀

▶

◀

▶

Back

Close

Full Screen / Esc

Printer-friendly Version

Interactive Discussion

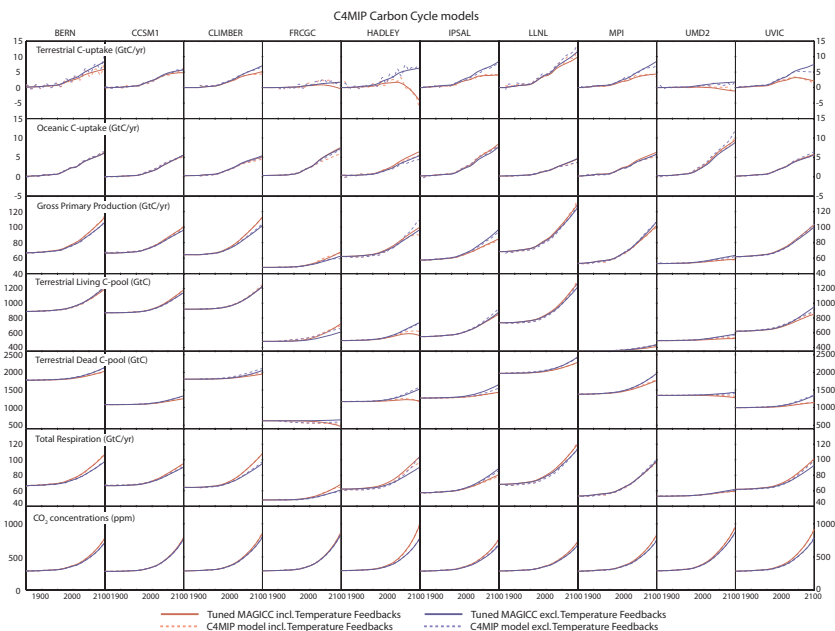


Fig. 19. Comparison of carbon cycle fluxes, pools and atmospheric CO_2 concentrations between C4MIP carbon cycle models (dashed) and the calibrated MAGICC 6.0 (solid) model. Shown are the coupled (including temperature feedbacks, red lines) and uncoupled (excluding temperature feedbacks, blue lines) runs for the anthropogenic CO_2 emissions based on the IPCC SRES A2 scenario. The carbon fluxes of the C4MIP models were lowpass-filtered.